universität wien

MASTERARBEIT | MASTER'S THESIS

Titel | Title

Source technologies for optomechanics in high vacuum

verfasst von | submitted by

Stefan Schrems BSc

angestrebter akademischer Grad | in partial fulfilment of the requirements for the degree of

Master of Science (MSc)

Wien | Vienna, 2024

Studienkennzahl lt. Studienblatt | Degree programme code as it appears on the student record sheet:	UA 066 876
Studienrichtung lt. Studienblatt | Degree programme as it appears on the student record sheet:	Masterstudium Physics
Betreut von | Supervisor:	Univ.-Prof. Dr. Markus Arndt

Contents

Acknowledgements

Writing my Master thesis took a lot of effort and I would not have been able to do it without the help I received both from my family, as well as our research group.

First and foremost, I would like to thank my supervisor, Professor Markus Arndt for supervising both for my Master and Bachelor Thesis and always being available to answer any questions I might have.

On a similar note, I would like to thank is Nafia Rahman, who was working on our Experimental setup with me. Due to COVID, I couldn't come to the Lab for my Bachelor Thesis, so she was the one to introduce me to the realities of actual Labwork and did so with great patience.

I also want to thank Florian Fechtel for taking the Time to proofread this Thesis not once but twice. Your help drastically reduced not only the number of grammatical errors, but also helped me find some errors in my thoughts while writing this thesis.

More generally, I would also like to thank the Quantum Nanophysics group and especially the Nanoparticles subgroup for always offering help when I needed it. To be able to work in such a good environment truly made my work on this thesis very enjoyable.

Finally, I would like express my gratitude to my family for their love and support during my whole studies, especially during the writing of my Thesis. None of this would have been possible without you.

Abstract

Trapping and cooling of nanoparticles is a field of modern physics with many prospective applications in sensing and tests of the foundations of physics. Optically trapped nanoparticles are especially interesting due to their decoupling from the environment, which allows for precise control of their dynamics. This however requires a source of nanoparticles with a well-defined mass, shape, size, velocity and charge with a low average velocity to load the trap. The cooling aspect also requires a low-pressure environment to minimize the interaction with any background gas. The main issues with most current loading mechanisms are twofold. They volatilise a high amount of nanoparticles simultaneously, which have a very high chance of polluting the sensitive optics of the trap, or they volatilise nanoparticles at high velocity. These particles require buffer-gas slowing in order for them to be caught in the trapping potential, which makes the source incompatible with a vacuum environment.

This thesis is dedicated to the investigation of two source techniques, Laser-induced acoustic desorption (LIAD), as well as (Poly-)phthalaldehyde (PPA) sublimation, which show promise to improve upon the aforementioned points. LIAD works by using a laser to spread acoustic and termal waves through a substrate, which desorb particles from its surface. This thesis focuses on LIAD for silica nanoparticles across different substrates, such as copper or titanium from $5\,\mu m$ to $700\,\mu m$ thickness in a vacuum environment ($2 \times 10^{-2}\,mbar$), which are detected by a $1550\,nm$ optical tweezer in combination with a fiber collecting light scattered of the particle. We observed single nanoparticles with a success rate of roughly $1/100$, whose average velocity for almost all substrates were below $5\,m/s$.

PPA sublimation is a new prospective volatilisation technique, that uses the property of (Poly-)phthalaldehyde to sublimate, instead of melt, when heated. We apply nanoparticles on a layer of PPA, which is vaporized using a CW-laser, vaporizing the nanoparticles with it in the process. Using this method, we were able to desorb nanoparticles and detect them in an optical tweezer. PPA-samples coated in SiO_2-nanoparticles of $300\,nm$ diameter have been prepared and an in-situ imaging system for direct observation of the sublimation process has been created. Finally, an analysis of the predicted particle behaviour after sublimation has been made.

Zusammenfassung

Fangen und Kühlen von Nanoteilchen ist ein Feld der modernen Physik mit vielen Anwendungsbereichen, wie beispielsweise hochsensitive Beschleunigungsmessungen oder Tests von fundamentalen Fragen der Quantenphysik auf mesoskopischer Ebene. Optisch gefangene Nanoteilchen im Speziellen interagieren minimal mit ihrer Umgebung interagieren, was präzisere Kontrolle über sie ermöglicht. Dazu benötigen wir eine Quelle mit wohldefinierten Teilchengrößen, Massen, Ladungen sowie Formen mit niedrigen Geschwindigkeiten, um optische Fallen auch ohne Buffergaskühlung zu füllen. Die Ladunsgeffizienz der meisten Teilchenquellen wird von zwei Faktoren limitiert. Eine große Menge an Teilchen werden gleichzeitig desorbiert und kontaminieren die sensitiven Optiken der Teilchenfalle, oder die Teilchen sind zu schnell.

Diese Arbeit behandelt zwei Teilchenquellen, namentlich Laser-induzierte akustische Desorption (LIAD), sowie (Poly-)phthalaldehyd (PPA) Sublimation. Beide haben das Potential, den Ladungsprozess von Teilchenquellen zu verbessern. Im Rahmen von LIAD wird ein mit Teilchen beladenes Substrat mit einem gepulsten Laser bestrahlt, der termische und akustische schockwellen auslöst. Dadurch werden Nanoteilchen auf der Vorderseite des Substrats abgelöst. Wir untersuchen die Desorption von SiO_2-Nanoteilchen von verschiedenen Substratsmaterialien, wie beispielsweise Kupfer oder Titan, mit Dicken von $5\,\mu m$ bis $700\,\mu m$ in Vakuumumgebung ($2 \times 10^{-2}\,mbar$). Als Teilchendetektor dient eine $1550\,nm$ optische Pinzette im Zusammenhang mit einer Glasfaser, die das Streulicht der Nanoteilchen sammelt. Die Durchschnittsgeschwindigkeit der Nanoteilchen, die wir in der optischen Pinzette sehen konnten lag unter $5\,m/s$ für fast alle Substrate, mit einer Erfolgswarscheinlichkeit von $1\,\%$.

PPA Sublimation hingegen ist eine neuartige Quelltechnik, welche die fragmentierende Sublimation von (Poly-)phthalaldehyd ausnutzt. Teilchen sind auf eine dünne PPA-Schicht aufgebracht, welche unter der Bestrahlung eines Lasers aufheizt und sublimiert. Mit dieser Methode ist es uns gelungen, eine funktionierende Nanoteilchenquelle zu konstruieren und desorbierte SiO_2 Nanoteilchen in einer optischen Pinzette zu detektieren. Diese Arbeit fokussiert sich hauptsächlich auf die Präparation der Substrate und deren Untersuchung mittels Fluoreszenzmikroskopie bzw. eines selbst gebauten in-situ Mikroskopiesystems. Verschiedene Durchmesser von SiO_2-Nanoteilchen wurden untersucht und das erwartete Teilchenverhalten nach deren Verdampfung wurde analysiert.

1 Introduction

Quantum optomechanics is the interaction of motion of micro- or nanomechanical objects with light. In the late 60's, proposals were made to detect the mechanical motion of an optical Fabry-Perot resonator caused by gravitational waves [1, 2]. Around the same time, Arthur Ashkin was the first to demonstrate optical levitation, as well as trapping of micro- and nanospheres using the radiation pressure of focused laser light in 1970, followed by experiments to optically trap bacteria and viruses in 1987 [3–5]. Eight years later, laser cooling of magnesium ions was demonstrated [6].

The first laser cooling experiments made use of Doppler shifts in two level systems such as atoms [6], making them incompatible with particles lacking clearly defined energy levels, such as nanoparticles. The first instance of one-dimensional cooling of an optically levitated glass microsphere was reported in 2011 [7]. The center-of-mass motion of the microsphere was brought from room temperature to $1.5\,\mathrm{mK}$ via parametric feedback cooling. Cooling of silica nanoparticles using the same technique was reported the following year [8]. More recently, coupling between nanoparticles in a Paul trap has been exploited to allow for indirect feedback cooling of nanoparticles, opening the road of laser cooling for fragile particles [9].

Following the initial successes of feedback cooling of levitated nanoparticles, cavity based cooling methods for nanoparticles have been developed in an effort to reach quantum ground state. Notably, cooling of silicon and silica nanoparticles coupled to an optical cavity was demonstrated in 2013 [10, 11], followed by three-dimensional cooling of nanoparticles using coherent scattering [12, 13], which has been reported to reach the motional ground state for two mechanical modes just last year [14].

Today, quantum optomechanics is a rapidly expanding field of research with many practical applications, such as ultra-sensitive torque and momentum sensors [15]. Optically levitated, slow particles in vacuum especially distinguish themselves with their minimal interaction with their environment. Besides other effects this allows for tests of quantum mechanics at mesoscopic scales [16], but is also expected to give rise to a number of interesting quantum phenomena, such as rotational revivals of nanorods [17].

Tightly focused laser light can trap single nanoparticles with minimal environmental noise, but in a submicron region and with trapping depths ranging from a few to multiple hundred eV. [18, 19]. To realize such setups, it is necessary to provide a slow, reproducible source of intact nanoparticles with controllable charge, which can be used to load the trap in high vacuum ($(1 \times 10^{-5} - 1 \times 10^{-10})\,\mathrm{mbar}$).[20, 21]

The aim of this thesis is to explore different source techniques applicable to both SiO_2-,as well as biological nanoparticles such as bacteria and viruses for optically levitated systems at pressure regimes from $(1 \times 10^{-5} - 1 \times 10^{-10})\,\mathrm{mbar}$. Upon finding such a source, we want to quantify the velocity spread, angular velocity spread, particle fragmentation, as well as their charge distribution of such a source. There exist a multitude of different source techniques. Nebulisation, where one sprays aerosolized nanoparticle solution in the trapping region [8]. Shaking nanoparticles of a substrate using a piezoelectric transducer [22]. Laser desorption (LD), which uses a pulsed laser to thermally evaporate nanoparticles [23] Matrix-assisted laser desorption ionization (MALDI), where a pulsed laser evaporates a matrix, which causes the desorption of the particles embedded in a matrix [24]. Electrospray-ionisation (ESI), where high voltage is applied to the nanoparticle solution, producing an aerosol similar to nebulisation, though the resulting particle plume is charged [25]. Note that while MALDI and ESI are often used for organic molecules, the incompatibility of most MALDI-matrices with nanoparticles, as well as particle clumping when volatilised with ESI make them unpopular choices for the desorption of nanoparticles [26]. Laser-

induced forward-, or backward transfer produces a material jet by impacting a solid slate with a high-energy nano- or femtosecond pulsed laser, which subsequently condenses into a nanoparticle [27, 28]. Laser-induced accoustic desorption (LIAD) works by irradiating the back-side of a substrate using a high-powered pulsed laser, thereby desorbing the nanoparticles on the substrate front-side [29] and (Poly-)Phtalaldehyde (PPA) sublimation, where sublimation of a thin layer of PPA containing nanoparticles, volatilises these nanoparticles in the process.

Development of a nanoparticle source has two aspects. The volatilisation of the nanoparticles and their quantitative detection method. The latter is discussed in section 2, while the former are treated in section 3, including some numerical predictions of nanoparticle behaviour.

In section 4, we discuss our choices regarding the desorption setups used for LIAD, as well as PPA sublimation and give a detailed account on our methods of preparing said substrate, as well as the resulting particle distributions observed in fluorescence microscopy.

Finally, in sections 5 and 6, we interpret our experimental results and discuss possible improvements of our source.

2 Optical detection methods of nanoparticles

This section gives a brief summary of the optical detection methods which will be used in this thesis. We start with an introduction of Gaussian beam optics, followed by optical tweezers in the Rayleigh approximation. Following this, the scattering properties of nanoparticles in a standing wave will be discussed. We will also briefly summarise the principles of fluorescence microscopy, since some nanoparticles come decorated with dye labels.

2.1 Gaussian Beam optics

Understanding the interaction between an optical tweezer and a nanoparticle requires knowledge of the properties of the light field. Here we give a brief overview of paraxial beams following [30–33].

2.1.1 Maxwell equations in vacuum for a monochromatic paraxial electric field

The Maxwell equations in absence of charges and currents can be transformed into the scalar wave equation.

$$\left(\vec{\nabla}^2 + \frac{1}{c^2}\frac{\partial^2}{\partial t^2}\right)\vec{E} = 0 \tag{1}$$

With c being the velocity of light, $\vec{E}$ the electric field and t the time. In case of monochromatic light it is solved by the electric field $\vec{E}$.

$$\vec{E}(t,\vec{r}) = \vec{E}(\vec{r}) \cdot \mathrm{e}^{-i\omega t} \tag{2}$$

Here $c = \omega/(nk)$, with ω being the light frequency, k the magnitude of its wave vector and n the diffractive index of the material in which the wave propagates. We will assume the wave to be propagating in vacuum for the rest of this section i.e. $n = 1$. If we substitute this expression into the wave equation, we end up with the Helmholtz equation.

$$(k^2 + \vec{\nabla}^2)\vec{E} = 0 \tag{3}$$

Note, that this equation is independent of the dimension of $\vec{E}$. As such, we will continue with the one - dimensional case. If we further assume the paraxial case, where the wavefront is restricted to a region close to the propagation axis, we can write our electric field as:

$$E(\vec{r}) = u(\vec{r})e^{-ikz} \tag{4}$$

Note, that while $u(\vec{r})$ depends on z, variation of z in u is assumed to be slower than in the exponential.

$$\left|\frac{\partial^2 u}{\partial z^2}\right| \ll k^2 u \tag{5}$$

$$\left|\frac{\partial u}{\partial z}\right| \ll ku \tag{6}$$

Plugging these into the Helmholtz equation, we get the paraxial wave equation

$$\left(\frac{\partial^2}{\partial x^2} + \frac{\partial^2}{\partial y^2}\right)u(r) - 2ik\frac{\partial u(r)}{\partial z} \approx 0 \tag{7}$$

Solutions to this equation are monochromatic waves closely confined to the axis of propagation, such as the transverse electric modes (TEM). The Gaussian beam (TEM_{00}) specifically can be obtained by inserting a trial solution into the paraxial equation.

$$u(\vec{\rho}, z) = u_0 \cdot \exp\left[-i\left(p(z) + \frac{k\rho^2}{2q(z)}\right)\right] \tag{8}$$

With $\vec{\rho} = x\vec{n}_x + y\vec{n}_y$. Inserting equation 8 into equation 7 and comparing terms of equal power in ρ, we get two coupled first order differential equations.

$$\frac{\partial q(z)}{\partial z} = 1 \tag{9}$$

$$\frac{\partial p(z)}{\partial z} = -\frac{i}{q(z)} \tag{10}$$

The solution for equation 9 is $q(z) = z + k$, with a constant k. If we now look at the $q(z)$ - dependence of equation 8, we see that for $q(z) \in \Re$, we have $|\exp\left[-ik\rho^2/\left(2q(z)\right)\right]| = 1$, the amplitude of the Gaussian beam is the same regardless of the distance from its axis, which is conflicting with the assumption of a spatially confined wavefront made earlier. As such $q(z)$ has to be complex and since we know $z \in \Re$, k has to be complex. We define k as $k = -iz_R$, where we call z_R the Rayleigh length.

2.1.2 Spot size of a Gaussian beam

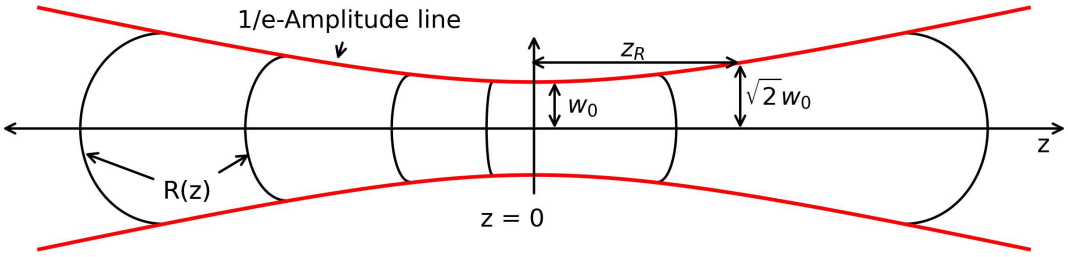

Figure 1: Side profile of the Gaussian Beam. For any given z, at a distance $w(z) = \rho$, the electric field amplitude of the beam drops by a factor of $1/e$ from its maximum. At z = 0 the beam has a minimal spot size of w_0, called beam waist and an infinite curvature R(z) resulting in an effectively planar wavefront, while for $z \to \infty$ the spot size $w(z)$ goes to infinity and the wavefront curvature $R(z) \to z$, resulting in a spherical wave front. Note, that at distance z_R from the waist, the Rayleigh length, the spot size increases by a factor of $\sqrt{2}$

By solving equation 9, we are already able to determine a number of important properties of the Gaussian beam, most importantly its spot size for arbitrary z and the shape of its wavefront. If we look at equation 8 for $z = 0$.

$$u(\vec{\rho}, z = 0) = u_0 \cdot \exp\left[-ip(z = 0) - \frac{k\rho^2}{2z_R}\right] \tag{11}$$

We now can define $w_0^2 := 2z_R/k = \lambda z_R/\pi$ as the waist of the Gaussian beam. It defines the $1/e$ - line of the transverse beam profile. A distance $|\vec{\rho}| = w_0$ from the beam axis the field amplitude drops to $1/e$ of its maximum magnitude at $\rho = 0$. If we rewrite $q(z)$ for arbitrary z we can write

$$\frac{1}{q(z)} = \frac{1}{z - iz_R} = \frac{z}{z^2 + z_R^2} + i\frac{z_R}{z^2 + z_R^2} =: \frac{1}{R} + i\frac{\lambda}{\pi w(z)^2} \tag{12}$$

Where R(z) and $w(z)$ can be expressed in w_0 and z_R as

$$R(z) = z\left[1 + \left(\frac{z_R}{z}\right)^2\right] \tag{13}$$

$$w(z) = w_0\sqrt{1 + \left(\frac{z}{z_R}\right)^2} \tag{14}$$

If we insert q(z) written in R(z) and $w(z)$ into Eq 8, we get

$$u(\vec{\rho}, z) = u_0 \cdot \exp\left[-ip(z) - i\frac{k\rho^2}{2R(z)} - \frac{\rho^2}{w(z)^2}\right] \tag{15}$$

This gives us some insight in the meaning of both $R(z)$ and $w(z)$. We see that $w(z)$ demarcates the $1/e$ Amplitude line of the Gaussian beam at arbitrary values of z, with w_0 being the special case of $w(z = 0)$ (see Figure 1). It is of note, that the Rayleigh length z_R defined in section 2.1.1 now has a physical meaning. It represents the distance z from the beam waist, where the spot size of the beam increases by a factor of $\sqrt{2}$ from the waist.
If we look at the term $\exp\left[-ik\rho^2/\left(2R(z)\right)\right]$, we can see that this term gives us a phase in dependence of the lateral distance from the axis of the Gaussian beam (see figure 1). We will talk more about this term in section 2.1.4

2.1.3 Gouy Phase

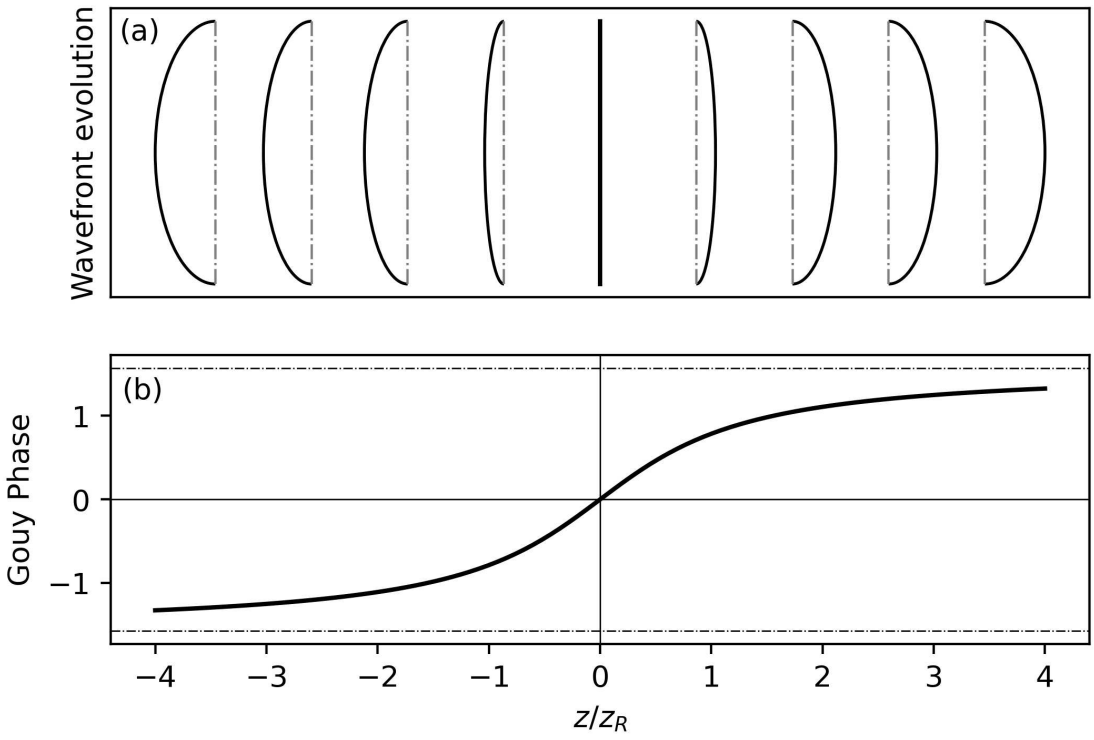

Figure 2: Visualisation of the Gouy-phase. (a) The black lines represent the evolution of the wavefront of a Gaussian beam, while the grey lines represent the wavefront of a planar wave. Near the center of the beam we can estimate the Gaussian beam with a planar wave, while for $r \to \infty$ the wavefront approaches a spherical wave. (b) z-dependence of the Gouy-Phase in units of z_R

Up till now we have ignored $p(z)$, since we were interested in the radial properties of the beam. If we insert $q(z)$ into equation 10 we get

$$\frac{\partial p(z)}{\partial z} = \frac{-i}{z - iz_R} \tag{16}$$

Integration yields

$$-ip(z) = -\ln\left(1 - i\frac{z}{z_R}\right) = -\ln\sqrt{1 + \left(\frac{z}{z_R}\right)^2} - i \cdot \tan^{-1}\left(\frac{z}{z_R}\right) \tag{17}$$

Equation 17 consists of two terms. The first term can be rewritten as $\ln(w_0/w(z))$. It represents the expected reduction in wavefront amplitude with z (see figure 3), while the second term $i \cdot \tan^{-1}(z/z_R)$ adds an extra phase shift dependent on z. It varies slowly compared to e^{-ikz}, changing from $-\pi/2$ at $z = -\infty$ to $\pi/2$ at $z = \infty$, as assumed for the paraxial case and changes mostly within one Rayleigh length of z = 0 (see figure 2 **b**). We call this phase the Gouy - Phase.

2.1.4 Summary

Inserting 12 and 17 into equation 8 we get the complete equation describing the electric field of the Gaussian Beam

$$E(\rho, z) = \underbrace{u_0 \frac{w_0}{w(z)} \exp\left[-\frac{\rho^2}{w(z)^2}\right]}_{\text{Longitudinal Amplitude/Spot size}} \cdot \underbrace{\exp\left[-ikz - i\zeta(z)\right]}_{\text{Longitudinal Phase}} \cdot \underbrace{\exp\left[-\frac{ik\rho^2}{2R(z)}\right]}_{\text{Radial phase}} \tag{18}$$

With $\zeta(z) = \tan^{-1}(z/z_R)$. This equation has already been split into phase- as well as amplitude/spot size contributions, which we will discuss separately in this chapter.

Amplitude and spot size

Normalizing the first term of equation 18 with respect to u_0, we get

$$\left|\frac{E(\rho, z)}{u_0}\right| = \frac{w_0}{w(z)} \exp\left[-\frac{\rho^2}{w(z)^2}\right] \tag{19}$$

Since the beam waist w(z) increases hyerbolically with distance z from the focal point with waist w_0, also the amplitude falls with $E_z/E_0 = w_0/w_z$ with $w_0/w(z) = 1/\sqrt{1 + (z/z_R)^2}$ (see figure 3). For the asymptote of the waist hyperbola $z \gg z_R$, we can approximate

$$w(z) = w_0 \sqrt{1 + \left(\frac{z}{z_R}\right)^2} \approx \frac{w_0 z}{z_R} \tag{20}$$

As such, we can for the asymptote of the waist hyperbola define a beam divergence angle in the far-field:

$$\phi = \frac{\partial w(z)}{\partial z} \approx \frac{w_0}{z} = \frac{\lambda}{\pi w_0} \tag{21}$$

The tighter a beam is focused, the faster it diverges.

Longitudinal and radial phase constituents of the Gaussian beam

The phase components of the Gaussian beam consist of the longitudinal - as well as radial phase. The total longitudinal phase - contribution of a Gaussian beam on its axis can be written as

$$\psi_l = kz + \zeta(z) \tag{22}$$

While the total radial phase contribution amounts to

$$\psi_r = \frac{k\rho^2}{2R(z)} \tag{23}$$

To set these terms into context, we now look at the total phase for $z \ll z_R$, $z \gg z_R$, as well as for arbitrary values of $z \neq 0$.

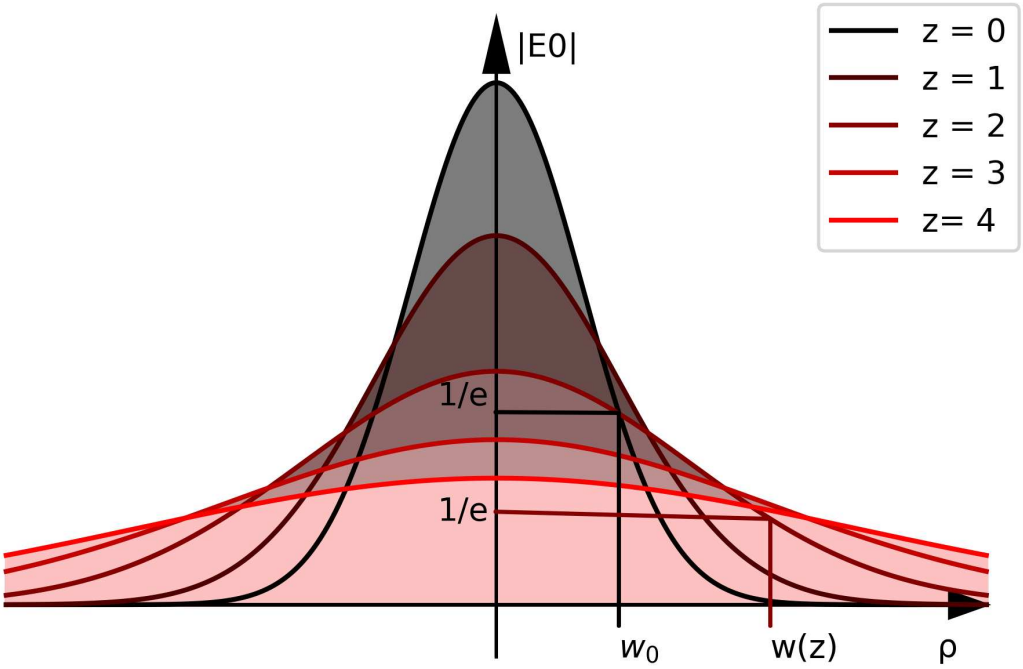

Figure 3: Transverse Gaussian Beam profile for different longitudinal positions z. Plotted is the magnitude of the electric field $|E|$ versus the transverse position ρ. With an increase in z, we can see an increase in beam diameter $w(z)$, as well as a decrease in Field amplitude to compensate for the increase in diameter and keep the total Flux of the beam constant with z.

For $z \ll z_R$, and $\rho \ll w_0$ $R(z) \approx z_R^2/z$, $\zeta(z) \to 0$. If we look at the total phase for this case, we get

$$\psi \approx kz + \frac{k\rho^2 z}{2z_R^2} = kz + \frac{z}{z_R}\frac{k\rho^2}{2z_R} = kz + \underbrace{\frac{z}{r_R}}_{\ll 1}\underbrace{\frac{\rho^2}{w_0^2}}_{\ll 1} \approx kz \tag{24}$$

This phase is characteristic of a plane wave, meaning that for small z, close to its waist, the Gaussian beam can be approximated by a plane wave (see figure 1). In this case both the radial phase term and the Gouy phase vanish.

Now we look at the opposite case $z \gg z_R$ with $z \gg \rho$, since we work under the assumption of a paraxial wave (see section 2.1.1). In this case $R(z) \approx z$ $\zeta(z) \approx \pi/2$, which gives us

$$\psi \approx kz + \frac{\pi}{2} + \frac{k\rho^2}{2z} = \frac{\pi}{2} + k \cdot \left(z + \frac{\rho^2}{2z}\right) \tag{25}$$

Note that the term $z + \rho^2\,(2z)$ describes a sphere of radius z, phase-shifted by a factor of $\pi/2$ by the Gouy phase. As such, for $z \gg z_R$, we get a spherical wavefront seemingly originating at a point source $z = 0$, $\rho = 0$. For arbitrary distances $z \neq 0$ from the waist of the beam, we can write (ignoring the slowly varying Gouy Phase).

$$\psi = kz + \frac{\rho^2 k}{2R(z)} = k\left(z + \frac{\rho^2}{2R(z)}\right) \tag{26}$$

In case of $r \ll R(z)$ (paraxial case), the surfaces of constant phase $z + \rho^2\,(2R(z)) = const.$ can be approximated as the equation of a sphere with radius R. Looking at equations 24, 25 and 26 we can assume that outside of $z \ll z_R$, the wave fronts of the Gaussian beam consist of circles of radius $R(z)$, which we as such call the wavefront curvature. Note, that these beams are shifted at the center by the slowly varying Gouy phase to compensate for their increasing curvature.

Intensity and Power

The Intensity I of the Gaussian beam is given by:

$$I(\rho, z) = \frac{c\epsilon_0}{2}|E(\rho, z)|^2 = I_0 \left(\frac{w_0}{w(z)}\right)^2 \exp\left[-\frac{2\rho^2}{w(z)^2}\right] \tag{27}$$

Here ϵ_0 is the vacuum permittivity, and as such $I_0 = u_0^2 c\epsilon_0/2$ is the maximum intensity of the beam. Since $w(z_R) = \sqrt{2} \cdot w_0$, the maximum intensity of the beam at distance z_R from its waist is exactly half of the intensity at the waist. The total power P_0 of a Gaussian beam is given by

$$P_0 = \int_0^\infty \mathrm{d}\rho I(\rho, z) 2\pi\rho = \frac{I_0 \pi w_0^2}{2} \tag{28}$$

Allowing us to express the maximum beam intensity as a function of power $I_0 = \frac{2P_0}{\pi w_0^2}$, which lets us rewrite the beam Intensity as

$$I(\rho, z) = \frac{2P_0}{\pi w(z)^2} \exp\left[-\frac{2\rho^2}{w(z)^2}\right] \tag{29}$$

2.2 Optical Tweezers

Optical tweezers, first experimentally realized by Arthur Ashkin in 1986 [34], trap particles using the optical gradient force. Optical tweezers can be used for particles, from single atoms ($\approx 10^{-10}$m) up to $\approx 3\times10^{-5}$ m [35]. The tweezer forces can be described by Lorentz-Mie theory [36], for any of spherical particles, or by T-matrix methods [37], for particles of arbitrary shape. Here, we will focus on the Rayleigh approximation, in the Rayleigh scattering and dipole approximation, which fits well for Si and SiO_2 particles smaller than 300 nm in diameter and a laser wavelength of 1550 nm.

2.2.1 Ray optics approximation

The ray optics approximation can be used when the tweezer wavelength λ is much smaller than the particle diameter $\lambda \ll d$ [38]. It explains the momentum transfer from rays of light to the particle due to refraction. When a ray of light is refracted by the particle, it changes its momentum. The difference between the old and new momentum of the ray of light will then, due to momentum conservation, be transferred to the particle. To get a better idea of this, let us look at figure 4 a) and b). It represents a spherical particle positioned slightly off center in an unfocused Gaussian beam (but not yet a tweezer). The section of the beam passing through the particle will be refracted, as represented by the black arrows in the picture, but since the particle is off-center, we have an intensity gradient along the particle. The refraction of the beam on the particle along this Intensity gradient imparts a force on the particle which acts along the Intensity gradient of the beam. Depending on the ratio of the indices of refraction of the particle n_p and the surrounding environment n_m, the resulting force is either conservative, keeping the particle at the center of the beam ($n_p > n_m$) or the opposite is true, the particle are pushed out of the beam ($n_p < n_m$).

To understand the axial trapping force figure 4 c), d) show us a particle at the center, but out of focus of the tweezer. While the lateral force components cancel each other out, the axial forces guide the particle to the focal waist.
Additionally, one has to also consider the reflected, and the absorbed rays of light. For a particle of refractive index n_p, in a medium n_m this results in a total force

$$F_{\text{tot}} = \frac{n_m P_i}{c}\vec{e_i} - \frac{n_m P_r}{c}\vec{e_r} - \frac{n_p P_t}{c}\vec{e_t} \tag{30}$$

Here P_i, P_r and P_t are the power of the incident light, the sum of the reflected rays and the sum of the transmitted rays respectively, while $\vec{e_i}$, $\vec{e_r}$ and $\vec{e_t}$ are the unit vectors pointing in the direction of the incident light, the sum of reflected rays and the sum of transmitted rays respectively.

Note that the absorption is included in this equation as the difference between incident and transmitted/reflected light. It is of interest that both reflected, as well as absorbed light push the particle in the propagation direction of the beam, which requires a the conservative axial force to be large enough to counteract both reflection, as well as absorption[39]. This can be done by, for example using wavelengths or particles, which maximize transparency, or adding a second, counter-propagating beam to the tweezer, counteracting the non-conservative force of the first one.
Finally, let us look at the ratio n_p/n_m of the indices of refraction of both the particle and its surrounding medium. To construct a tweezer as depicted in figure 4, it is important, that $\frac{n_p}{n_m} > 1$, to ensure, that the gradient forces generated by the refracted light push the particle to the region of highest intensity, while for $\frac{n_p}{n_m} < 1$ the particle seeks the region of lowest intensity (see section 2.2.2) [40].

2.2.2 Dipole Approximation

The electric dipole approximation, valid for $\lambda \gg d$ is based on the assumption that the electric field is homogeneous across the particle. This allows us to treat the trapped particle like a dipole in a homogeneous electric field. The following calculations are based on [18, 41, 42]. The force acting on matter per unit volume is given by the Lorentz law:

$$f = \rho\vec{E} + \vec{J} \times \vec{B} \tag{31}$$

Here ρ and $\vec{J}$ are the charge density, as well as current density respectively induced by the external electric field respectively. Now, we introduce the dielectric polarisation density of the particle $\vec{P}$. Using $\vec{P}$, we can express ρ and $\vec{J}$ as $\rho = -\nabla\vec{P}$ and $\vec{J} =$
$partial\vec{P}/\left(\partial t\right)$, thus turning the Lorentz law into

$$f = \vec{P}(\nabla\vec{E}) + \frac{\partial\vec{P}}{\partial t} \times \vec{B} \tag{32}$$

Note, that we used the divergence theorem to arrive at equation 32.

$$-\int_V (\nabla\vec{P})\vec{E}\mathrm{dV} = \int_V \vec{P}(\nabla\vec{E})\mathrm{dV} - \underbrace{\int_S \vec{E}\vec{P}\mathrm{dS}}_{=0} \tag{33}$$

If the force acts uniformly over the whole particle, then it follows from equation 33 $(\nabla\vec{P})\vec{E} = \vec{P}(\nabla\vec{E})$. The term $\int_S \vec{E}\vec{P}\mathrm{dS}$ of this equation can be taken as 0, because we assume the polarisation of the particle to be defined for only one point $\vec{P}(\vec{r}) = P\delta\left(\vec{r} - \vec{r_0}\right)$, where r_0 doesn't lie on surface S.

If we use the identity $\nabla(\vec{E}\vec{E}) = 2 \cdot \vec{E}\nabla\vec{E} + 2 \cdot \vec{E} \times (\vec{E} \times \vec{E})$, and Maxwell's equations and express $\vec{P}$ as $\vec{P} = (\epsilon_p - \epsilon_m) \cdot \vec{E}$ in terms of the total electric field $\vec{E}$, we can rewrite equation 32 as:

$$f = (\epsilon_p - \epsilon_m)\left(\frac{1}{2}\nabla(\vec{E} \cdot \vec{E}) + \frac{\partial}{\partial t}(\vec{E} \times \vec{B})\right) \tag{34}$$

This gives us an expression of the force per unit volume acting on the particle, which is solely dependent on the electromagnetic field, as well as on the permittivity (ϵ) of the particle and its surrounding medium, respectively.

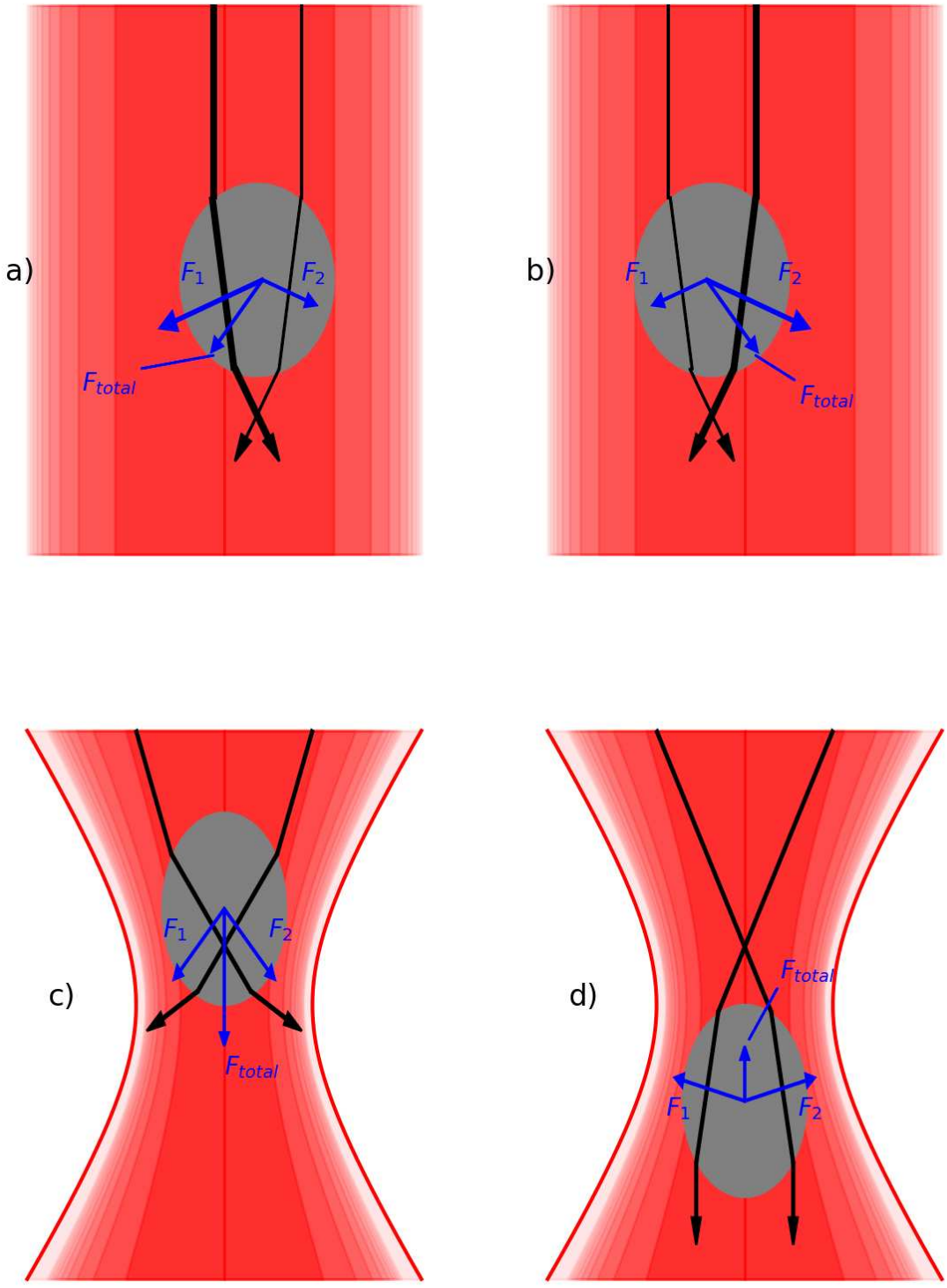

Figure 4: Schematic of the ray optics approximation. Note, that figure a and b are showing an unfocused beam of light for ease of representation, but the principle remains the same as for the focused beam. **(a)** Particles to the right of the center of the beam experience an intensity gradient creating a force acting on the particle, pushing it to the left. **(b)** Same as (a), particles moving out of the center of the beam are pushed into back into the center. The unfocused beam still exerts a force of the particle in the direction of beam propagation. **(c)** In case of a particle in the center of a focused of the beam before its focus the optical gradient forces pushing the particles lateral to the beam nullify each other. Additionally we have a longitudinal force pushing the particle in direction of the focus. This force can be see an a sum of the force of the reflected/absorbed light and the momentum change of the refracted rays of light. **(d)** For a particle after focus, the lateral forces acting on it cancel each other, just like (c). Different than (c) however, the refraction of light in this case imparts momentum opposite to the beams propagation direction to the particle.

For a particle much smaller than the wavelength, the electric field can be assumed to be uniform, allowing us to assume constant force density over the whole particle (effectively $\vec{F} = V\vec{f}$, for a particle of volume V)

$$\vec{F} = \vec{f} \cdot V = V \cdot \frac{3\epsilon_m}{\epsilon_p + 2\epsilon_m} \cdot (\epsilon_p - \epsilon_m) \left(\frac{1}{2} \nabla (\vec{E} \cdot \vec{E}) + \frac{\delta}{\delta t} (\vec{E} \times \vec{B}) \right) \tag{35}$$

Here the factor $3/(\epsilon_p/\epsilon_m + 2)$ is caused by the local field of polarised charges inside the particle induced by the external field. The local field can be written as $\vec{E}_{\text{lok}} = \vec{E} + \vec{E}_{\text{ind}}$, where $\vec{E}$ represents the external homogeneous electric field inside the particle and $\vec{E_{\text{ind}}}$ represents the field of local polarisation charges in the particle.

If we now assume a spherical particle we get for $\vec{E_{\text{lok}}}$:

$$\vec{E_{\text{lok}}} = \vec{E} + \frac{\vec{P}}{3\epsilon_m} = \vec{E} + \frac{\epsilon_p - \epsilon_m}{3\epsilon_m} \vec{E} = \frac{\epsilon_p + 2\epsilon_m}{3\epsilon_m} \vec{E} \tag{36}$$

With $\frac{\vec{P}}{3\epsilon_m}$ representing the field of the polarisation charges of a sphere (Lorentz - Field). If we now assume a spherical particle $V = \frac{4\pi r^3}{3}$ and insert this term into equation 35, then we get a total force F:

$$\vec{F} = 4\pi r^3 \epsilon_m \left(\frac{\epsilon_p - \epsilon_m}{\epsilon_p + 2\epsilon_m} \right) \left(\frac{1}{2} \nabla (\vec{E} \cdot \vec{E}) + \frac{\partial}{\partial t} (\vec{E} \times \vec{B}) \right) \tag{37}$$

We can simplify this expression by defining the static polarisability of a sphere α:

$$\alpha = 4\pi \epsilon_m r^3 \left(\frac{\frac{\epsilon_p}{\epsilon_m} - 1}{\frac{\epsilon_p}{\epsilon_m} + 2} \right) \tag{38}$$

$$\vec{F} = \alpha \left(\frac{1}{2} \nabla (\vec{E} \cdot \vec{E}) + \frac{\partial}{\partial t} (\vec{E} \times \vec{B}) \right) \tag{39}$$

If we now calculate the time average of the force, we get:

$$\langle \vec{F} \rangle = \frac{1}{2} \cdot \text{Re}\{ \underbrace{\alpha \frac{1}{2} \nabla (\vec{E_0} \vec{E_0^*})}_{\text{Gradient Force}} - \underbrace{2\alpha i \omega \vec{E_0} \times \vec{B_0^*}}_{\text{Scattering Force}} \}. \tag{40}$$

Here $\vec{E_0}$ and $\vec{B_0}$ represent the complex time-independent amplitude of the electric, and magnetic field respectively. Equation 40 consists of two terms, the gradient force, as well as the scattering force of the tweezer. Let us first look at the scattering force:

$$\vec{F}_{\text{scat}} = \text{Re}\{-i\omega\alpha\mu_m \vec{S}\} = -\omega\mu_m \text{Im}\{\alpha\}\vec{S}. \tag{41}$$

Here $\vec{S}$ is the poynting vector $\vec{S} = \vec{E} \times \vec{B}/\mu_m$. If we now look at the average power radiated from a time-harmonic radiation of a dipole $|p_0|^2 \omega k^3 / (12\pi\epsilon_m)$ and compare it with the scattered power $1/2\text{Re}\{-i\omega\alpha\vec{E_0}\vec{E_0}^*\} = -\omega/2\text{Im}\{\alpha\}|\vec{E_0}|^2$ we arrive at the imaginary component of the polarisability

$$\text{Im}\{\alpha\} = -\frac{k^3}{6\pi\epsilon_m} |\alpha|^2 \tag{42}$$

Which we then can use to express the scattering force

$$\vec{F}_{\text{scat}} = \frac{\omega k^3 |\alpha|^2 \mu_m}{\pi\epsilon_m} \vec{S} = \frac{8\pi}{3c} k^4 r^6 \left(\frac{\epsilon_p - \epsilon_m}{\epsilon_p + 2\epsilon_m} \right)^2 \vec{S} \tag{43}$$

Here c generally corresponds to the velocity of light in the medium surrounding the particle. This force acts in the direction of tweezer propagation. If we define the scattering cross section as

$$\sigma_{\text{scat}} = \frac{8\pi}{3} k^4 r^6 \left(\frac{\epsilon_p - \epsilon_m}{\epsilon_p + 2\epsilon_m} \right)^2 \tag{44}$$

then we can rewrite equation 43 as:

$$\vec{F}_{\text{scat}} = \frac{\sigma_{\text{scat}}}{c} I(\rho, z) \vec{e_z} \tag{45}$$

Here $I(z, \rho)$ is defined as the intensity of the Gaussian beam at the particle position.

Now, let's discuss the gradient force and its Intensity dependence.

$$\vec{F}_{\text{grad}} = -\frac{\alpha}{4} \nabla |\vec{E}|^2 = -\frac{\alpha}{2\epsilon_0 nc} \nabla I(\rho, z) \tag{46}$$

The term $\nabla I(\rho, z)$ defines the vector components of the gradient force. The gradient force acts along the intensity gradient of the maximal light field. In case of $\alpha > 0$ (essentially $\epsilon_p/\epsilon_m > 1$), the gradient force is conservative, always pointing along the field gradient to the point of highest intensity I and essentially trapping particles in the focus of an optical tweezer. For $\epsilon_p/\epsilon_m < 1$, $\alpha > 0$. In this case the gradient force becomes non-conservative and particles seek low-intensity regions of the light field.

A nanoparticle trap needs to satisfy $\vec{F}_{\text{grad}} + \vec{F}_{\text{scat}} + \vec{F}_{\text{env}} = 0$. Here $\vec{F}_{\text{env}}$ is a summary of all environmental forces, such as gravity or gas pressure caused by Brownian motion, etc. Here, we will ignore $\vec{F}_{\text{env}}$ and only consider the scattering force, as well as the gradient force. Comparing Equation 43 and the z-component of Equation 46, we arrive at a ratio β between the scattering and gradient forces:

$$\beta = \left| \frac{\vec{F}_{\text{scat}}}{\vec{F}_{\text{grad}}} \right| \propto k^4 r^3 \epsilon_m^2 \left(\frac{\epsilon_p - \epsilon_m}{\epsilon_p + 2\epsilon_m} \right) \tag{47}$$

The ratio of scattering and gradient forces are dependent on particle radius, wave vector of the tweezer, electric permittivity of both particle and surrounding medium. The dependence of equation 47 on the particle radius leads to an effective size limit for trappable particles, since the scattering force of a tweezer beam pushes particles above a certain size out of the trapping region. To trap particles above a certain size, it is necessary to add a counterpropagating second beam of light counteract the scattering force (i.e. double sided Tweezer, see section 2.2.1. This effectively creates a standing wave and changes the trapping conditions to $\vec{F}_{\text{grad}} + \vec{F}_{\text{env}} = 0$.

2.3 Detection of nanoparticles through scattered light

Optical detection of nanoparticles can be realized in a multitude of ways, including interference based schemes, such as forward and backward scattering detection [43, 44], cavity-based detection methods, such as homodyne or heterodyne detection [45, 46], as well as detection of laterally scattered light [11, 47, 48]. In our experiments, we collected the (Rayleigh-)scattered light of nanoparticles crossing a tweezer with a scattering fiber.

2.3.1 Rayleigh scattering of a nanoparticle in a double - sided tweezer

We want to approximate the scattering properties of a single nanoparticle inside a double - sided tweezer using the Rayleigh approximation (see section 2.2.2). For a tweezer of wavelength $\lambda = 1550\,\text{nm}$, the Rayleigh approximation holds true for particles with diameters smaller than $400\,\text{nm}$ [19, 49]. Since our nanoparticle diameters in our experiments only go up to $300\,\text{nm}$, we operate in the Rayleigh regime. The total Rayleigh scattering cross section of a spherical particle is given by [50]

$$\sigma_{\text{scat}} = \frac{k^4|\alpha|^2}{6\pi} \tag{48}$$

Here k is the wave vector of the scattered light and alpha the polarisability of the particle. The electric field amplitude of a double -sided tweezer consisting of two counter-propagating Gaussian beams of the same polarisation is given by:

$$E_{\text{total}}(\rho, z) = E_+(\rho, z) + E_-(\rho, z) = E_{\text{Gauss}}(\rho, z) + E_{\text{Gauss}}(\rho, -z) \tag{49}$$

Here E_{Gauss} refers to the electric field of a Gaussian beam (see Equation 18), where the negative z component of the second beam implies propagation antiparallel to the first beam. Writing 49 using 18, we arrive at the term:

$$E_{\text{total}}(\rho, z) = 2u_0 \frac{w_0}{w(z)} \exp\left[-\frac{\rho^2}{w(z)^2}\right] \cos\left(kz + \zeta(z) + \frac{k\rho^2}{2R(z)}\right) \tag{50}$$

Here we used $w(-z) = w(z)$, $R(-z) = -R(z)$ and $\zeta(-z) = -\zeta(z)$ (see Equations 13, 14 and 17). The phase-term of equation 50 corresponds to a plane standing wave with wave vector k near the beam waist $z = 0$ (for $z \to 0$, $R(z) \to \infty$ and $\zeta(z) \to 0$). We want to know how well this approximation works for $z \neq 0$, but still close to the beam waist.

Since the Gouy-phase varies slowly compared to the wavefront propagation by definition (see section 2.1.1) we can ignore the influence of this term on our assumption of a plane standing wave. The magnitude of the wavefront curvature phase term in equation 50 relative to the plane wave term can be approximated by setting $kz = k\rho^2/2R(z)$. Reforming this equation gives us the distance from the propagation axis at which the wavefront curvature becomes comparable to the plane wave component $\rho(z) = \sqrt{2z^2 + 2z_R^2}$. If we compare this result to the corresponding beam radius in equation 14, we observe a linear dependence on z for both parameters. Since there is no clear trend to be observed, we numerically approximate the effect of wavefront curvature on the standing wave. Using the tweezer-parameters of our setup (see section 4) and setting $z = 2z_R \approx 1.7\,\text{mm}$, we arrive at $\rho(2z_R) = \sqrt{10} \cdot z_R \approx 2.7\,\text{mm}$, while for our waist, we have $w(z) = \sqrt{5} \cdot w_0 \approx 4.6\,\mu\text{m}$. We can see that $w \ll \rho$ and as such the influence of wavefront curvature on the standing wave is negligible. Consequentially, we can write the intensity of the standing wave as:

$$I(\rho, z) = \frac{c\epsilon_0}{2}|E_{\text{total}}(\rho, z)|^2 = \frac{4P_0}{\pi w(z)^2} \exp\left[-\frac{2\rho^2}{w(z)^2}\right] \cos(kz)^2 \tag{51}$$

Combining equations 48 and 51, we can write the total scattered power a nanoparticle inside a standing wave as:

$$P_{\text{scat}} = I(\rho, z) \cdot \sigma_{\text{scat}} = \frac{2k^4|\alpha|^2 P_0}{3\pi^2 w(z)^2} \cdot \exp\left[-\frac{2\rho^2}{w(z)^2}\right] \cos(kz)^2 \tag{52}$$

This is just the total amount of light scattered by the particle. When using a cleaved fiber to collect scattered light, only a fraction $f = NA/4\pi$ of the light is actually collected. Here NA represents the numerical aperture of the fiber.

2.3.2 Behaviour of particles in a tweezer

With this wave function we can construct some example cases of how a particle would behave in the standing wave. The figures in this section are mostly reproduced and adapted from [19, 51].

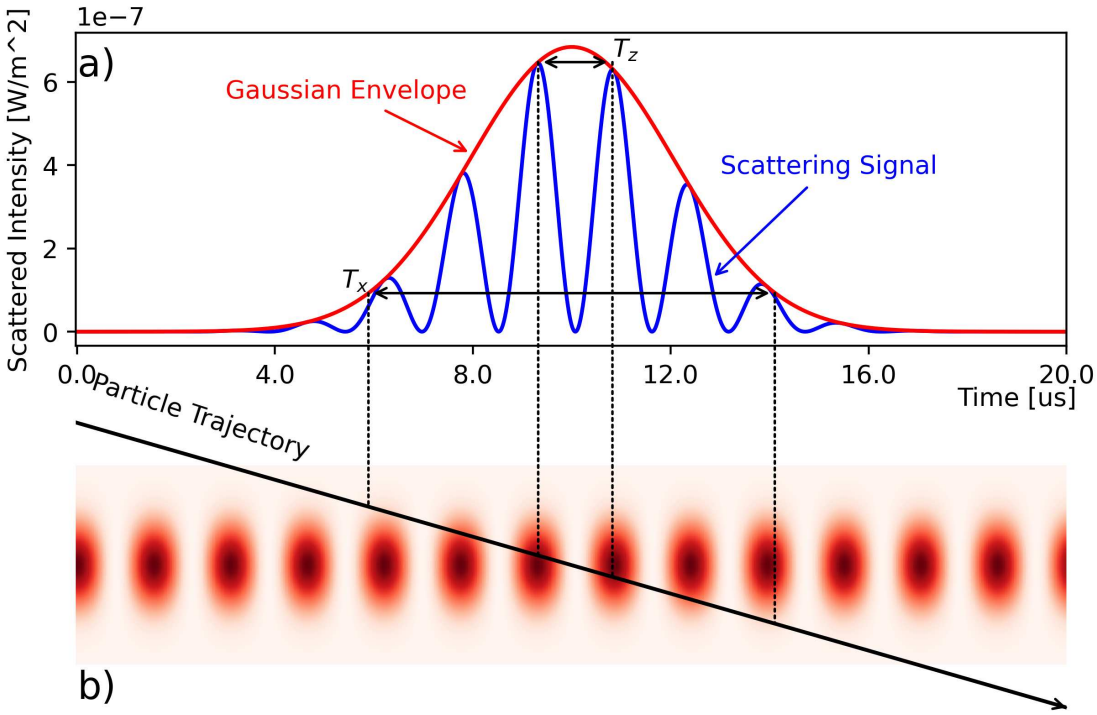

Figure 5: **a)** Simulated scattering signal of a particle of r $= 150$ nm passing through the standing wave of a double-sided tweezer with waist $w_0 = 20,55\mu m$ and wavelength $\lambda = 1550$ nm. **b)** The passage of the particle through the beam results in a Gaussian envelope modulated by an additional sinusoidal signal due to its traversal of the standing wave. The $1/e^2$-width of the Gaussian envelope T_x gives a forward-velocity of the particle of $v_x = 5m/s$, while the repetition rate of the sinusoidal modulation of the scattering signal T_z lets us calculate the transversal velocity in direction of the tweezer of $v_x = 0.5m/s$.

First, we assume the nanoparticle passing the tweezer to have high kinetic energy (i.e. a fast moving particle). In figure 5, we see an example trajectory of such a particle, accompanied by the corresponding scattering signal as a function of time. The kinetic energy of the particle along the tweezer is much greater than the forces of the light field. As such one can ignore the forces of the light field and assume that it moves with constant velocities v_x and v_z through the tweezer. If we take equation 52 and assume a constant beam diameter $w(z) \approx w_0$ over the section of the beam the particle crosses, then we get:

$$P_{\text{scat}} = P_{\text{scat}} = \underbrace{\frac{2k^4|\alpha|^2 P_0}{3\pi^2 w_0^2}}_{\text{Constant}} \underbrace{\exp\left[-\frac{2\left(v_x T_x\right)^2}{w_0^2}\right]}_{\text{Gaussian}} \underbrace{\cos\left(k v_z T_z\right)^2}_{\text{Modulation}} \tag{53}$$

This equation is two dimensional. For the three dimensional case, we would have to include an additional term $\exp\left[-2\left(v_y T_y\right)^2 / w_0^2\right]$, though the only difference this would make is a variance in the magnitude of the Gaussian envelope. With this equation, we can correlate the shape of the scattering signal with the particle velocities. The $1/e^2$-width of the Gaussian envelope T_x of equation 53 correlates to the waist of the tweezer, which allows us to calculate the velocity of the particle in the x-direction $v_x = w_0/T_x$. Similarly, one can use the sinusoidal modulation of the Gaussian envelope to determine the z-velocity of the particle. If we have $\cos\left(k v_z T_z\right)^2 = \cos\left(2\pi v_z T_z/\lambda\right)^2$, we have a period π (π the period of a squared cosine) with a periodicity $\pi = 2\pi v_z T_z/\lambda$, which we can rewrite to $v_z = \lambda/2T_z$, giving us the particle velocity in tweezer-direction.

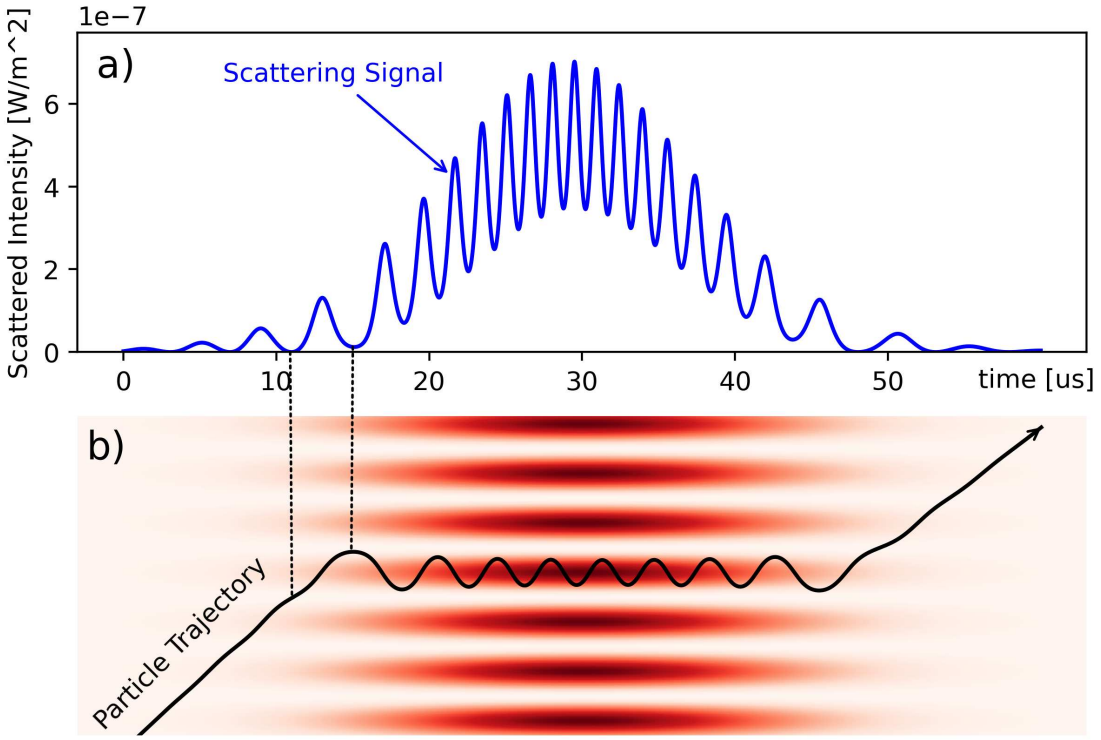

Figure 6: **a)** Simulation of the scattering signal of a slow-moving nanoparticle traversing the same tweezer as in figure 5. When entering the tweezer, the particle has an initial velocity of $v_x = 1\frac{m}{s}$, $v_x = 0.2\frac{m}{s}$. **b)** Simulated particle trajectory corresponding to the scattering signal. The particle is one-dimensionally trapped in one anti-node of the standing wave during the transit time. Comparing a) and b), we associate the non-zero minima of the scattering signal with the oscillations of the particle in the anti-node, while minima close to zero are associated with the particle passing through the nodes of the standing wave.

We now consider a nanoparticle with low kinetic energy (i.e. a slow particle). In case of a slow

particle, the forces discussed in section 2.2.2 are large enough to influence the particle trajectory inside the tweezer. As depicted in figure 6, the particle initially travels along the standing wave, before eventually being one-dimensionally trapped in one of the anti-nodes of the tweezer. The particle has enough momentum in the xy-direction to transverse the cavity, but it is trapped along the cavity axis. The trapped particle now oscillates along the intensity maximum of the anti-node in the z-axis, resulting in non-zero minima of the scattering signal. Eventually, as the particle passes the center of the tweezer the field intensity decreases, allowing the particle once again to travel along the standing wave. The optical forces acting on the particle are conservative in nature and as such the kinetic energy of the particle will not change due to the trapping, though a change in propagation direction can occur depending on the number of oscillations in the anti-node (see figure 6).

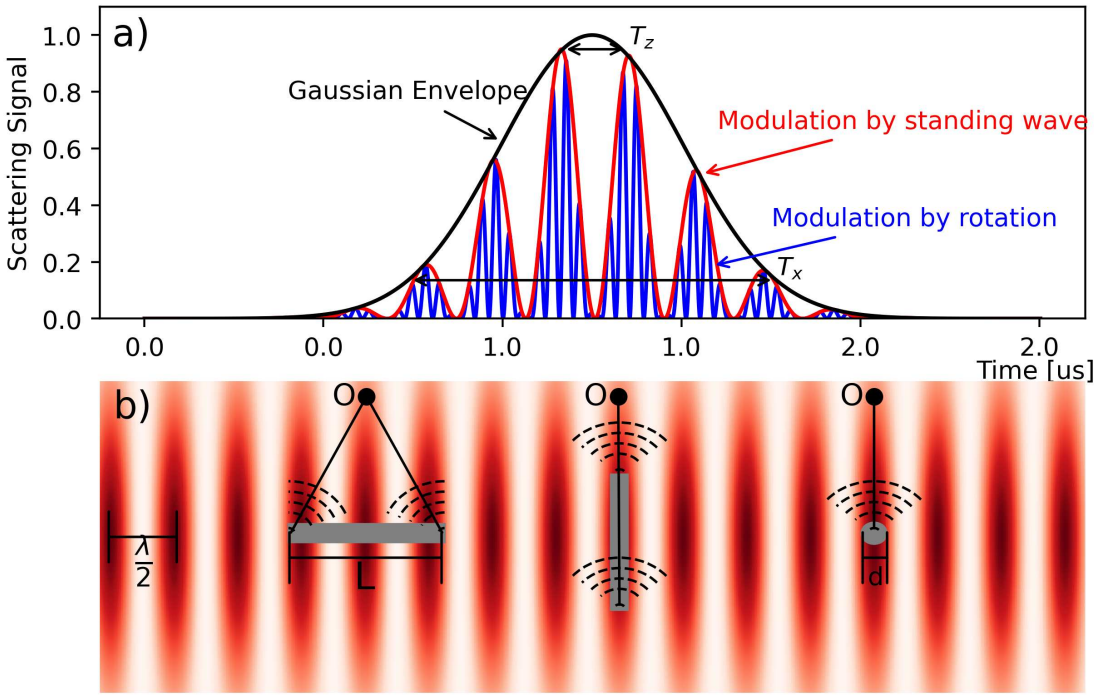

Figure 7: **a)** Simulated, normalised example trajectory of an asymmetric particle cluster with high aspect ratio. The rotation of the cluster adds another modulation frequency to the scattering signal. **b)** Qualitative depiction of modulation frequencies of scattering signals caused by asymmetric particles in a standing wave using the example of a rod with $L >> d$ and L on the order of λ. In case the rod is oriented along the wave vector $\vec{k}$ of the standing wave, every point along the rod experiences a different phase of the electric field $\vec{E}$, causing the light scattered of different sections of the rod to be out of phase, thereby reducing the scattered intensity. For a rod aligned to the observer, a similar phenomenon occurs. All sections of the rod experience the same phase, but the scattering occurs along the length of the rod, causing the scattered waves to not add up in phase and thereby suppressing the scattering signal. When the rod is oriented orthogonal to both observer and field vector $\vec{k}$, both electric field $\vec{E}$, as well as scattered waves from different parts of the rod are in phase, thereby maximising the scattering signal arriving at the observer.

Finally, we should consider the case of particle clusters. In our experiments we use prefabricated symmetrical particles with sizes falling within the Rayleigh approximation, but during sample preparation and volatilisation, it is possible for multiple particles to form nonspherical clusters. Their scattering properties can no longer be approximated by Rayleigh approximation and are strongly dependent on size, shape and orientation to the observer, making a quantitative discussion difficult. The most important property of the asymmetric particles are modulation frequencies resulting from the rotation of asymmetric particles in the light field. A nanoparticle in the Rayleigh regime $d \ll \lambda$ scatters in phase, while a cluster with $d \approx \lambda$ scatters out of phase,

reducing the power of the scattered light field. For clusters of high aspect ratio this effect leads to additional modulation frequencies depending on their rotational frequencies (compare figure 7 **a)**). Waves of scattered light belonging to different sections of a cluster will interfere with each other, reducing the scattering intensity. In case of an asymmetrical particle, it can be the Rayleigh-regime in two dimensions (e.g. two or more particles sticking together in a rod-like structure), while exceeding it along the third. In this case, it is possible for Rayleigh scattering to occur with the right cluster orientation, while for other alignments the scattered waves are out-of-phase. The out-of-phase scattering results in reduced scattering intensity (see figure 7 **b)**). A more quantitative discussion of the scattering formalism for thin rods or disks can be found in [52].

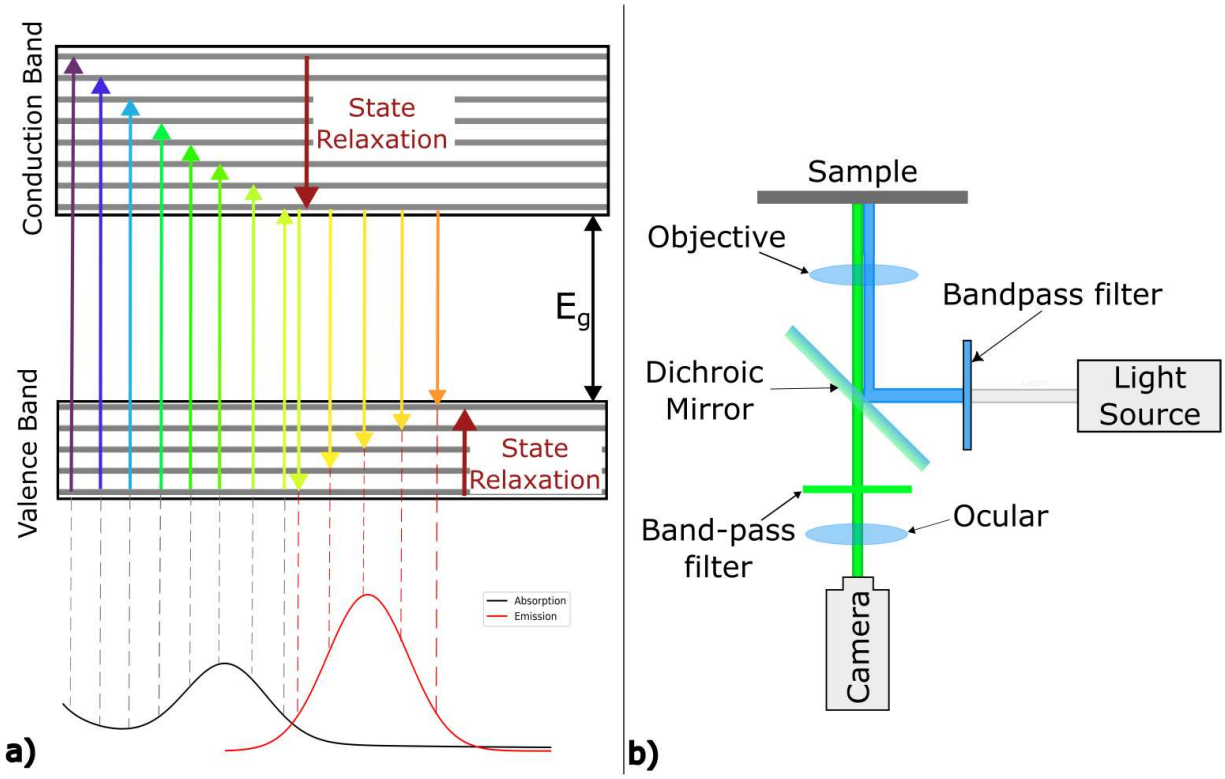

Figure 8: **a)** Schematic operating principle of fluorphores. The band gap between the conduction and valence band, allows for photon absorption as long as a minimum energy threshold has been exceeded. After photon absorption the excited electrons and hole carriers are out of thermodynamic equilibrium in their respective bands and as such seek to return to their respective lowest-energy state. This process occurs on a much faster timescale than the emission of a photon, which returns the electron to the valence band [58]. As such, when a photon is emitted, its energy will be reduced as compared to the absorbed one. **b)** Operating principle of a fluorescent microscope. The light source sends full-spectrum light to a band-pass filter, letting only light capable of exciting the sample (in blue) pass. The filtered light is reflected by a dichroic mirror and focused on the sample by the objective. The sample fluoresces, emitting light of a shorter wavelength (in green), capable of passing through the dichroic mirror and a second excitation filter, after which it is focused on the camera by the ocular.

2.4 Fluorescence microscopy

To characterise a particle source it is necessary to investigate the substrate on which the particles are applied before volatilisation. To this length, we use fluorescence microscopy [53, 54] in combination with fluorescent nanoparticles [55] or quantum dots [56, 57] to detect the particle spread on the substrate.

Fluorescence microscopy distinguishes itself from other, similar methods of microscopy by achieving a strong contrast between sample and environment while being easy to set up. This is achieved by exploiting the emission properties of fluorphores, as seen in figure 8 **a**. Fluorescence microscopy as seen in figure 8 **b** highlights a fluorescent sample by illumination at its center absorption wavelength, which results in emission of light at a longer wavelength. This allows us to filter the background light reflected by the microscopy slide and collect only the fluorescence of the sample through the camera. Magnification of the sample is achieved through a lens system. A fraction of the fluorescent light is caught by the objective lens, which for collimates it in the direction of the ocular. After being filtered by a dichroic mirror, as well as an emission band-pass filter, the collimated light passes through the ocular, which focuses the emitted light on a camera or an eyeport to observe the sample. The angular magnification of a fluorescent microscope as

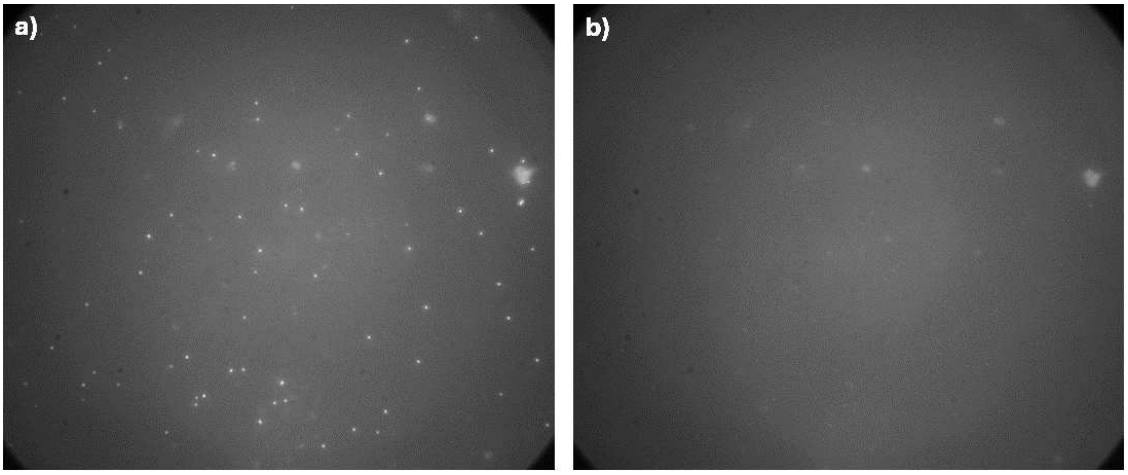

Figure 9: Green fluorescent $300\,\mathrm{nm}$ SiO_2 - nanoparticles in a fluorescent microscope with hundredfold magnification **a)** directly after setting the sample in focus **b)** twenty seconds after setting the sample in focus.

depicted in figure 8 **b)** (assuming the sample is in focus of the objective) is given by:

$$M_{\mathrm{tot}} = M_{\mathrm{ob}} \cdot M_{\mathrm{oc}} \tag{54}$$

Where M_{ob} and M_{oc} are the magnification of the objective and ocular respectively given by $M_{\mathrm{ob}} = d_1/f_{\mathrm{ob}}$, and $M_{\mathrm{oc}} = d_2/f_{\mathrm{oc}}$, with f_{ob}, f_{oc} being the focal lengths of the objective/ocular, and d_1, d_2 the distance between objective and ocular and the distance between ocular and camera respectively.

A common issue in fluorescence microscopy is the decrease of the observed fluorescence of the sample over time, also known as photobleaching. This effect is more pronounced in organic fluorophores and at higher illumination intensities and can be caused by a wide array of photochemical processes dependent on the fluorophore [59]. It limits the effective observation time and makes it harder to observe single nanoparticles (see figure 9). Photobleaching cannot be circumvented, but can be mitigated by using fluorophores with higher photochemical stability, working with higher integration times at lower power or increasing the scanning speed of the sample.

3 Volatilisation schemes

Developing source techniques has remained an experimental challenge ever since the introduction of high precision experiments needing reliable sources, such as (both electromagnetic and optical) particle trapping/cooling, mass interferometry, as well as mass spectroscopy experiments [20, 60, 61]. Here, we will discuss the two desorption methods we investigated in the scope of this thesis.

3.1 Laser-induced acoustic desorption

The common problems source technologies face are the fragmentation and/or clustering of particles during sample preparation/volatilisation, controlling the variable particle charges, as well as velocities [62, 63]. Different source techniques improve upon different issues of particle volatilisation and as such, we will briefly compare three laser-induced desorption methods, their respective benefits, as well as drawbacks and explain, why we chose to explore LIAD as a source technique.

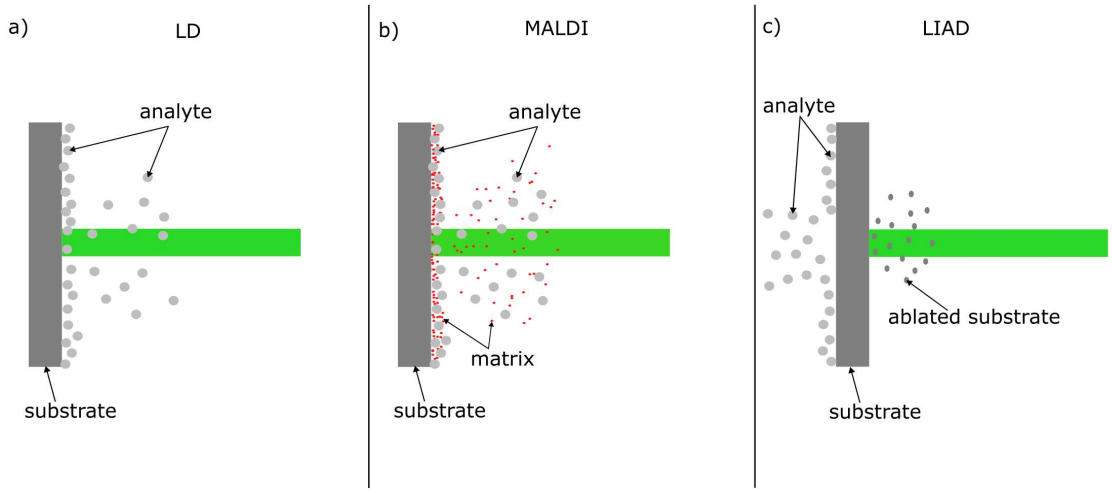

Figure 10: Schematics of different Laser-induced desorption methods. **a** Laser-desorption(LD) volatilizes particles by direct irradiation via laser. **b** Matrix-assisted Laser-desorption ionisation(MALDI) adds a matrix to LD, which works as an intermediary between laser and analyte. **c** Laser-induced acoustic desorption(LIAD) volatilizes particles by irradiating the backside of the substrate with a pulsed laser and shaking the analyte of.

3.1.1 Laser desorption(LD)

A substrate is directly irradiated using a (pulsed-) laser beam, leading to the desorption of the analyte (see figure 10 **a)**). The velocity distribution of the LD particle-plume varies with the properties of the desorption laser and the the optical properties of the analyte. Both thermal Maxwell-Boltzmann distributions [64], as well as bimodal distributions with one peak in shape of a Maxwell-Boltzmann distribution have been observed [65].

The direct interaction of the desorption laser with the sample causes thermal heating, leading to a high degree of fragmentation. This can be counteracted using desorption lasers of shorter pulse length [23, 66]. Additionally, the plume of desorbed particles will be partially ionized by the desorption beam. While LD is sometimes used for the mass spectroscopy of small molecules in conjunction with special substrates, [67] its high fragmentation rate and broad charge distribution makes it unsuitable for experiments needing a reliable source of identical particles.

3.1.2 Matrix-assisted Laser desorption ionisation (MALDI)

MALDI was first experimentally demonstrated in 1988 by Karas and Hillenkamp [68]. It introduces a matrix to the Laser desorption method (see figure 10 **b**). This matrix consists of small

organic molecules with strong absorption at the laser wavelength. It is applied together with the analyte on the substrate and later ablated by a (pulsed) desorption laser similar to LD. This leads to the indirect desorption of the analyte through the matrix [69]. The velocity distribution of the MALDI-plume takes the form of a Maxwell-Boltzmann distribution [70].

The indirect desorption process allows for a decoupling of the absorption properties of the analyte from the laser choice [71]. This significantly increases the available analyte choices and desorption efficiency compared to the direct laser desorption. Additionally, the indirect interaction of light and analyte reduces the particle fragmentation rate as compared to direct laser desorption, making it a technique often used in Mass spectroscopy [72]. The particle plume of MALDI consists of a mixture of matrix, as well as analyte particles, necessitating separation, if a pure analyte source is needed.

3.1.3 Laser-induced acoustic desorption (LIAD)

LIAD has a pulsed desorption beam irradiate the back-side of a thin substrate and "shake" particles of the front side of the analyte (figure 10 **c**). The exact mechanisms of LIAD are still unclear, with the source technique showing properties typical for both thermal and acoustic desorption. There are multiple theories regarding the working principles of LIAD, such as the propagation of thermal or acoustic waves through the substrate imparting energy on the analyte particles, or internal strains in the crystallized analyte layer being released through surface deformations generated by the desorption laser [73] (see sections 3.1.4, 3.1.5).

The velocity distribution of the desorbed particle plume is independent of the desorption laser power and wavelength and takes the form of a Maxwell-Boltzmann velocity distribution. The particles experience delays of tens of microseconds between the impact of the desorption laser and the emission of particles from the substrate. These delays are an order of magnitude greater as compared to the ones of a LD or MALDI source and result in broader LIAD velocity distribution [74, 75].

With LIAD, the mean particle velocity depends on the substrate material, as well as thickness rather than the desorption laser power [76]. The laser power instead influences the desorption- and fragmentation rate of the analyte [74, 77]. Compared to MALDI and LD, LIAD does not feature direct interaction of the desorption Laser and analyte. This makes the method applicable to both photosensitive and thermally labile sample materials [62], over a wide range of particles without the need for a matrix [11, 29, 61, 78].

When LIAD was first experimentally demonstrated by Golovlev et. al. in 1997 [29], the effect was thought to be caused by acoustic waves propagating through the substrate. These waves were thought to cause surface displacement and thereby shake the particles of the substrate.

Characterisation of LIAD sources has brought up a number of contradictions to this theory, however. The mean delay of the particle volatilisation after laser impact has been reported to be in the range of tens of microseconds while the time needed for an acoustic wave to traverse the sample has only been observed to be $1\,\mu s$ [77, 79]. Further, the magnitude of particles desorbed via LIAD as a function of time has the form of a Maxwell-Boltzmann distribution, which would not be possible in case of acoustic desorption. An acoustic shock wave spreading through the substrate foil would dissipate after several round trips, effectively leading to multiple, much sharper peaks in the particle velocity distribution [74].

The independence of the desorbed particle velocity of the laser power similarly excludes the volatilisation of particles through the propagation of thermal waves. Additionally, the desorption

of thermally labile compounds without fragmentation would be impossible if LIAD were a thermal desorption method [74, 80].

When measuring temperature and surface deformation caused by the desorption laser, there is a noticeable discrepancy between experimentally measure parameters and required values for the observed velocity distributions typical for LIAD [81, 82]. Furthermore, the particle velocity distribution was observed to be independent of the laser power. These observations, as well as the small fragmentation rate of LIAD as compared to the thermal desorption of direct LD led to the proposal of a new mechanism for LIAD by Zinovev et. al. in 2007 [75]. In this new model the analyte would form crystals on the substrate, with the desorption occurring based on the release of internal strain in the crystals primed by a combination of acoustic, as well as thermal waves. This could explain the independence of the velocity from the laser power, since said velocity would instead be dependent on the internal strain of the analyte [83]. This model runs into issues when considering samples with low analyte concentration incapable of forming crystals.

In the next sections the interactions between the laser and substrate are discussed.

3.1.4 Thermal waves in the substrate and their propagation

A laser irradiating a metal surface couples to the free electrons of the surface and accelerates them. This process is called inverse Bremsstrahlung. After acceleration, the electrons collide with the ion lattice, transferring their energy to it. This series of processes consequentially heats the impact point of the laser [84].

This process can be described in one dimension by the following set of differential equations [85, 86]:

$$C_i \frac{\partial T_i}{\partial t} = \gamma \left(T_e - T_i \right) \tag{55}$$

$$C_e \frac{\partial T_e}{\partial t} = \frac{\partial}{\partial z} \left(\kappa_e \frac{\partial T_e}{\partial z} \right) - \gamma \left(T_e - T_i \right) + S(z,t) \tag{56}$$

With $T_{i/e}$ and $C_{i/e}$ being the temperature and heat capacity of the ion lattice (index i) and the electrons (index e) respectively. The factor γ describes the coupling of free electrons and ions and κ_e is the electron thermal conductivity used to write the heat flux $Q(z,t) = -\kappa_e \partial T_e / \partial z$ in terms of the temperature. A laser with intensity I(t) would transmit the power S to the electrons:

$$S(z,t) = I(t) A \mathrm{e}^{-\alpha z} \tag{57}$$

With absorptivity A and material absorption coefficient $\alpha = \frac{4\pi n_I(\lambda)}{\lambda}$ of the substrate. Here $n(\lambda) = n_R(\lambda) + i \cdot n_I(\lambda)$ is the complex index of refraction. The material absorption coefficient α is the inverse of the material penetration depth $\delta = 1/\alpha$, which is used to quantify the penetration of the light field into the substrate.

These equations represent the dynamics of a thermal wave in a fixed substrate, but depending on the pulse length of the heating laser they can be simplified further. If we assume a nanosecond laser, the time τ_i the ion lattice needs to reach thermal equilibrium with the free electrons is much smaller than the pulse length τ. Effectively, we have $T_e = T_i = T$, which allows us to rewrite equations 55 and 56 into [86]:

$$C_e \frac{\partial T}{\partial t} = \frac{\partial}{\partial z} \left(\kappa_e \frac{\partial T}{\partial z} \right) + I(t) A \mathrm{e}^{-\alpha z} \tag{58}$$

Equation 58 is called inhomogeneous heat conducting equation and can be solved analytically for the right boundary conditions. We assume the substrate before the laser pulse possesses a

homogeneous temperature $T(z,0) = T_0$. Then, we look at the penetration depth of the heat wave after time τ [86, 87]:

$$l = \sqrt{D\tau} \tag{59}$$

Here $D = \kappa_e / C_i$ is the heat diffusion coefficient of the surface material. The penetration depth indicates the depth the thermal wave has penetrated into the metal and assuming a nanosecond laser (i.e. $4\,$ns to $10\,$ns pulse length) and heat diffusion coefficient typical for metals (see section 3.1.6), we have penetration depths of less than $1\,$µm. This allows us to assume the substrate to be semi-infinite in the time frame of the laser pulse, effectively $T(d,t) = T_0$ for a substrate thickness d. Lastly, we need to define the boundary conditions for equation 58. The temperature evolution at the interface of the substrate with the laser can be described by [88]:

$$\kappa_e \left.\frac{dT}{dz}\right|_{z=0} = \sigma_{\mathrm{SB}} \cdot \epsilon_S \left(T(z,t)^4 - T_0^4\right)\big|_{z=0} - I(t)A \tag{60}$$

Here $\sigma\epsilon \left(T(z,t)^4 - T_0^4\right)|_{z=0}$ represents the heat loss of the metal through radiation as per the Stefan Boltzmann law with σ_{SB} and ϵ_S being the Stefan Boltzmann constant and the surface emissivity respectively. The term $-I(t)A$ represents the heating of the metal through the laser and $\kappa_e \, dT/dz|_{z=0}$ represents the total heat flux of the metal. Note that for high laser intensities heat loss through Stefan Boltzmann radiation is negligible compared to the laser heating and as such can be neglected, giving us:

$$\kappa_e \left.\frac{dT}{dz}\right|_{z=0} = -I(t)A \tag{61}$$

Using equation 61 together with $T(d,t) = T_0$ (due to the assumption of a semi-infinite substrate as above), as well as $T(z,0) = T_0$, we can solve equation 58 and get [87]:

$$T(z,t) = T_0 + \sqrt{\frac{D}{\pi}} \frac{A}{\kappa_e} \int_0^t dt' \frac{I\left(t - t'\right) \exp \frac{-z^2}{4Dt'}}{t'^{\frac{1}{2}}} \tag{62}$$

Equation 62 represents an analytical solution to the temperature distribution in a substrate of a thickness of over $1\,$µm irradiated by a ns laser in one dimension and of homogeneous temperature before irradiation. This equation holds true for any t, but if we are interested in the evolution of the temperature in the metal after the pulse ($t > \tau$), we can write equation 62 as [87]:

$$T(z, t > \tau) = \frac{2AI_0\sqrt{D}}{\kappa} \left[\sqrt{t} \cdot \mathrm{ierfc}\left(\frac{z}{2\sqrt{Dt}}\right) - \sqrt{t-\tau} \cdot \mathrm{ierfc}\left(\frac{z}{2\sqrt{D(t-\tau)}}\right) \right] \tag{63}$$

Here I_0 is the peak laser power and ierfc(x) is [83]:

$$\mathrm{ierfc}(x) = \frac{1}{\sqrt{\pi}} \left[e^{-x^2} - x(1 - \mathrm{erf}(x)) \right] \tag{64}$$

with erf(x) being the error function.

3.1.5 Acoustic waves in the substrate caused by laser ablation

Irradiating a substrate with a laser of sufficient power causes rapid heating of the substrate. This results in evaporation of the substrate surface, with the evaporated material forming a plasma plume. The recoil pressure (which we will call ablation pressure from now on) of the plasma plume is the cause of an acoustic shock wave inside the substrate [89].

Ablation pressure depends on a multitude of factors, such as environmental pressure, properties of the target material and interaction of the ablation plume with the background gas/ablation

laser. Due to stark case-by-case differences in the interaction between laser and substrate, there doesn't exist a general model describing the recoil pressure on the substrate over a long range of intensities [83]. As such, the relation between the laser intensity I and the ablation recoil pressure p_a on the substrate is conventionally characterized using a mechanical coupling coefficient [90]:

$$C_m = \frac{p_a}{I} = \frac{|\vec{p}|}{E_L} \tag{65}$$

Here $|\vec{p}|$ represents the magnitude of the momentum imparted on the substrate by laser ablation and E_L the laser pulse energy.

When observing the behaviour of C_m as a function of the laser intensity, one can divide laser ablation into two regimes. At lower intensities, the laser is able to directly interact with the target, making the interaction primarily dependent on material properties, as well as laser intensity For higher intensities on the other hand, the ablated particle plume shields the substrate, getting ionised by the ablation laser, which effectively reduces the laser intensity. [90–92] The high intensity regime in vacuum starts out with an optimal intensity I_{opt}, allowing for maximal intensity-momentum coupling, which then falls with increasing laser I power as [92–94]:

$$C_m = \Gamma \left(\frac{I}{I_{\text{opt}}} \right)^{-n} \tag{66}$$

Here Γ and n are material constants. I_{opt} is dependent on the material, but has been determined to be in the range of $1.2 \times 10^8\,\text{W/cm}^2$ to $2 \times 10^9\,\text{W/cm}^2$ for most metal surfaces [90, 93]. This is significantly lower than the Intensities used in our experiment. As such, we operate in the high intensity regime.

In the low intensity regime where ionisation of the plume is negligible, ablation of a surface by a laser can be treated like thermal vaporisation from a hot surface. This allows one to use the saturation pressure of the plasma plume to calculate the ablation recoil pressure. [95] When increasing the laser intensity, one eventually reaches a critical point in saturation pressure. This marks the start of the high intensity regime, where ablation pressure is almost independent of the target material. For laser intensities in the range of GW/cm^2, one can estimate the ablation pressure using the model of Gospordy et. al [96]:

$$P_{\text{abl}} = 7.26 \times 10^8 \cdot I^{\frac{3}{4}} \lambda^{-\frac{1}{4}} \tau^{-\frac{1}{8}} \tag{67}$$

Here I is expressed in GW/cm^2, λ in μm and τ in ns.

We now have a measure of the pressure acting on the substrate and are interested in its propagation. We approximate the substrate foil as a thin plate, where the ablation recoil pressure induces vibrations in the foil. The following derivations regarding the vibrations of a thin plate have been taken from [97–99].

The equation governing the vibration of the thin plate is given by:

$$D\nabla^4\zeta(x,y,t) + 2\rho h \frac{\partial^2 \zeta(x,y,t)}{\partial t^2} = f(x,y,t) \tag{68}$$

With $D = Eh^3/12\,(1-v^2)$, where E is Young's Modulus, v the Poisson ratio, h the plate thickness, ρ its material density and f the force per unit volume acting on the plate. We assume the edges of the plate to be clamped, resulting in the following boundary conditions:

$$\zeta(0/L_1, y, t) = \zeta(x, 0/L_2, t) = 0 \tag{69}$$

n	m	ω_{nm}
1	1	4171
1	2	10430
2	1	10430
2	2	16687
2	3	27116
3	2	27116
3	3	37546

Table 1: Eigenfrequencies in Hz for a Ti-foil of thickness $h = 5\mu\mathrm{m}$ with $L_1 = L_2 = 5\mathrm{mm}$

$$\frac{d\zeta(0/L_1, y, t)}{dt} = \frac{d\zeta(x, 0/L_2, t)}{dt} = 0 \tag{70}$$

Here L_1 and L_2 are the dimensions of the plate in the x and y direction respectively.

$f(x, y, t)$ in equation 68 lasts only as long as the laser pulse τ, so we describe the impact the force has on the plate in two different regimes. First, we will look at times long after the laser pulse ($t \gg \tau$), allowing us to use the homogeneous equation with $f(x, y, t) = 0$. This can be done by separating $\zeta(x, y, t) = g(x, y)\xi(t)$, changing equation 68 into:

$$D\left(\nabla^4 g(x, y)\right)\xi(t) = -2\rho h g(x, y)\frac{\partial^2 \xi(t)}{\partial t^2} \tag{71}$$

Separating xy-dependent and time dependent parts of the equation gives us:

$$\frac{D}{2\rho h} \cdot \frac{1}{g(x, y)}\left(\nabla^4 g(x, y)\right) = \frac{-1}{\xi(t)}\frac{\partial^2 \xi(t)}{\partial t^2} = \omega^2 \tag{72}$$

Here ω^2 is a constant independent of x, y or t. If we solve the spatial component $g(x, y)$ of equation 72 with the given initial conditions we arrive at the natural modes $W_{\mathrm{nm}}(x, y)$ and natural frequencies ω_{nm}:

$$W_{\mathrm{nm}}(x, y) = \sin\left(\frac{n\pi x}{L_1}\right)\sin\left(\frac{m\pi y}{L_2}\right) \tag{73}$$

$$\omega_{\mathrm{nm}} = \sqrt{\frac{\pi^4 D}{2\rho h}}\left(\frac{n^2}{L_1^2} + \frac{m^2}{L_2^2}\right) \tag{74}$$

Where $n, m \in \mathbb{N}_{\neq 0}$ are natural numbers. It is of note, that solutions such as $W_{\mathrm{nm}}(x, y) = \cos\left(n\pi x/L_1\right)\cos\left(m\pi y/L_2\right)$ containing one or more cosine of $g(x, y)$ are eliminated by the initial condition $\zeta(0/L_1, y, t) = \zeta(x, 0/L_2, t) = 0$. Solving the time-dependent part of equation 72 and combining it with $W_{\mathrm{nm}}(x, y)$ and ω_{nm} gives us a general solution of:

$$\zeta(x, y, t) = \sum_{n=1}^{\infty}\sum_{m=1}^{\infty} W_{\mathrm{nm}}\left(A_{\mathrm{nm}}e^{iw_{\mathrm{nm}}t} + B_{\mathrm{nm}}e^{-iw_{\mathrm{nm}}t}\right) \tag{75}$$

Here A_{nm} and B_{nm} are dependent on the initial conditions and the orthogonality of the Fourier components in $W_{\mathrm{nm}}(x, y)$ [97]. Generally, equation 75 represents a superposition of standing sine waves confined to the plate surface. This is represented by a quantisation of eigenfrequencies ω_{nm} for different n and m as given in table 1.

Now that we have the equations modelling the behaviour of a thin plate vibrating without any external force acting on it, we want to solve equation 68 during the interaction with the laser ($t < \tau$). For a strongly focused laser acting on a comparatively big plate, one can assume the force to only act on one point of the surface $f_{\mathrm{nm}}(x, y, t) = \delta\left(x - L_1/2\right)\delta\left(y - L_2/2\right)f_{\mathrm{nm}}(t)$. We have already seen that free vibrations of a thin plate can be split into natural modes solved by

the eigenfrequencies, so we assume the driven case to be similar and split the driving force into components n and m acting on corresponding natural modes.

Splitting $\zeta(x,y,t)$ into $\zeta(x,y,t) = \sum_{n=0}^{\infty}\sum_{m=0}^{\infty}\tilde{W}_{\mathrm{nm}}(x,y)\xi_{\mathrm{nm}}(t)$, we assume the xy-dependent component to be the normalised natural modes of equation 68.
The normalised natural modes are defined using the the natural modes of equation 73:

$$\tilde{W}_{\mathrm{nm}}(x,y) = N_{\mathrm{nm}} \cdot W_{\mathrm{nm}}(x,y) \tag{76}$$

Here $N_{\mathrm{nm}} = -nm\pi/8\rho h L_1 L_2$ is a normalisation constant. $\tilde{W}_{\mathrm{nm}}(x,y)$ for odd n and m satisfies:

$$\int_0^{L_1}\int_0^{L_2} 2\rho h\tilde{W}_{\mathrm{nm}}(x,y)\mathrm{dx}\ \mathrm{dy} = 1 \tag{77}$$

We can use $1/\tilde{W}_{\mathrm{nm}}(x,y)\cdot D/2\rho h\left(\nabla^4\tilde{W}_{\mathrm{nm}}(x,y)\right) = \omega_{\mathrm{nm}}$ (see equation 72) to rewrite equation 68, similar to equation 72:

$$2\rho h\omega_{\mathrm{nm}}^2\tilde{W}_{\mathrm{nm}}(x,y)\xi_{\mathrm{nm}}(t) + 2\rho h\tilde{W}_{\mathrm{nm}}(x,y)\frac{\partial^2\xi_{\mathrm{nm}}(t)}{\partial t^2} = f_{\mathrm{nm}}(t)\delta\left(x-\frac{L_1}{2}\right)\delta\left(y-\frac{L_2}{2}\right) \tag{78}$$

The xy - dependence of this equation can be eliminated by integrating it over the whole surface of the thin plate. For this, we distinguish between solutions for odd and even n and m. For even n, m, integral 77 is 0, since driving force of the Laser acts at the center of the plate and as such doesn't contribute to these modes ($f_{\mathrm{nm}}(t) = 0$ for even n,m). For odd n, m on the other hand we get:

$$\frac{\partial^2\xi_{\mathrm{nm}}(t)}{\partial t^2} + \omega_{\mathrm{nm}}^2\xi_{\mathrm{nm}}(t) = F_{\mathrm{nm}}(t) \tag{79}$$

This equation can be solved by applying a Laplace transformation, giving us the temporal component of the solution:

$$\xi_{\mathrm{nm}}(t) = \frac{1}{\omega_{\mathrm{nm}}}\int_0^t \sin\left(\omega_{\mathrm{nm}}(t-t')\right)F_{\mathrm{nm}}(t')dt' \tag{80}$$

Recombining equation 80 with the normalised natural modes gives us the complete solution to 68 for $t < \tau$:

$$\begin{aligned}\zeta(x,y,t) = \sum_{n=1}^{\infty}\sum_{m=1}^{\infty}&\left[\frac{1}{\omega_{\mathrm{nm}}}\int_0^t \sin\left(\omega_{\mathrm{nm}}(t-t')\right)F_{\mathrm{nm}}(t')dt'\right]\\ &\frac{nm\pi}{2\rho h L_1 L_2}(-1)^{n+m}\sin\left(\frac{n\pi x}{L_1}\right)\sin\left(\frac{m\pi y}{L_2}\right)\end{aligned} \tag{81}$$

Equation 81 describes the vibrational motion of a plate driven by a force acting on a single point of the plate, which for long times $t \gg \tau$ transitions into harmonic oscillations as described in equation 75.

Internal strain in the analyte layer

A droplet of analyte solution applied to a substrate crystallizes during the evaporation of its solvent. These crystals are subject to stress, either due to imperfections during their growth, or external causes such as rapid temperature changes or vibrations of the substrate [82, 100]. These stresses have been postulated to be the reason for the volatilisation of particles in LIAD [75, 83]. While these stresses are highly dependent on the specific structure of the analyte layer, it is possible to make some estimations on the stress energy caused by acoustic and thermal waves during LIAD.

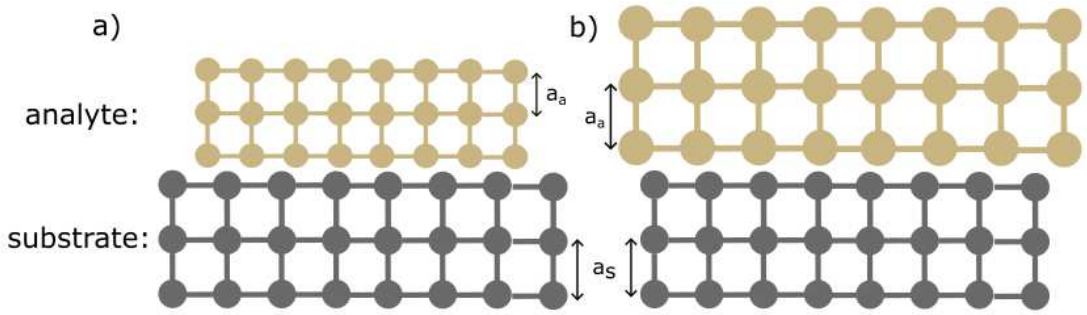

Figure 11: Lattice mismatch of the substrate (grey), as well as analyte (beige). In case **a**, the bigger substrate lattice stretches the smaller analyte lattice, while in case **b**, the opposite is the case.

There are three main contributors to stress on an analyte crystal lattice, one effecting the analyte during the crystallisation process, while the other two are caused by the thermal or acoustic waves of the desorption laser.

The application of the analyte on the substrate can lead to lattice mismatch stress. When applying analyte on the substrate, both the substrate, as well as the dried analyte form two seperate crystal lattices. The substrate and analyte lattices have different spacing (see figure 11), which results in the lattice of the drying analyte being either stretched or compressed in an effort to conform to the lattice of the substrate. The resulting stress in the analyte can be expressed as [101, 102]:

$$\sigma_M = 2\frac{E}{1-v}\frac{a_a - a_s}{a_s + a_a} \tag{82}$$

Here E is the Young modulus, v the poisson ratio, a_s and a_a the lattice constants of the substrate and analyte respectively. The lattice mismatch stress is purely a result of the different lattice constants of analyte and substrate and as such independent of external forces, although the resulting bound energy can contribute to particle desorption when primed by other forms of stress.

One such form of external stress is thermal mismatch stress. Thermal mismatch stress is a result of the difference in thermal expansion of substrate and analyte when subjected to thermal waves caused by laser desorption. Thermal mismatch stress is given by [100, 103]:

$$\sigma_{\mathrm{Th}} = \frac{E}{1-v}\left(\eta_s - \eta_a\right)\Delta T \tag{83}$$

Here ΔT is the temperature difference between the substrate before and after being irradiated by the desorbtion laser and η_s, η_a are the thermal expansion coefficients of the substrate and analyte film respectively.

Similar to the thermal mismatch stress, the acoustic wave caused by the desorption laser induces stress on the analyte. The deformation of the substrate caused by the acoustic wave results in a change in substrate curvature, causing a stress [82, 103]:

$$\sigma_d = \frac{E}{1-v}\frac{h_s^2}{h_a R} \tag{84}$$

Here R represents the substrate curvature and h_s, h_a the substrate and analyte film thickness respectively.

3.1.6 Thermal and acoustic properties of different substrates

Now that we have a basic understanding of the LIAD mechanism, we can make some estimations regarding the suitability of different substrate choices. A list of material properties for some of

	Copper	Tantalum	Titanium	Stainless Steel	Iron	Aluminium	SiO2
E[GPa]	129,8	185,7	105	200	211,4	71	70
v	0,343	0,342	0,34	0,27	0,293	0,33	0,17
ρ $[\frac{\text{g}}{\text{cm}^3}]$	8,94	16,65	4,43	7,8	7,87	2,7	2,65
η $[\frac{\text{ppm}}{\text{K}}]$	16,5	6,6	8,6	10,4	11,8	22,6	0,55
T_b [K]	2835	5632	3533	2900	3134	2743	2950
c_v $[\frac{\text{J}}{\text{kgK}}]$	385	140	520	460	450	900	680
κ $[\frac{\text{W}}{\text{mK}}]$	391	57	11,4	45	73	237	1,3
A ($\lambda = 532\,\text{nm}$)	0,244	0,22	0,401	0,433	0,382	0,077	0
$n_r(\lambda = 532\,\text{nm})$	1,04	1,09	0,27	2,75	2,65	0,77	2,1
$n_i(\lambda = 532\,\text{nm})$	2,59	5,24	4,61	3,8	3,34	6,08	0

Table 2: Material Constants of select substrate choices for LIAD. Sources: [87, 104]

the common substrate choices, such as titanium or aluminium is given in table 2.

Inserting these material constants in equations 81, 67 and 63 allows for the estimation of the behaviour of acoustic and thermal waves in the metal. In figure 12, we can see an estimate for the mechanical and thermal effects of the laser on the substrate.
The substrate material and thicknesses presented in figure 12 **b)** were used in our experiment.

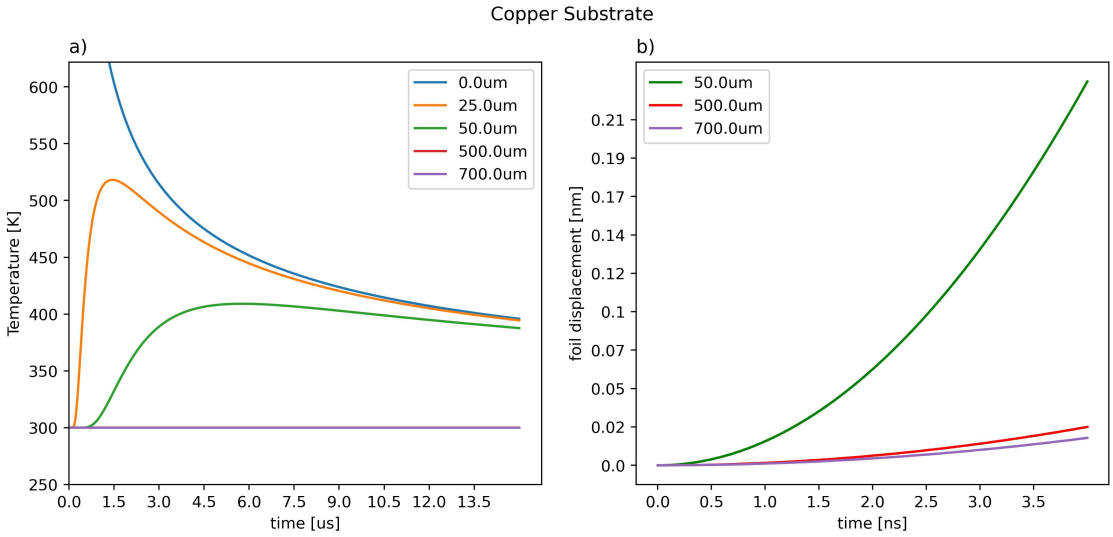

Figure 12: A estimation of the substrate temperature, as well as the foil displacement of copper of varying thicknesses when irradiated with a pulsed laser with $3\,\text{mJ}$ pulse energy and $4\,\text{ns}$ pulse length **a)** The thermal wave spreads through the substrate, notably heating the surface past the boiling point during the first few nanoseconds. For higher substrate thicknesses, there is no temperature change on the substrate front-side over the timescales of LIAD. **b)** Substrate displacement during the irradiation with the pulsed laser as calculated from equation 81.

While the ablation pressure is relatively independent of the material (see section 3.1.5) and in our experiments estimated to be about $P_{\text{abl}} \approx 2.357\,\text{GPa}$, the substrate displacement caused by the ablation pressure varies strongly with the material choice, as well as thickness (see also section 8). When combining the displacement values of 12 **b)** together with the pulse length of $4\,\text{ns}$, we get an upper estimate of the copper foil displacement velocity.

The thermal waves presented in figure 12 **a)** are calculated using equation 63 with an addi-

	Back temp. [K]	Front temp. [K]	Substr. disp. [nm]	Disp. velocity[$\frac{cm}{s}$]
$50\,\mu$m Cu		387	0,24	5,96
$500\,\mu$m Cu	9706	300	0,02	0,6
$700\,\mu$m Cu		300	0,02	0,43
$12.5\,\mu$m Ta		805	0,75	18,77
$50\,\mu$m Ta	29580	306	0,15	3,8
$100\,\mu$m Ta		300	0,08	2
$5\,\mu$m Ti		972.4	5,36	133,93
$50\,\mu$m Ti	99275	0,61	397	15,28
$100\,\mu$m Ti		300	0,31	7,8
$10\,\mu$m Steel		562	6,72	168,1
$50\,\mu$m Steel	48484	486	0,88	22,13
$100\,\mu$m Steel		322	0,45	11,21
$50\,\mu$m Fe		456	6,99	174,85
$100\,\mu$m Fe	33893	352	1,02	25,5
$200\,\mu$m Fe		300	0,51	12,9
$50\,\mu$m Al		356	7,79	194,61
$100\,\mu$m Al	4838	1,41	314	35,39
$500\,\mu$m Al		300	0,59	14,87

Table 3: Simulated values for ablation temperature, front-side temperature after $50\,\mu$s, maximal substrate displacement during the ablation laser pulse and the average foil displacement velocity during the laser pulse. We assumed a desorption laser with 4 ns pulse length, 3 mJ pulse power and a waist of $60\,\mu$m. The figures containing the spread of the temporal waves in the substrate, as well as the time-dependent foil displacement can be found in section 8

tional factor:

$$C_{\text{att}} = \left(\frac{I_0}{I_{\text{opt}}}\right)^{-n} \tag{85}$$

The factor C_{att} is a result of the ablation particle plume shielding the substrate with $n = 0.3$ and $I_{\text{opt}} \approx 5 \times 10^8\ W/cm^2$. It is based on the mechanical coupling constant and approximates the relative reduction in effective laser Intensity due to the ablation plume to be linear with the relative reduction of ablation pressure (see equation 65 and 67).

Results of our estimates regarding thermal, as well as acoustic waves can be found in table 3. We can observe significant differences in the acoustic waves dependent on their materials and thicknesses, Especially $5\,\mu$m titanium shows vibrations of a noticeably greater magnitude of vibrations followed by tantalum. Not unsurprisingly, we notice a significant decrease of the influence of thermal and acoustic waves for thicker substrates, with thicknesses of $\approx 100\,\mu$m or higher showing almost no change in front-side temperature and only minuscule changes in substrate position.
Comparing the substrate velocities calculated for $12.5\,\mu$m Ta to those measured in [83] or the substrate displacements for Al to [96], we can see our estimates are of the right order of magnitude.

The back-side temperatures for all substrates show different temperatures, but are consistently above the boiling point of the respective metal (see table 2), which is a prerequisite for laser ablation in the first place. The spread of the thermal waves in the metal has been simulated until thermal equilibrium has been reached or $50\,\mu$s have passed, after which the assumption of a plane thermal wave no longer holds (see section 3.1.4).

For thick samples no observable change to the front-side temperature occurs. Despite this, we could still observe particles when operating LIAD under the given conditions. This implies an

independence of the LIAD-mechanism from thermal effects.

3.1.7 Applications of Laser-induced acoustic desorption

In the previous sections, the principle of the LIAD process has been introduced and several underlying mechanisms have been discussed. Now, we discuss the advantages of LIAD in different fields of research and some practical examples. LIAD has two major fields of application. One in the mass spectroscopy for fragile compounds [73, 77, 79, 80, 105] and another in trapping of nanoparticles in vacuum. [48, 60, 106, 107]

Mass spectroscopy was the first field of application for Laser-induced acoustic desorption and it has been extensively used for the analysis of high-mass non-volatile particles, such as large saturated hydrocarbons, bio-molecules, or aromatics. [62, 76, 78, 108] Compared to MALDI, the most commonly used desorption mechanism in mass spectroscopy, LIAD has several major advantages. It is independent of matrices acting as an intermediary. This is of particular importance for analytes, which lack suitable matrices, such as hydrocarbons with no polar functional groups or nanoparticles. [76, 77] Additionally, desorbed particles up to 1000 u have been observed to be electrically neutral and of lower velocity than those desorbed with MALDI, [73, 79, 80, 109] allowing separate particle ionisation.

In the field of particle trapping, LIAD allows for clean loading of both optical, [60, 106] as well as electrical traps [107]. LIAD allows for low desorption plume densities depending on the sample preparation, making it an attractive loading technique for sensitive optical traps, such as optical cavities. Additionally, it has been demonstrated to as a loading technique for large, complex biological particles, such as viruses, bacteria or cells in conjunction with quadrupole-traps. [78, 110] The low particle velocities of LIAD are especially beneficial to trap loading in low-pressure environments, since it reduces the need for buffer-gas cooling [60, 106].

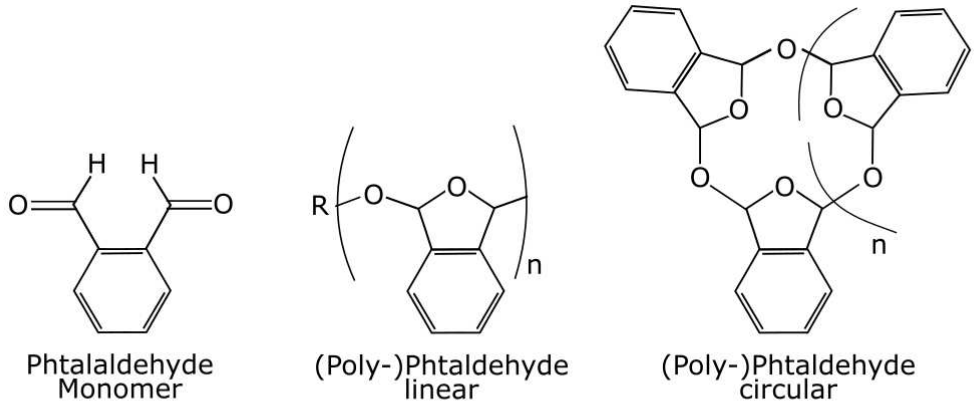

Figure 13: Molecular structure of Phtalaldehyde monomer (left), linear PPA (middle) and cyclic PPA (right). R represents the end-cap of the Polymer-chain.

3.2 (Poly-)phtalaldehyde(PPA)-sublimation

This section about (Poly-)phtalaldehyde(PPA)-sublimation will begin with a short overview of the properties of PPA, followed by the envisioned mechanism of volatilisation using PPA and its advantages in a high-vacuum environment, as well as the sublimation behaviour of PPA when irradiated by a laser, concluding with some simulations of the behaviour of particles after meltout.

3.2.1 Properties of PPA

Phtalaldehyde is an aromatic compound composed of a benzene ring and two carbonyl-groups. Its chemical formula is $C_6H_4(CHO)_2$. Polymerisation of Phtalaldehyde can be achieved in one of two ways, anionic polymerisation, as well as cationic polymerisation depending on the catalyst for the reaction [111, 112]. In case of anionic polymerisation, a nucleophile catalyst acts on one of the carbonyl-groups, leading to a restructuring of the Phtalaldehyde. This effectively causes a chain reaction which links many monomers together in a polymer chain. The catalyst acts as a neutral end-cap for one side of the resulting linear Polymer chain (see figure 13). The cathionic method of polymerisation uses a Lewis-acid, to polarise the carbonyl groups, allowing for Phtalaldehyde-chains to connect back to themselves, forming cyclical polymer chains as seen in figure 13 [111, 113].

The properties of linear PPA are heavily reliant on its end-caps, but in general anionic polymerisation offers stronger control of the length of the polymer chains at the cost of longer polymerisation times [111, 114]. Linear PPA depolymerizes rapidly at temperatures above -40°C without end-caps, making it susceptible to the breaking of polymer chains [111]. Cyclic PPA on the other hand was found to possesses long-term stability at room temperature and rapid polymerisation rates at the cost of little control over the polymer chain lengths. [113, 115]

Cyclic (Poly-)Phtalaldehyde, when heated past its depolymerisation temperature (see table 4) shows volatilisation of its breakaway monomers, causing the polymer to sublimate and dissolve without the formation of material droplets. This property of PPA has already been exploited for transient electronics, or nanolithography [116, 119–121] and is what makes it so attractive as a carrier substrate in a nanoparticle source.

Symbol	Quantity
n_r	1,63
n_i	4,8e-4
A($\lambda = 405\,$nm)	0,2
T_C(l-PPA) [°K]	233
T_C(c-PPA) [°K]	403
κ [$\frac{W}{mK}$]	0,25
c_p [$\frac{J}{kgK}$]	1500
ρ [$\frac{kg}{m^3}$]	1190
M [$\frac{kg}{mol}$]	0,134

Table 4: Properties of PPA at irradiation wavelength $\lambda = 405\,$nm and environmental temperature $T_e =$ 300°K. The thermal conductivity was taken from the values of poly(4-vinylphenol), since no thermal conductivity of PPA could be found. Sources: [115–118]

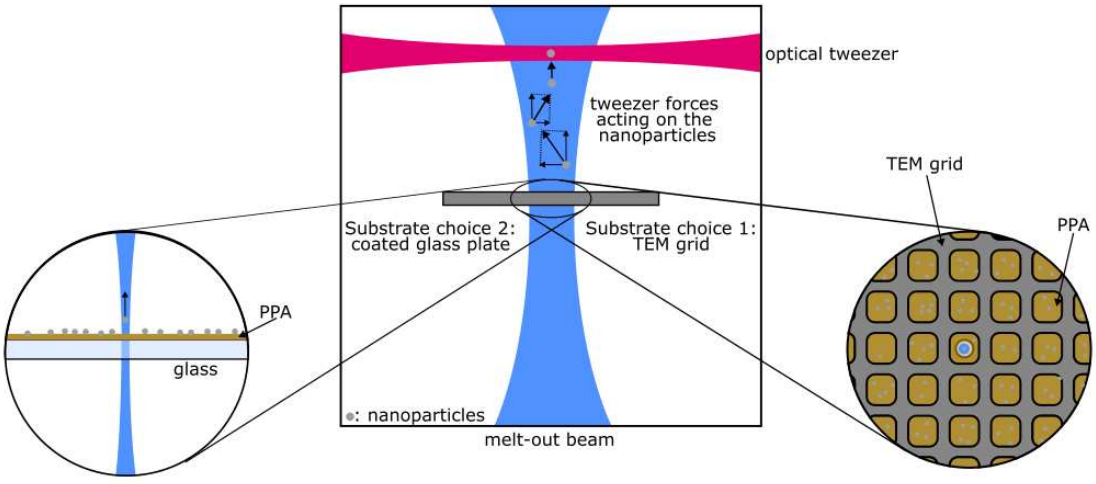

Figure 14: PPA sublimation scheme. A focused Gaussian beam is used to melt PPA dotted with nanoparticles locally. The beam acts as a particle guide similar to an optical tweezer, (compare section 2.2.2) guiding the nanoparticles to the detection beam. We studied two methods of sample preparation. In method one, we fill the holes of a TEM-grid with a thin layer of PPA, which is either already infused with nanoparticles or has nanoparticles applied to it retroactively via nebulisation. In method 2 PPA is applied to a transparent microscopy slide and then nebulised with nanoparticles.

3.2.2 PPA-sublimation as a volatilisation mechanism

When desorbing nanoparticles from solid surfaces, it is necessary to overcome the van der Waals forces that bind the nanoparticles to the surface. These forces scale inversely with distance $F_{\mathrm{vdW}} \propto 1/d$. [122] Consequently, manufacturing a PPA-substrate designed to sublimate during the desorption process allows for a drastic reduction of the van der Waals forces and for particle desorption with lower velocities, as well as lower internal temperatures.

A simple scheme of our desired desorption mechanism can be seen in figure 14. A PPA-substrate is dotted with nanoparticles and subsequently irradiated by a tightly focused Gaussian beam, which we will call the melt-out laser. The sublimation laser heats the PPA from below and causes depolymerisation on a time-scale of $\approx 1.2\,\mathrm{s}$ (see section 3.2.3). The PPA is sublimated, while the nanoparticles themselves are transparent to the sublimation laser, allowing them to remain whole.

After volatilisation of the nanoparticles, the sublimation laser acts as a particle guide. The gradient force of the laser keeps the desorbed particles in its center, while its radiation pressure pushes them upwards in the direction of an optical tweezer meant for particle detection (see section 3.2.4). For the proposed scheme nanoparticles and tweezer have to be chosen such that radiation pressure acting on the particles is greater than gradient force and gravity combined.

That the sublimation laser acts as a particle guide makes PPA melt-out especially attractive for vacuum environments. The particle guide allows for a much larger fraction of desorbed particles to reach the target area than they could via a desorption method with an undirected particle plume (e.g. LIAD). Additionally, a strongly focused sublimation beam allows us to melt out very small sections of the substrate, limiting the release of contaminants which could possibly enter the tweezer or pollute the optics in the chamber.

We investigated various kinds of samples, which we will split in two main categories (see section 4). The first category consists of glass coated with PPA, while the second utilizes a TEM-grid, which is filled with thin PPA layers. The metallic TEM grid allows for total sublimation of the carrier substrate in the region around the nanoparticle, but the observation of the particle distribution on the metal grid poses a problem. PPA-coated glass allows for an improved observation of the nanoparticle distribution, but make total sublimation of the carrier substrate impossible, effectively imposing an increased van-der Waal force on the particle depending on the thickness of the PPA coating.

For a sufficiently strong melt-out beam (or just a normal light source illuminating the sample from above) in combination with fluorescent nanoparticles, it is in theory possible to use fluorescence microscopy to map the particle positions on the PPA before melt-out, enabling volatilisation of single nanoparticles (see section 4).

3.2.3 Thermal sublimation of PPA

Since this volatilisation method hinges on sublimating of PPA using a highly focused laser, we should investigate the laser-PPA surface interaction. There are two main interaction types when considering a high-intensity laser irradiating a polymer surface. The photo-thermal model, which works similar to laser interaction with a metal surface described in section 3.1.4 and the photo-chemical model, which has the laser photons cleave the polymer chain, sometimes using a catalyst as an intermediary. A number of mathematical models describing both processes can be found in [123, 124].

Photo-chemical sublimation of PPA relies on laser-triggered photo acid generators (PAG's)

as an intermediary, which work as a catalyst to dissolve the acid-sensitive polymer-chains. This sublimation method has been investigated extensively for transient electronics [112, 119, 125]. Pure PPA without the involvement of PAG's on the other hand depolymerizes thermally. We work with pure PPA (see section 4), meaning we will discuss the photo-thermal regime.

The PPA-surfaces we have to sublimate in our setup are approximately $10\,\mu m$ thick. Using the lambert-beer law [84], as well as the linear absorption coefficient of PPA $\alpha = 4\pi n_I(\lambda)/\lambda$ calculated at $\lambda = 405\,nm$ with n_I and n_R taken from table 4, we can estimate the backside of the sample to still be irradiated with an evanescent field of $\approx 78\,\%$ of the intensity of the front side.

As such, we can make a quick estimate of the heating rate of PPA by assuming homogeneous heating of the substrate. We start our estimation of the heating rate by assuming a Laser of spot size w_0. with power P_0 hits the polymer. The laser-power at distance r from the optical axis at the waist can be calculated using [104]:

$$P(r,z) = P_0 \exp \frac{-2r^2}{w_0^2} \tag{86}$$

If we take $z = 0$ and $r = w_0$, we have $P = 0,14P_0$. Now that we know the power acting on the area with radius w_0 from the optical axis, we can calculate the total amount of power absorbed by this area. For this, we use the Lambert-beer law and integrate over the substrate thickness d:

$$P_{\text{abs}} = \int_0^d P_0 e^{-\alpha z} dz = \frac{P_0}{\alpha}\left[1 - e^{-\alpha d}\right] \tag{87}$$

We assume this power to act on all PPA molecules in the affected area of the substrate simultaneously. For an area of the substrate with radius w_0, we can calculate the number of molecules using the molar mass of PPA given in table 4:

$$N_{\text{sub}} = w_0^2 \pi d \rho_{\text{mol}} \tag{88}$$

Here $\rho_{\text{mol}} = \rho N_A/M$ is the molar density of PPA. Combining equations 88 and 87, we get the average power absorbed per molecule:

$$P_{\text{ind}} = \frac{P_{\text{abs}}}{N_{\text{sub}}} \tag{89}$$

Which we can use to calculate the heating rate:

$$\gamma = P_{\text{ind}} \frac{N_A}{M} / c_p \tag{90}$$

If we assume our desorption laser to have a $3\,\mu m$ waist and total power $P_0 = 0.05\,W$, then using this set of equations we estimate a heating rate of $\gamma \approx 125\,K/s$. This heating rate would cause the PPA to reach critical temperature in approximately $1.2\,s$. In this estimation we neither took into account heat loss due to e.g. black body radiation, thermal diffusion nor shielding of the substrate due to ablated PPA. As such, this estimation represents a lower limit of the melting time.

3.2.4 Behaviour of a nanoparticle after sublimation

The most promising aspect of PPA sublimation is the prospect of controlling the particles after volatilisation. To this effect, we simulate the potential behaviours of particles after sublimation. There are three kinds of forces acing on the particle. The gradient force of the sublimation beam that acts as a conservative force and keeps the particle in the focus of the desorption beam, radiation pressure and gravity gravity, acting against each other and pushing the particle out of

equilibrium, and the drag force acting as a damping factor.

If we assume a spherical nanoparticle, we can write the equation of motion as [126]:

$$m\ddot{\vec{x}}(t) + \Gamma_0 \dot{\vec{x}}(t) = \vec{F}_{\mathrm{ges}}(\vec{x}, t) \tag{91}$$

Here $F_{\mathrm{ges}}(t, \vec{x})$ represents the sum of all forces acting on the particle and Γ_0 is the damping factor due to the background gas:

$$\Gamma_0 = 6\pi\eta r_p \frac{0.619}{0.619 + Kn} (1 + c_K) \tag{92}$$

$$\vec{F}_{\mathrm{ges}}(\vec{x}, t) = \vec{F}_{\mathrm{grad}}(\vec{x}, t) + \vec{F}_{\mathrm{scat}}(\vec{x}, t) + \vec{F}_{\mathrm{g}} + \vec{F}_{\mathrm{abs}} \tag{93}$$

With $\vec{F}_{\mathrm{grad}}$, $\vec{F}_{\mathrm{abs}}$ as well as $\vec{F}_{\mathrm{scat}}$ as defined in section 2.2.2 and the gravitational force $\vec{F}_g = -m_p g \vec{e}_z$ acting on a particle with mass m_p. Equation 92 represents the stokes force acting on a spherical nanoparticles for a given background gas with pressure p_{env} and temperature T_{env}. Additionally, r_p is the nanoparticle radius, η the dynamic viscosity of the background gas, Kn the Knudsen number and $c_K = (0,31Kn)/(0,785 + 1,152Kn + Kn^2)$ a constant dependent on the Knudsen number. The Knudsen number can be expressed as:

$$Kn = \frac{L_{\mathrm{mfp}}}{r_p} \tag{94}$$

$$L_{\mathsf{mfp}} = \frac{k_b T_{\mathrm{env}}}{4\pi p_{\mathrm{env}} r_g^2} \tag{95}$$

With L_{mfp} as the mean free path of the nanoparticle and r_g the radius of the background gas particles.

Equation 91 takes into account the forces of the melt-out laser, gravity as well as the damping of the background gas. What is not accounted for in equation 91 is the Brownian motion of the nanoparticle due to its collisions with the background gas. In our calculations we assume an elastic collision with a nanoparticle of much bigger than the background gas particles ($m_p \approx 10\,\mathrm{GDa}$, whereas $m_g \approx 28\,\mathrm{Da}$ for nitrogen). This allows us to approximate the velocity change of the nanoparticle after collision with:

$$\Delta v = \frac{2\vec{p_g}}{m_p} \tag{96}$$

With $\vec{p_g}$ as the momentum of the gas molecule colliding with the nanoparticle. Equation 96 can be added to equation 91 as a random velocity change happening on the timescale of the mean free path of the nanoparticle $T_{\mathrm{mfp}} = L_{\mathrm{mfp}}/v_g$. Here v_g is the mean velocity of the background gas.

By solving the equations of motion numerically using the material constants in table 2, we can estimate the trajectory of a particle after sublimation. Two example trajectories for the nanoparticles most commonly used in our experiments are depicted in figure 15 and 16. The trajectories are similar in shape, with the Gold nanoparticles showing greater initial acceleration in the z direction and a higher equilibrium point due to their higher polarisability. The z position of the particle as a function of time behaves like an harmonic oscillator and reaches an equilibrium of scattering force and gravity after some oscillations. This has some interesting prospective applications for trapping particles. If we look at the particle position, we see that the Brownian motion of the background gas is not strong enough to counteract the radial gradient force. As long as the desorption laser is avtive, any desorbed particle inside it would effectively hover at the equilibrium position, being gradually cooled by the background gas. Trapping a particle cooled in such a way with a separate tweezer installed at the equilibrium position would theoretically

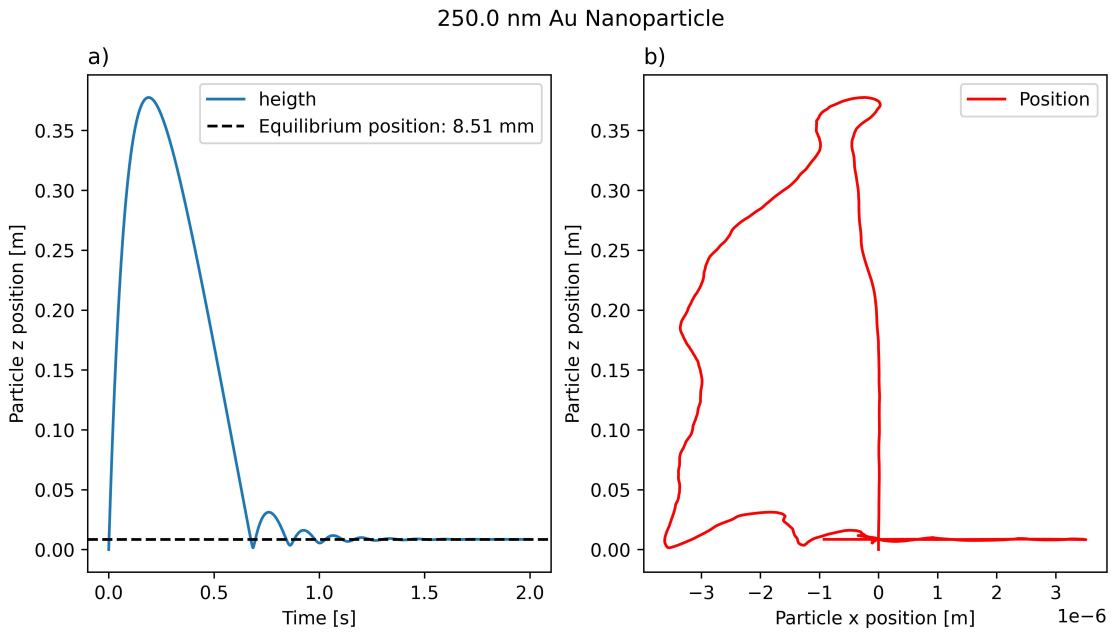

Figure 15: Simulation of the trajectory of a $250\,\text{nm}$ Au-nanoparticle after sublimation. We assume the desorption to occur at a pressure of $5\,\text{pa}$ with a desorption laser at $3\,\mu\text{m}$ waist and a with power of $50\,\text{mW}$. The initial position of the nanoparticle is taken as the 0 of the coordinate system.**a)** Z-position of the nanoparticle after melt-out as a function of time. We observe a strong initial upwards acceleration of the particle followed by a damped harmonic oscillation of the z-position gradually reaching an equilibrium position. **b)** Particle position after sublimation. The initial acceleration upwards is so strong that Brownian motion almost plays no role. The gradient force is strong enough to counteract Brownian motion.

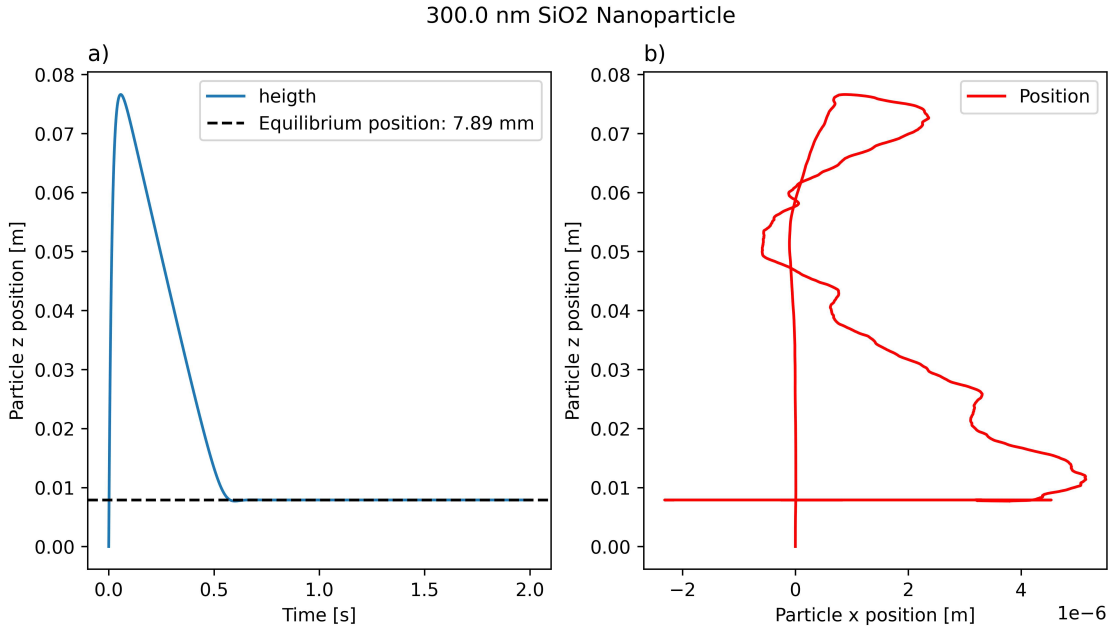

Figure 16: Simulation of the trajectory of a $300\,\text{nm}$ SiO_2-nanoparticle after sublimation. We assume the desorption to occur at a pressure of $5\,\text{pa}$ with a desorption laser at $3\,\mu\text{m}$ waist and with a power of $50\,\text{mW}$. The initial position of the nanoparticle is taken as the 0 of the coordinate system.**a)** Z-position of the nanoparticle after melt-out as a function of time. We observe a strong initial upwards acceleration of the particle followed by an over-damped harmonic oscillation of the z-position. **b)** Particle position after sublimation. The particle behaviour is almost analogous to figure 15

Particle:	250nm Au	300nm SiO2
Heating rate $[\frac{GK}{s}]$	35,32	0
T_{melt} [ns]	38	∞

Table 5: Heating rates and melting times of example nanoparticles without taking into account black body radiation or buffer gas cooling.

be possible at much lower pressures. This may allow for a reduction in environmental pressure necessary for optical trapping of nanoparticles.

Lastly, let us consider the temperature of nanoparticles in the melt-out beam. This can be easily achieved by looking at the Power absorbed by the nanoparticle:

$$P_{\mathrm{abs}} = I_0 \cdot \sigma_{\mathrm{abs}} \tag{97}$$

Where σ_{abs} is the absorption cross section which can be defined using equation 41:

$$\sigma_{\mathrm{abs}} = \frac{k\mathrm{Re}\{\alpha\}}{\epsilon_0} \tag{98}$$

From this, we can calculate the heating of the nanoparticle using the heat capacity c_m:

$$\gamma_{\mathrm{heat}} = \frac{P_{\mathrm{abs}}}{m_p c_m} \tag{99}$$

The material constants for Au, as well as SiO_2 are given in Table 2 and allow us to calculate the heating rates for both $300\,\mathrm{nm}$ SiO_2, as well as for $250\,\mathrm{nm}$ Au particles. The results can be see in table 5. When in the melt-out beam, the Au nanoparticles would melt in $2\,\mathrm{ns}$, making it unusable for this experiment. SiO_2 on the other hand doesn't absorb at $405\,\mathrm{nm}$, making it possible to irradiate it with the melt-out beam for longer times.

4 Experimental Setup

This section is split into three parts. In the first section, we describe our detection, as well as desorption setup for LIAD and PPA-sublimation. The second, as well as third section will describe the preparation of LIAD and PPA sublimation substrates and their respective particle distributions.

4.1 The desorption and detection setup

The detection setups for LIAD and PPA sublimation are nearly identical, with exception of the position of the nanoparticle source relative to the detection beam. In both cases, the nanoparticles are detected by collecting the scattered light of a focused $1550\,\mathrm{nm}$ tweezer-beam, as described in section 2.3. The difference in LIAD and PPA sublimation setups lies in the desorption setup.

4.1.1 Laser-induced acoustic desorption setup

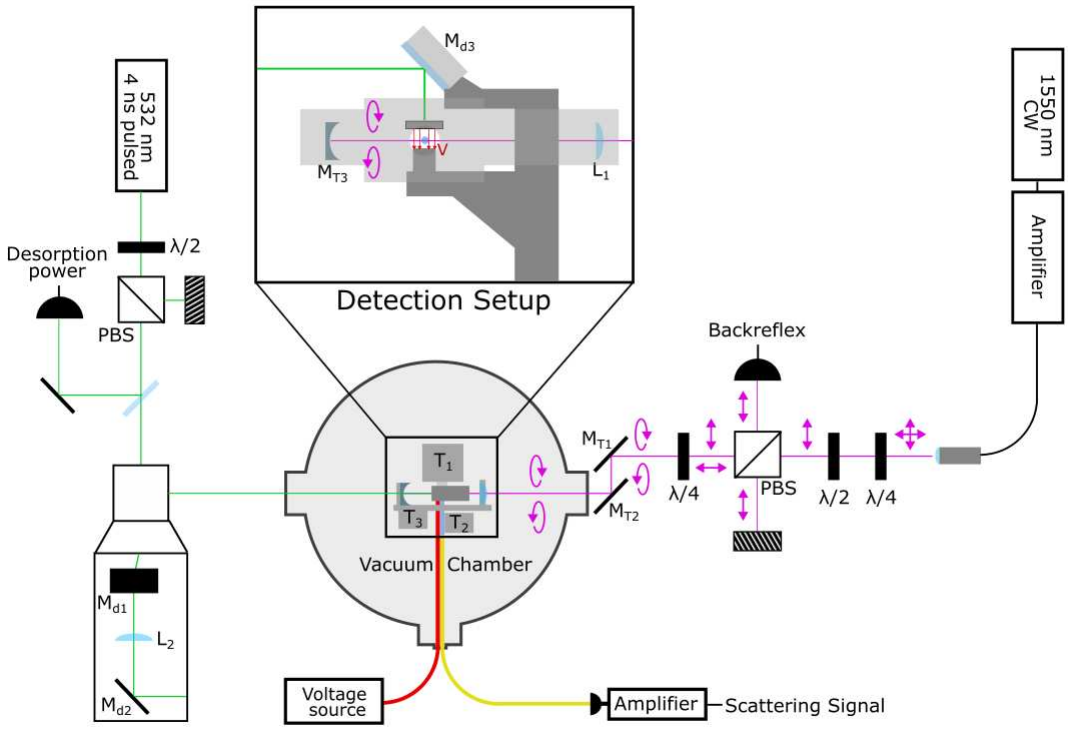

Figure 17: Schematic experimental setup for LIAD. The violet beam represents the $1550\,\mathrm{nm}$ laser used for particle detection. The mirrors M_{T1} and M_{T2} are used to align the incoming detection beam, while M_{T3} creates a standing wave in the detection region. L_1 is a lens with $f = 75\,\mathrm{mm}$ focusing the detection beam to $w_0 = 20.55\,\mu\mathrm{m}$. The scattered light is collected using a $500\,\mu\mathrm{m}$ diameter scattering fiber. The green beam represents the $4\,\mathrm{ns}$ pulsed $532\,\mathrm{nm}$ desorption laser, whose intensity is regulated using a $\lambda/2$-plate and a PBS. Its Alignment inside the vacuum chamber is adjusted with the dielectric mirrors M_{D1} and M_{D2}, while M_{D3} is used to adjust its impact angle on the substrate. The power of the desorption beam is monitored using a glass plate in combination with a photo-diode. The translation stages T_1, T_2 and T_3 are used to move the sample, the scattering fiber and the detection beam (tweezer) optics respectively. We set an electric field V between the sample substrate and a metal plate below the tweezer.

A schematic depiction of the LIAD-setup can be found in figure 17. The $1550\,\mathrm{nm}$ detection laser (Toptica photonics CTL 1550, output power $\approx 40\,\mathrm{mW}$) is amplified to $35\,\mathrm{dBm}$ by an optical amplifier (FTTP erbium doped fiber HA5400) and collimated using a fiber collimator (Thorlabs

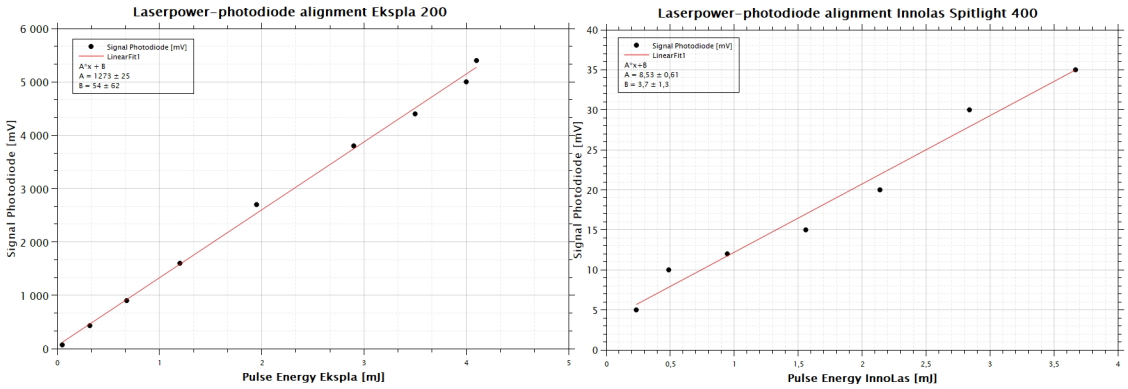

Figure 18: Photodiode signals as a function of the desorption laser pulse energy for both the Ekspla 200 and the Innolas SpitLight 400 respectively. The Intensity measurement has been taken between the anti-reflection coated glass plate and mirror M_{d1}.

Fiber Collimation Package F280FC-1550, beam diameter: $3.6\,\mathrm{mm}$).

The collimated beam passes through a $\lambda/4$, as well as a $\lambda/2$-plate after which it is be p-polarised. The beam subsequently passes through a polarising beam splitter that only lets p-polarised light pass towards the chamber, acting as a polarisation check. A $\lambda/4$-plate subsequently changes the p-polarised light to right circularly polarised light, which is later used to allow separation of the back-reflex from the incoming light. The mirrors M_{T1} and M_{T2} are dielectric broad band mirrors (Thorlabs BB1-E04) used for alignment. Inside the chamber, the detection beam is focused to a waist of $20.55\,\mu\mathrm{m}$ using lens L_1 ($f = 75\,\mathrm{mm}$) and reflected using a concave mirror M_{T3} with radius of curvature $19\,\mathrm{mm}$ (Thorlabs CM127-010-P01). Both L_1, as well as M_{T3} are placed on a translation stage which can be moved by a picomotor T_3 (Newport 8301NF). This picomotor allows displacement of the Tweezer. The right circular polarisation of the incoming beam changes orientation upon back-reflection on M_{T3}, transforming into left circularly polarized light. The incoming beam overlaps with the back-reflected one, creating a standing wave. The overlap of two circularly polarized beams of light of opposite handedness results in a standing intensity wave, as described in section 2.3 [127].

Nanoparticles crossing the standing wave will scatter light (see section 2.3), which in our setup is collected using a multi-mode fiber. A Thorlabs M53L02 fiber serves as our scattering fiber. It is connected to a Thorlabs SM05PD4A photodiode, whose Signal is amplified by an electrical amplifier (FEMTO DHPCA-100, magnification: 10^6) and fed to an oscilloscope (LeCroy wavesurfer 454). The scattering fiber can be moved using the three-dimensional translation stage T_2, which consists of three seperate translation stages (Newport MS-DS25-X-LC for y-translation and MS-DS40 for both x and z translations respectively).

During our LIAD measurements, we first worked with an Ekspla 200 nanosecond tunable laser system, which later got replaced with an Innolas SpitLight 400. In both cases we used the first harmonic of an ND:YAG laser ($532\,\mathrm{nm}$) at pulse lengths of $3.6\,\mathrm{ns}$ and $7\,\mathrm{ns}$ respectively with a waist diameter of roughly $4\,\mathrm{mm}$. The power of the Laser was modulated using a $\lambda/2$-plate together with a polarising beam splitter (Thorlabs CCM1-PBS251/M) and monitored using an anti-reflection coated glass plate in combination with a photodiode (Thorlabs PDA36A2) connected to the oscilloscope.

Using a photodiode to monitor the power of the desorption laser requires knowledge of the correlation between the diode signal and the energy per laser pulse. For this purpose a power meter (Coherent Field mate PM10) was placed between the anti-reflection coated glass plate used to divert part of the beam to the photodiode and mirror M_{d1}. A series of measurements of

the diode signals for different laser powers both for the Ekspla 200 laser, as well as the Innolas can be seen in figure 18. The data is fitted to function $A \cdot x + B$, where A is the conversion factor between diode Signal and laser power. For the Ekspla Laser, A is $(12.73 \pm 0.25)\,\mathrm{V/J}$, while for the Innolas it is $(8.53 \pm 0.61)\,\mathrm{V/J}$. This conversion factor allows us to use the photodiode current to calculate the laser power.

The mirrors M_{D1} and M_{D2} (Thorlabs BB1-E02) are placed on top of each other in a periscope setup. They are used for the alignment of the desorption beam to the center of mirror M_{D3}, while mirror M_{D3} is used to control the impact angle of the desorption beam on the substrate. Between Mirrors M_{D1} and M_{D2} the lens L_2 ($f = 500\,\mathrm{mm}$) is positioned, focusing the desorption beam to $w_0 \approx 50\,\mu\mathrm{m}$ on the substrate. After the initial alignment, the laser stays in position, while the sample is moved using translation stage T_1 (SmarAct DLS5252).

We are interested in the behaviour of nanoparticles desorbed with LIAD when applying an electric field to the area of their propagation. As such, we connect the substrate, as well as a metal plate beneath the substrate (see figure 17) to the poles of a voltage source (RS-3005D, 0-30V 0-5A). The poles are interchangeable at their interface to the vacuum chamber, allowing us to set an electric potential and control its direction between tweezer and substrate.

4.1.2 (Poly-)Phtalaldehyde sublimation setup

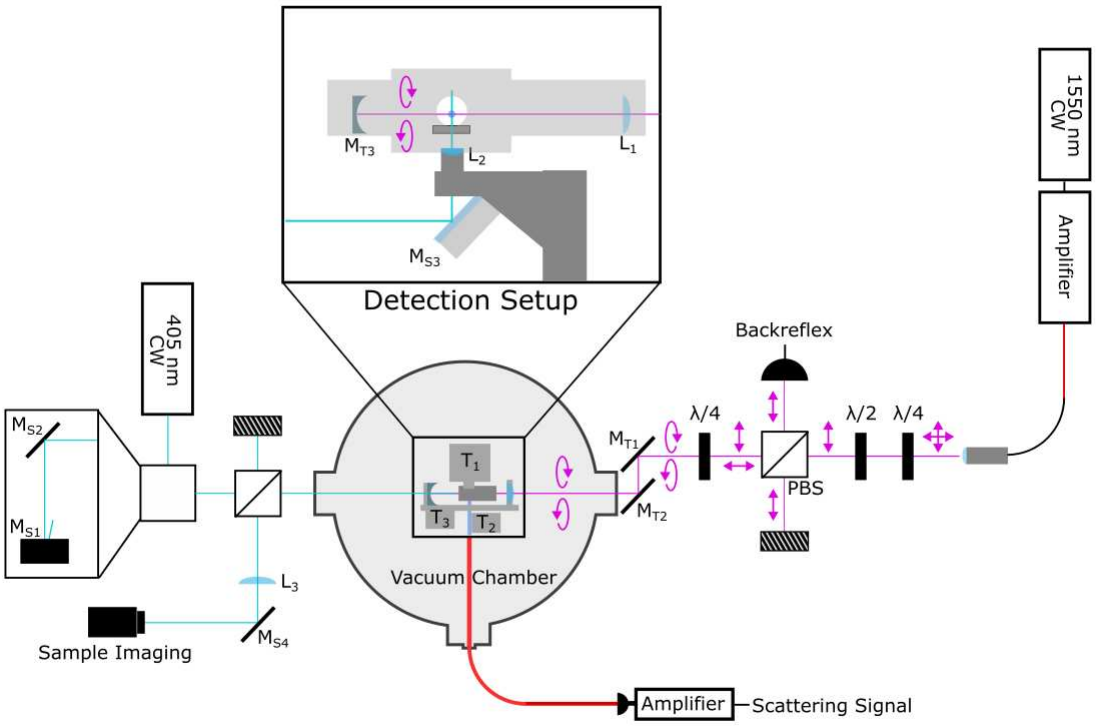

Figure 19: Schematic experimental setup for PPA sublimation. The detection setup is identical to LIAD (see figure 17). The cyan beam represents the $405\,\mathrm{nm}$ desorption laser. The beam alignment inside the vacuum chamber can be adjusted using the dielectric mirrors M_{S1} and M_{S2}. Unlike the LIAD-setup, M_{D3} is fixed and cannot be used to adjust its impact angle on the substrate. The reflection of the laser on the sample is collected by the focusing Lens L_2 and used for imaging. The translation stages T_1, T_2 and T_3 are used to move the sample, the scattering fiber and the detection beam (tweezer) optics respectively.

The experimental setup of our PPA-sublimation experiments is schematically depicted in figure 19. The $1550\,\mathrm{nm}$-detection beam setup is identical to the one used for LIAD, while a different des-

orption laser is used to sublimate the PPA (Toptica iBeam-SMART-405-S-HP, center wavelength $405\,\text{nm}$, beam diameter approximately $1\,\text{mm}$). The sublimation beam is aligned using mirrors M_{S1} and M_{S2} of the periscope. After the periscope, a non-polarising beams splitter is inserted into the beam path, which was used for subsequent imaging of the sample. This beam splitter effectively halves the intensity of the sublimation laser, but has no other effect on the on the incoming beam.

Using the mirrors M_{S1} and M_{S2}, we align the beam to be reflected in a right angle of mirror M_{S3} to the center of Lens L_2 (Edmundoptics molded aspheric lens $EFL = 14\,\text{mm}$), which focuses the beam to $\approx 3\,\mu\text{m}$. As described in section 3.2.4, the PPA-substrate is placed below the detection beam, with the sublimation beam acting as a particle guide. To ensure the substrate is placed in the focus of lens L_2, and to have better control over which region of the sample is irradiated by the desorption laser (see section 4.3), we constructed an imaging system using the reflection of the sublimation beam on the substrate.

The imaging system works analogous to a light microscope using two lenses (see figure 8). The light scattered by the substrate is collected by Lens L_2 and back-reflected along the path of the incoming beam until it reaches the beam splitter. At the beam splitter, half the scattered light is reflected and subsequently focused using Lens L_3 (Thorlabs LA1172-C, $f = 400\,\text{mm}$) onto a camera (Teledyne Grasshopper3). Mirror M_{S4} is used to focus the back-reflex on the camera.

Alignment of the detection and sublimation beam

It is crucial to have the $1550\,\text{nm}$ tweezer aligned to the detection beam to ensure overlap of the particle guide and the detection system. To ensure this, we move the scattering fiber using translation stage T_2 towards the center of the sublimation beam to maximise the sublimation light beam collected in the scattering fiber. During this process the detection beam is turned off. Then, we switch off the sublimation laser and activate the detection beam. Subsequently, we move the tweezer using translation stage T_3 to maximise the light of the detection beam collected in the scattering fiber. Using this process, we are able to align the beams to a precision of $10\,\mu\text{m}$, limited by the precision of translation stage T_2. Considering the detection beam diameter ($20.55\,\mu\text{m}$), the given precision should be sufficient to ensure overlap of the beams.

4.2 Laser-induced acoustic desorption sample preparation and positioning

To characterize a source, we need to minimize the number of variables influencing the properties of the desorbed particles. Here, we treat the variables arising from the substrate preparation and positioning and our attempts at minimising them. We will discuss the shape of our sample holder and the mechanism clamping it to translation stage T_1, the method of sample preparation and the method we used to position our sample before and during the desorption process.

4.2.1 Shape of the sample holder and clamping mechanism

A schematic of the substrate foil and its holder is depicted in figure 20 **a)** and **b)**. The substrate foil is glued to a (8×12) mm plate of Aluminium with a thickness of $500\,\mu\text{m}$, which we call sample holder. A square hole of $5.5\,\text{mm}$ edge length allows the desorption laser to access the substrate. The side of the substrate irradiated by the desoprtion laser will from now on be called back-side, while the opposite side of the substrate will be called front-side. The sample holder is only used for metallic substrates, while the silicon wafer substrates are directly clamped onto T_1.

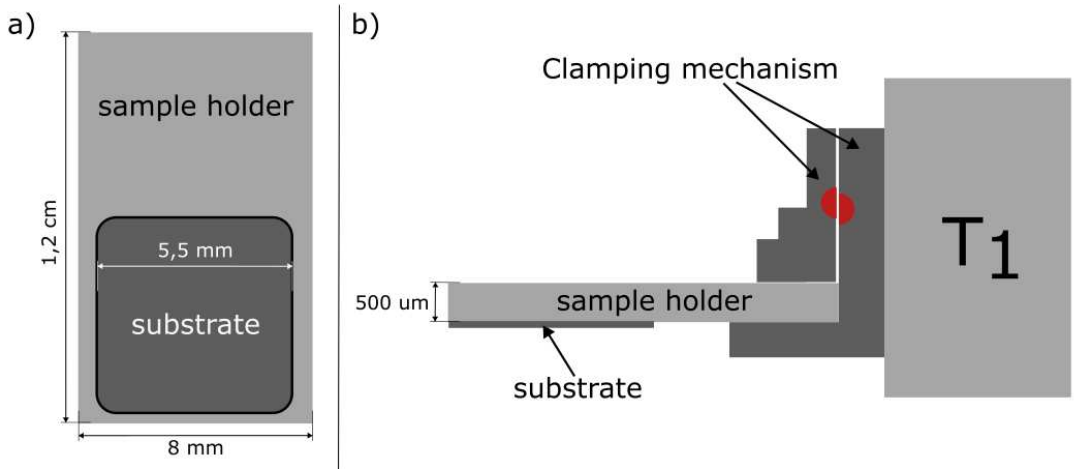

Figure 20: **a)** Schematic depiction of the sample holder **b)** Clamping mechanism fixing the sample holder to Translation stage T_1

In figure 20 **b)**, the clamping mechanism fixing the sample holder to translation stage T_1 is depicted. It consists of two L-shaped pieces of metal, one of which is screwed on the Translation stage, the other is free. Permanent magnets are embedded in both parts of the clamping mechanism (20 **b)**, demarcated red), whose attraction towards each other, clamp the sample holder onto the translation stage.

4.2.2 Method of sample preparation

The properties of the LIAD plume are dependent on the distribution of the analyte on the substrate. More specifically, high analyte concentrations lead to the formation of multiple stacked layers of analyte particles, which causes the formation of analyte clusters. This effectively reduces the single-particle yield in favor for a higher fraction of clusters. Similarly, low analyte concentrations reduce the single-particle yield since there are less particles on the substrate for the desorption laser to desorb.

When preparing a sample, we are looking for a single, evenly spread, layer of nanoparticles on the substrate, with enough space between particles to avoid cluster formation. We diluted the pre-fabricated nanoparticle solution (microspheres-nanospheres C-SIO-G0.3; $300\,\mathrm{nm}$ Green Fluorescent Silica nanospheres, SiO_2-Concentration: $25\,\mathrm{mg/ml}$) with distilled water in a 10:1 ratio. The diluted solution was ultrasonified for 30 minutes to ensure homogeneous particle distribution before being applied to the substrate via spin-coating. During spin-coating, the substrate spins with a rotational frequency of 10 rotations per second (rps) and $60\,\mu\mathrm{l}$ of solution is applied to the center of the substrate. Subsequently, the rotational frequency of the substrate is slowly increased to 50 rps over the next minute, which causes the droplet of solution in the substrate center to spread evenly across the surface.

The results of spin coating can be seen in figure 21. The analyte particles form a submonolayer on the majority of the substrate surface with patches of higher nanoparticle density appearing at random intervals. The patches in question consist of a particle monolayer of higher density, though we can observe some particle clusters concentrated on their edges. The formation of patches occurs mostly in the center of the substrate, while its edges show a lower density of both particles and patches of high particle density. The formation of patches can be attributed to splashing of the analyte solution during the spin-coating. Spraying the analyte solution on the sample via nebulisation could pose a solution to this.

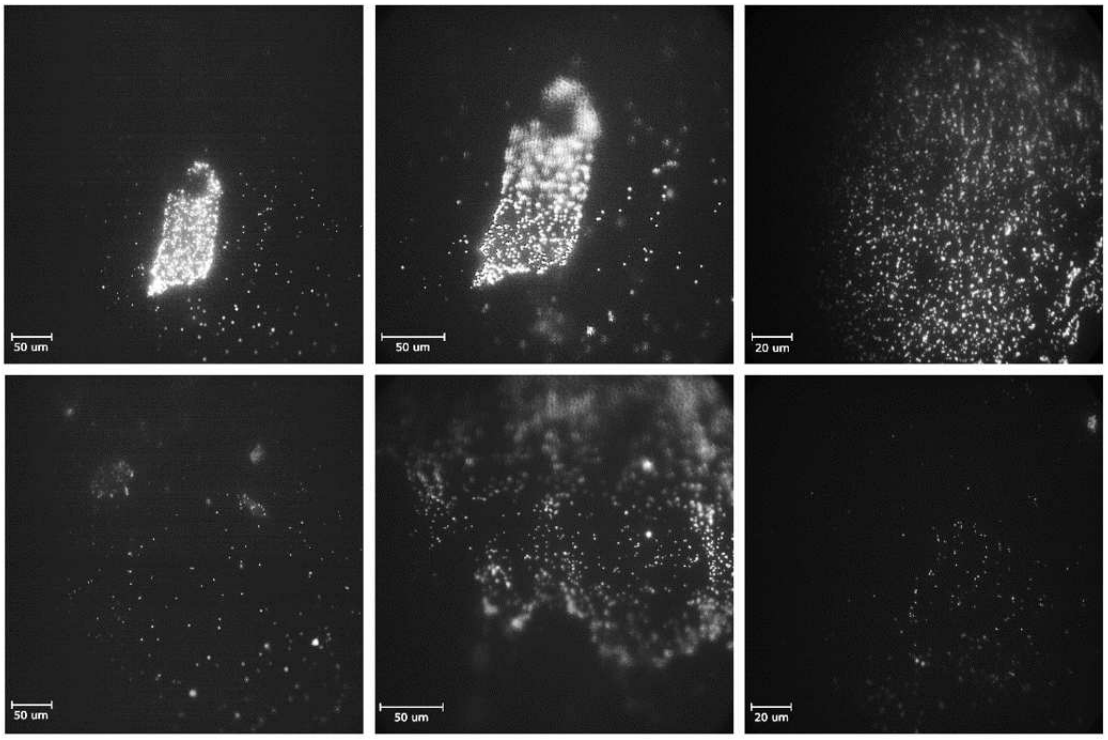

Figure 21: A selection of fluorescence microscopy images of $300\,\mathrm{nm}$ fluorescent Silica particles spin-coated on a $500\,\mu\mathrm{m}$ copper substrate with a magnification of $40x$ (left), $63x$ (middle) and $100x$ (right)

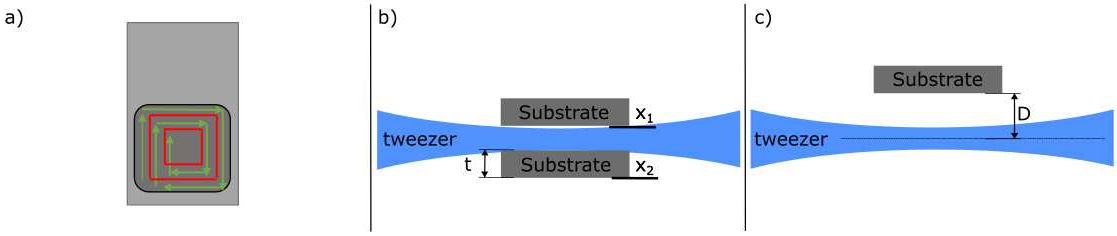

Figure 22: Scheme of our method of sample positioning and shootout. In **a)**, we define the movement pattern of the sample with respect to the desorption laser during shootout. In **b)**, we define our definitions of the sample positions x_1 and x_2, which will be used in conjunction with the sample thickness t to determine the center point of the tweezer and in **c)**, we depict the distance D between the front-surface of the substrate and the center of the tweezer, which we define as the distance between sample and tweezer.

4.2.3 Sample positioning scheme

We define the way we move the sample during the desorption process to prevent overlap between the impact points of the desorption laser and allow for a study of the dependence of source properties on the foil position during the LIAD process. Additionally, we define a method to determine the distance between substrate front-side and detection beam taking into account sample thickness.

The sample and its movement scheme during LIAD are depicted in figure 22 **a)**. We start desorbing particles in one of the outer corners of the substrate and move inwards in a spiral. This allows us to keep track of the position of the desorption laser on the foil and avoid repetitive desorption of particles from the same spot.

In figure 22 **b)** and **c)**, the scheme used to determine the distance between the sample and the center of the detection beam is depicted. We assume the x-position of the sample to corresponds

to the x-position of its front-side, since we are interested in the distance particles travel after desorption. We assume movement of the sample with respect to the tweezer only in one axis (the axis normal to both the sample and the detection beam), which we will refer to as the x-axis. The x-position of the sample is measured using a program keeping track of the position of Translation stage T_1. We start with the sample above the tweezer and slowly move the sample downwards until we cut into the detection beam. When starting to cut into the detection beam, we observe a drop in the back-reflected intensity (see figure 17). We define the x-position of the sample with the minimal observable drop in back-reflex x_1. Here the sample touches the upper edge of the tweezer. Moving the sample downward, it eventually leaves the tweezer. Before leaving the tweezer fully, it reaches an x-position equivalent to x_1, where its upper edge touches the lower edge of the tweezer. We call this x-position x_2. Using positions x_1 and x_2, as well as the sample thickness t, we can calculate the beam center x-position:

$$x_{\text{center}} = x_1 - \frac{x_1 - x_2 - t}{2} = \frac{x_1 + x_2 + t}{2} \tag{100}$$

Using equation 100, we can easily arrive at a term describing the sample position for arbitrary distances D between sample and center of the detection beam:

$$x_{\text{substrate}} = x_1 - \frac{x_1 - x_2 - t}{2} = \frac{x_1 + x_2 + t}{2} + D \tag{101}$$

4.3 (Poly-)Phtalaldehyde sublimation sample preparation

Similar to the LIAD-samples, the particle concentration of the substrate is of paramount importance for the quality of the source. Since our goal for PPA sublimation is to melt out single particles with minimal pollution (see section 3.2), we want the nanoparticles to be sparsely distributed. For this, we have chosen a dilution of the prefabricated nanoparticle solution with distilled water or isopropanol in a ratio of $1 \times 10^6 : 1$. The resulting particle distribution can be observed in figure 23. We used a syringe to drip $20\,\mu$l of the diluted NP-solutions on a microscopy slide and observed said solutions under a fluorescence microscope. We observe a sub-monolayer particle distribution dominated by single particles, as well as some half transparent white stains on the microscopy image, which we interpret as dirt on the other side of the microscopy slide.

We observe a similar rate of particle clusters for the water-diluted and isopropanol-diluted solution, though the isopropanol-diluted solution has a lower concentration of particles than the water-diluted one. This is most likely due to the faster evaporation of isopropanol than water, which causes of some solution in the syringe to evaporate, reducing the effective amount of solution applied to the microscopy slide. As such, we conclude that the particle distribution of solutions diluted with water or isopropanol is not significantly different.

A significant difference between water- and isopropanol diluted solutions lies in their behaviour when aerosolised. The solution of nanoparticles dissolved in water produce comparatively more aerosol particles, but have a tendency to condense into droplets that produce patches of high particle density similar to section 4.2.2. The isopropanol on the other hand dries to fast to be able to condense into droplets, but has a noticeably lower aerosol yield when nebulised, necessitating longer nebulisation times.

When discussing the PPA samples, we distinguish between two kinds of samples. Glass coated with a thin layer of PPA, where analyte solution is nebulised onto the PPA layer afterwards and Transmission electron microscopy (TEM) grids filled with PPA. Here the analyte particles are either nebulized onto the PPA, or applied onto the grids together with the PPA.

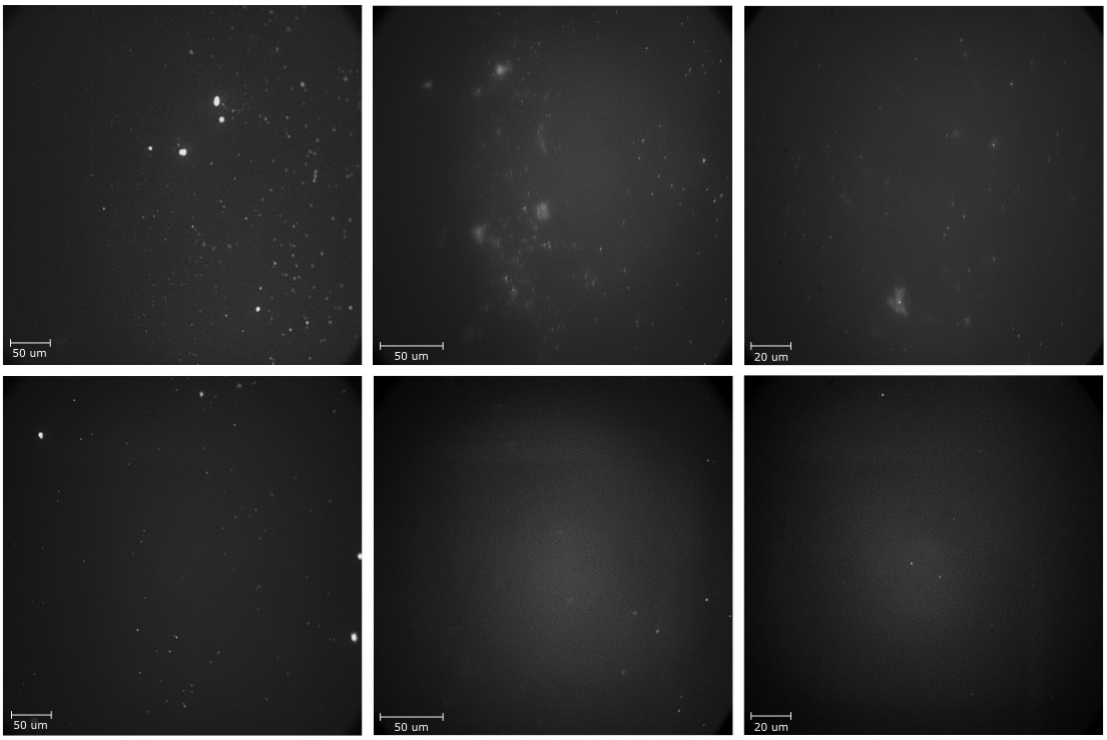

Figure 23: A selection of fluorescence microscopy images of $300\,\text{nm}$ fluorescent Silica particles applied on a microscopy slide. We applied $20\,\mu\text{l}$ of NP-solution on the microscopy slide by dripping the solution on the slide using a syringe. The original NP-solution was diluted in a ratio of $1 \times 10^6 : 1$ using distilled water (upper row) and isopropanol (lower row).

Material	Mesh	Mesh shape	Manufacturer
Nickel	200	Square	Tedpella Pelco
Nickel	400	Square	Tedpella Pelco
Copper	500	Square	Tedpella Pelco
Gold	200	Hexagonal	Tedpella Pelco
Gold	400	Square + $2\,\mu\text{m}$ Submesh	PLANO

Table 6: Selection of TEM-grids used for sample preparation. All TEM grids used have the standard diameter of $3.05\,\text{mm}$

4.3.1 Transmission electron microscopy grids as sample holders for (Poly-)Phtalaldehyde sublimation

We prepared TEM grids made from a number of different materials of several different grid shapes and sizes to prepare PPA samples. The grids in question are placed on a thin metal plate acting as the sample holder with the same dimensions as the sample holder used in LIAD, but a different hole, capable of holding the TEM grids (see figure 24). A full list of the TEM grids can be found in table 6. The grids are filled with PPA solved in a 20:1 mass ratio with Tetrahydrofuran (THF). The solution is applied either by dripping $20\,\mu\text{l}$ it onto the TEM-grid or by dipping the TEM-grid in the solution. Nanoparticles are similarly applied onto the grid by one of two methods. Either the nanoparticle and PPA solution are mixed before application to the TEM-grid, or they are applied the the dried PPA surface via nebulization. In either case the TEM grid is placed on the sample holder before the PPA solution can dry, allowing it double act as a glue and affixing the grid on its holder.

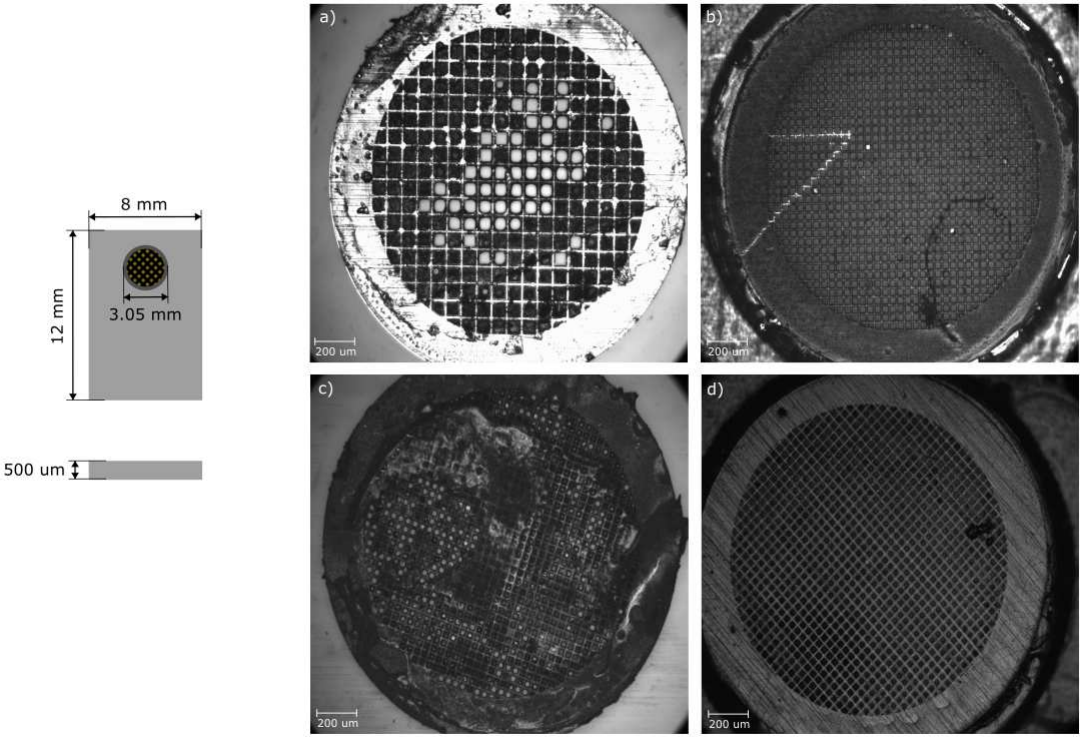

Figure 24: Schematic depiction of the sample holder together with four nickel TEM grids prepared using different methods. **a)** When dripping $20\,\mu l$ of PPA solution on a 200 mesh nickel grid, most central grids are empty and we can observe holes in the PPA layer over the entire grid. **b)** A 400 mesh nickel grid prepared similarly shows a homogeneous layer of PPA with few holes in the PPA layer. The dark and white lines on the sample were caused by a hair and a scratch from a tweezer respectively. **c)** The 400 mesh nickel grid dipped in$20\,\mu l$ PPA solution shows an inhomogeneous distribution of PPA, with some parts of the grid being covered with PPA, while others are empty. **d)** Dripping the PPA-solution twice on the same 400 mesh nickel grid allows for smooth PPA layers.

Microscopy images of some of the prepared TEM grids can be found in figures 24 and 25 . We found the distribution of the PPA strongly dependent on both the sample, as well as the method of application. Dipping the grid in the PPA-solution causes the formation of droplets of PPA on the grid, resulting in an uneven PPA-distribution. Dripping the solution on the sample leads to a more homogeneous PPA distribution, but demands the presence of the sample holder keeping some space below the grid during the drying process and let excess solution drip off the sample. Furthermore, dripping the solution on the grid tends to leave holes in the center of the grid. By dripping the PPA-solution on the grid twice, we can create a flat layer of PPA with a thickness of $\approx 10\,\mu m$ across the whole grid.

Naturally, the quality of the PPA-layer depends not only on the application method of the solution, but also on the TEM grid. Of the samples used, the nickel grid with 400 mesh was the most suited for sample preparation. The grid size of the 200 mesh Nickel grid was found to be too large to form a coherent PPA layer, leaving holes in most of the grids. The gold grids ware too fragile, breaking during the application of the solution or during their placement in the sample holder. The subgrid-membrane of the 400 mesh gold grid especially was prone to breaking and judged to be detrimental to the observation of the PPA layer. The issue we faced with the copper sample was the presence of a handle fixed on the sample. This handle made it impossible for the grid to properly fit on the metal plate acting as the sample holder, necessitating the sample to be fixed on the sample holder at an angle. Additionally, we observed substructures in the PPA layer. A square shape of a thinner PPA layer in the center of the holes in the lattice surrounded by a ring structure of thicker PPA at the lattice edges of the holes was observed. These sub-

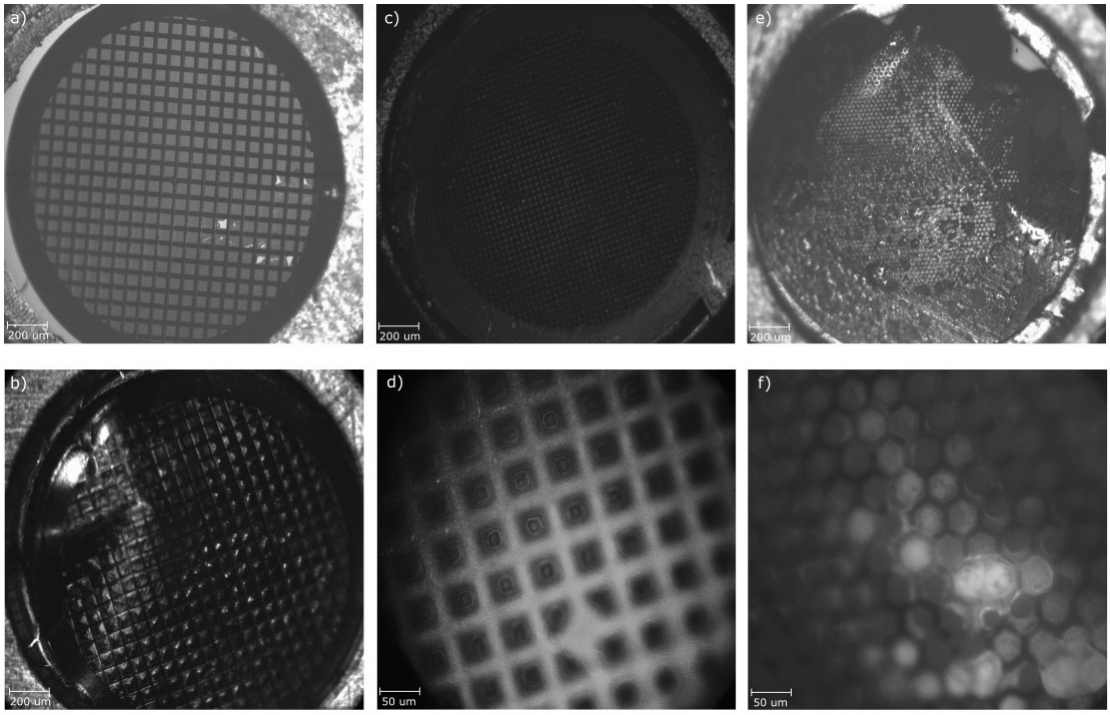

Figure 25: Selection of microscopy images of TEM grids. **a)** 200 mesh Gold grid with $2\,\mu m$ subgrid without PPA ($10\times$ magnification). The subgrid lattice is made of a gold foil with $2\,\mu m$ thickness, making it very fragile. Simply picking up the grid and placing it under the microscope has already damaged the subgrid. **b)** 200 mesh Gold grid with $2\,\mu m$ subgrid. PPA is applied via dripping the solution on the grid ($10\times$ magnification). The grid is deformed at the spot it was gripped with the tweezers. **c)** 500 mesh copper grid, PPA is applied via dunking the grid in solution ($10\times$ magnification). The handle of the grid can be seen in the right lower edge of the image. The distribution of PPA is fairly regular . **d)** Closeup of the same 500 mesh copper grid ($40\times$ magnification). We observe a substructure in the PPA, forming square shapes of either holes or thinner PPA layers in the center of the grid. **e)** 500 mesh hexagonal Gold grid, PPA is applied via dunking the grid in solution ($10\times$ magnification). This grid far to fragile to apply our solution to it, showing even stronger bending during the process than the 200 mesh Gold grid, which can be attributed to its smaller lattice. **f)** 500 mesh hexagonal Gold grid, PPA is applied via dunking the grid in solution ($40\times$ magnification). We observe an inhomogeneous distribution of PPA, similiar to a NI-grid dunked in PPA.

structures are most likely consequences of the surface tension of the PPA solution, with copper likely having a higher surface tension for the PPA-solution as compared to nickel. Interestingly, copper grids have shown to produce more homogeneous PPA layers when dunking them in PPA than nickel grids. Dripping PPA on them has not been attempted, since their uneven resting position on the sample holder would most likely result in an uneven distribution of the PPA solution.

Working with TEM grids filled with PPA has the advantage of being able to fully sublimate the substrate when desorbing the particles, but comes with a set of disadvantages. Our main issue with PPA filled TEM grids was our inability to observe single nanoparticles embedded in the PPA solution under the fluorescence microscope. It is possible to observe fluorescence of the PPA layer when dotted with nanoparticles, but we couldn't observe single nanoparticles embedded in said layer. We attribute our inability to see nanoparticles to the opaqueness of the PPA, since it was independent of the substrate the PPA was applied to (see figure 26). We were able to counteract this to some extent by separating the PPA-solution from the nanoparticles and applying said nanoparticles afterwards via nebulization (see figure 26). An additional issue is posed by the sample holder. The TEM-grid is embedded in the sample holder, which blocks our objective lenses with $100\times$ and $63\times$ magnification, allowing for a maximum magnification of only $40\times$. We were unable to improve upon this, since the sample holder is needed for the preparation of

the TEM grid and when removing the grid from its holder after preparation, the PPA-solution acts as glue and prevents us from removing the grid without damaging it in the process.

TEM microscopy images of a 400 mesh Ni-grid are depicted in figure 35. The PPA solution is dripped onto the TEM grid twice, after which nanoparticles are nebulised onto the dried PPA layer. TEM microscopy allows us to not only investigate the smoothness of the surface of the PPA-layer, but also enables us to observe the distribution of nanoparticles on the PPA. The center of the PPA-surface is smooth, while any cracks are concentrated at its edges. We see some deformations in the PPA surface near the nanoparticles, which lets us to assume that the isopropanol-solution that has been used for their nebulisation is able to locally dissolve the PPA. The nanoparticles are evenly distributed over the center of the grid, while they agglomerate at its edges and near the cracks in the PPA. They are deposited on the PPA layer either alone or in small clusters of 2 to ≈ 20 particles.

4.3.2 Glass coated with (Poly-)Phtalaldehyde

The coated glass samples were prepared due to the sample holder necessary for coating TEM grids with PPA blocking the $63\times$ and $100\times$ magnifications of our fluorescence microscope. The goal was to observe the nanoparticle distribution on the sample up close, while still making use of a layer of PPA to increase the distance between nanoparticles and glass surface. The van der Waals forces binding the nanoparticles to the surface scale inversely with distance (see section 3.2), and as such a sufficiently thick PPA layer reduces the attractive force between glass surface and nanoparticles enough to allow for desorption.

To prepare the sample, we dripped $20\,\mu l$ of PPA solved in THF in a 20:1 ratio using a syringe on a microscopy slide. Then we covered the solution with yet another microscopy slide, before pulling the slides apart, therefore creating a thin layer of PPA on their surfaces. After applying PPA, we coat the surface with nanoparticles by spraying aerosolized NP-solution in a ratio of $1 \times 10^6 : 1$) on the surface.

The resulting sample can be observed with much higher magnifications under the fluorescence microscope. Some fluorescence microscopy images of the sample are depicted in figure 28. The sample in question has been nebulised using the NP-solution diluted with distilled water, which condensed into droplets during the drying process. This results in an observable inhomogeneity in the particle distribution and forms patches in places where the droplets condensed. Upon observation of the particle patches, we see a mostly homogeneous particle distribution with no observable clusters. In addition to the particle distribution, we observe dark spots with bright lining. We found these spots to be dried PPA solution, which formed droplets during its application process. The inhomogeneity of the PPA-layer make this kind of sample unusable as a substrate for PPA sublimation.

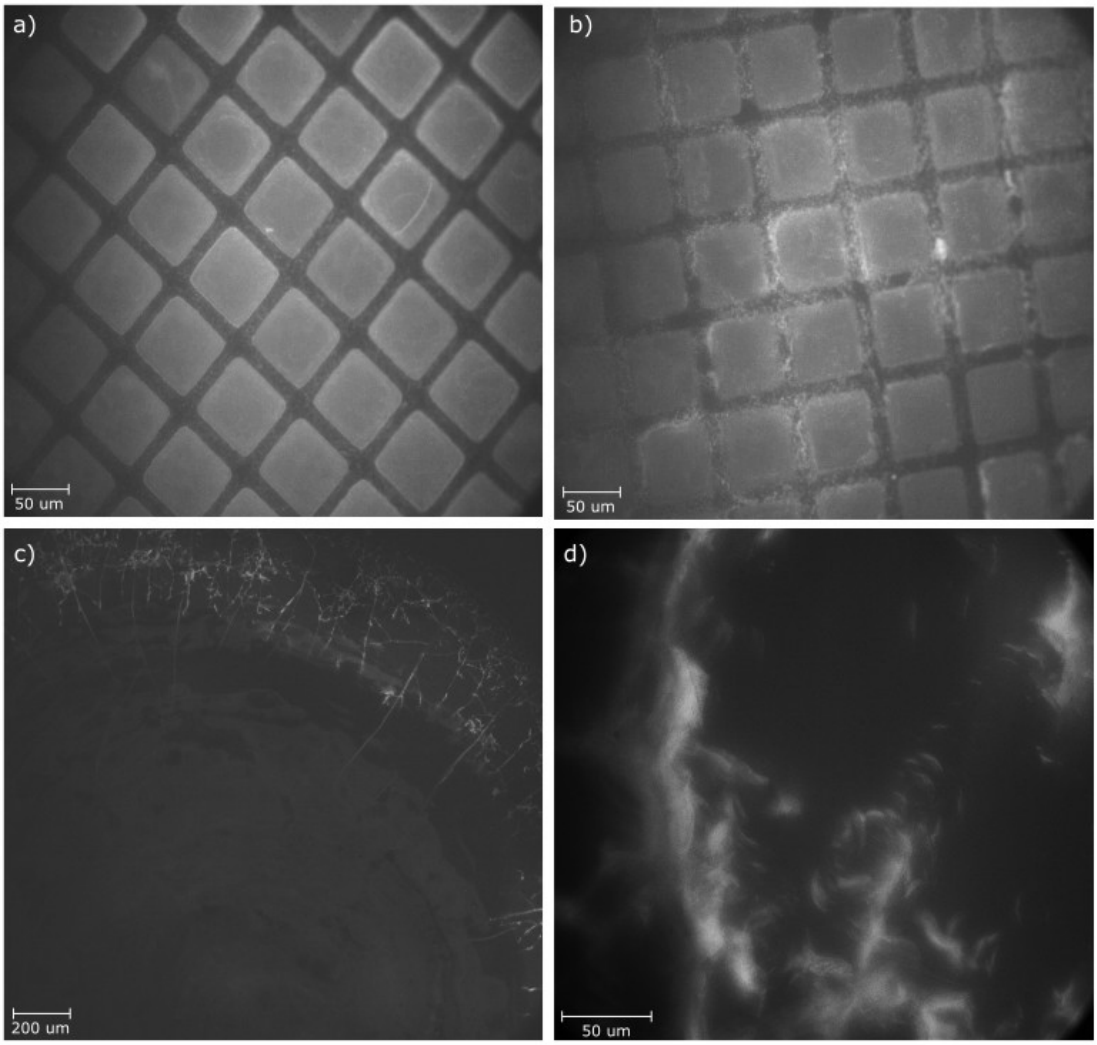

Figure 26: Fluorescence microscopy images of nanoparticles on PPA. **a)** 400 mesh nickel grid filled with PPA-solution ($20\,\mu l$ dripped twice on the grid) containing nanoparticles depicted using fluorescence microscopy with $40\times$ magnification. We can see the fluorescence of the nanoparticles illuminate the holes of the lattice and it is possible to make out some particles on the lattice itself, but we cannot see single particles in the holes of the lattice. **b)** 400 mesh nickel grid filled with PPA-solution ($20\,\mu l$ dripped twice on the grid) and afterwards nebulized with nanoparticle solution $40\times$ magnification. We are able to make out single nanoparticles both on the lattice as well as in its holes. The sample in question has a very high particle density due to a long nebulization time. **c)** $20\,\mu l$ PPA-solution dripped on a microscopy slide, $10\times$ magnification. We see a uniform glow in the center of the PPA-drop with cracks caused by the drying process on its edges. **d)** $20\,\mu l$ PPA-solution dripped on a microscopy slide, $63\times$ magnification. Even with greater magnification, we still cannot see any particles in the PPA. We observe glowing cracks in the PPA. The cracks can be attributed to the drying process of a large, coherent PPA-surface, as in c). We assume the reason for them to glow is either the accumulation of nanoparticles in the during the drying process or the sedimentation of nanoparticles at the bottom of the PPA. If the latter where the case, the cracks would act as tunnels to the fluorescent nanoparticle sediment.

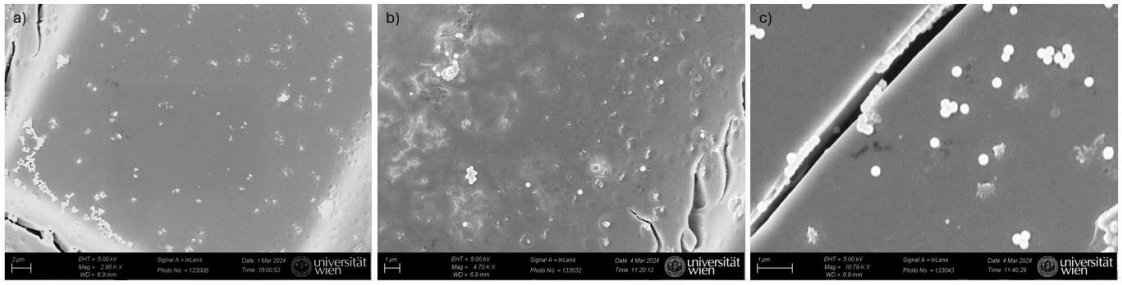

Figure 27: Transmission electron microscopy images of nanoparticles nebulised on a PPA-filled TEM grid. The PPA forms a flat surface with some cracks at its edge. The nanoparticles are distributed evenly over the PPA-layer, either as single particles or conglomerating in small clusters at the edges of the PPA or in the cracks.

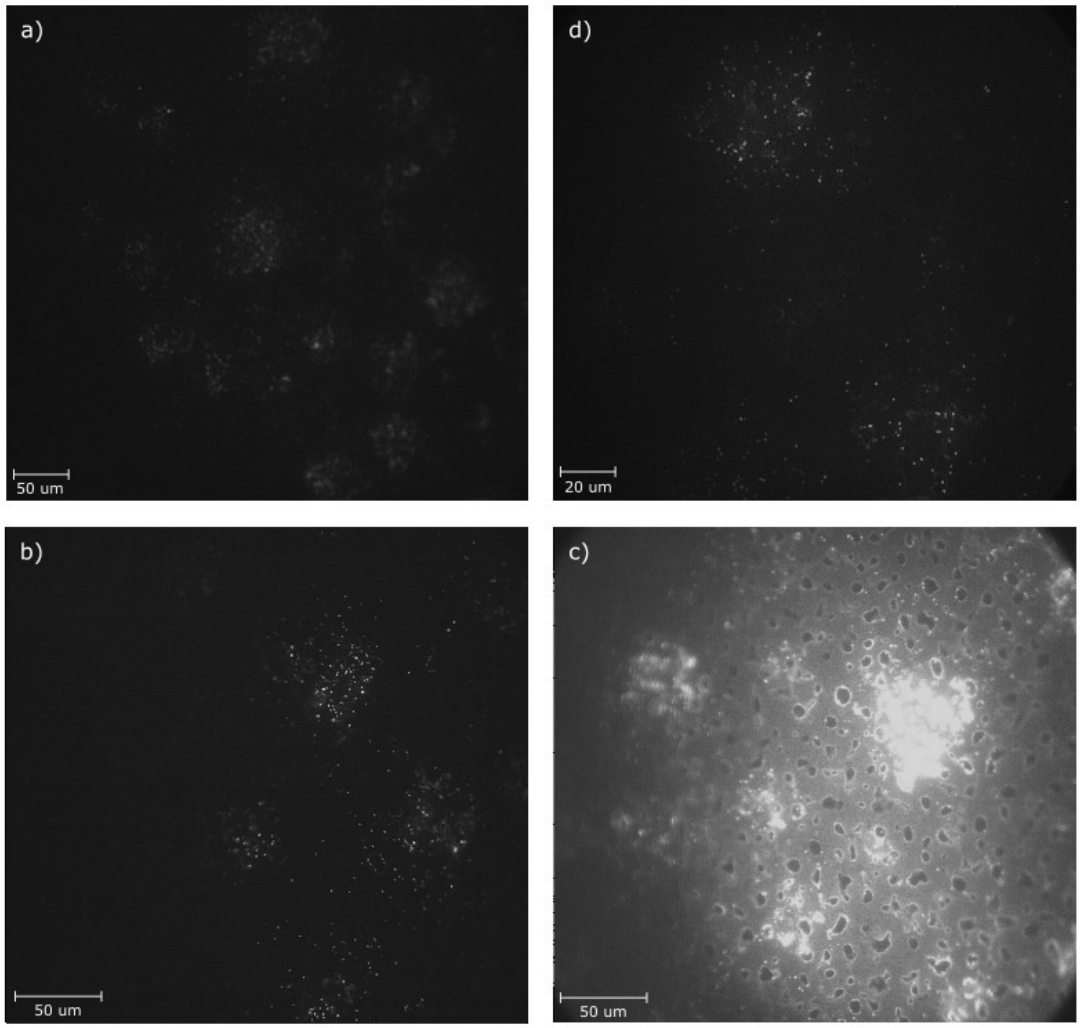

Figure 28: fluorescence microscopy images of a microscopy slide coated with PPA and nebulized using nanoparticle solution diluted with water. **a)** $40\times$ magnification. The particles form patches on the glass plate. These patches are caused by the condensation of the solution into droples during the nebulisation process. **b)** $63\times$ magnification. We observe homogeneously distributed particles along with some bright spots in the background of the picture not caused by particles. **c)** $63\times$ magnification with increased illumination. We can see the uneven distribution of the PPA solution, forming droplets instead of a homogeneous layer. **d)** $100\times$ magnification. A closer observation of the particle distribution reveals that most particles are placed directly on the glass instead of on PPA.

	300 nm SiO_2	150 nm SiO_2	100 nm SiO_2
5 µm Ti	3	-	-
50 µm Ti		1	1
50 µm Cu	2		
500 µm Cu	12	4	2
700 µm Cu	4		
200 µm Fe	2		
100 µm Steel	2		
400 µm Si		1	1

Table 7: List of our substrate and nanoparticles diameter choices.

5 Results

In this section, we discuss the most probable desorption velocities, calculated using both time of flight (TOF) and flythrough time, the particle yield and the fragmentation rate of the LIAD-plume. We further calculate the desorption delay of LIAD by comparing the TOF velocity of the particle to its fly-through time velocity and observe the effect an electric field has on the LIAD particle plume. Finally, we report our observations for PPA-sublimation, both in terms of sample preparation, as well as post-desorption particle distribution.

5.1 Results Laser-induced acoustic desorption

A complete list of LIAD substrates can be found in table 7. We have investigated a multitude of different substrates coated with nanoparticles of different sizes, with $500\,\mu m$ copper making up the majority of investigated substrates. The reason for choosing this substrate lies in the remarkably low velocities observed using thicker copper substrates.

5.1.1 Classification of scattering signals

We will now analyze the scattering signal emitted by the nanoparticles crossing the standing wave of our $1550\,nm$ tweezer and the conclusions regarding their physical reality we make using said scattering signals. As such, we separate the oscilloscope signal curves we want to discuss in two categories (see figure 29). The first will be called Gaussian curves and consists of oscilloscope signals that can be fitted under a Gaussian envelope, as we expect of a single particle, described in section 2.3. The second we will call non-Gaussian curves, which is a collective term for all scattering signals which don't conform to Gaussian envelopes. Curves of this type include lopsided curves, M-shaped scattering curves such as those caused by the scattering signal of two particles passing the tweezer in rapid succession or any number of other curves of arbitrary shape.

5.1.2 Success rate

We define the success rate as the fraction of desorption processes which result in oscilloscope signals indicating particles. The success rates for LIAD can be found in tables 8 and 9, the first of which only treats the success rates regardless of the shape of the scattering signal, which we call the general success rate, while the second shows the success rates for Gaussian scattering signals, which will be called the fraction of Gaussian curves henceforth.

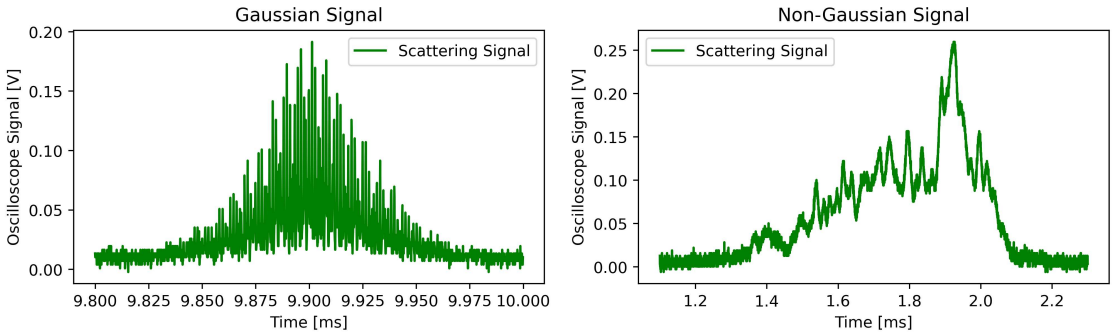

Figure 29: Examples of the two types of scattering signals. The given image depicts scattering signals of $300\,\text{nm}$ SiO_2-particles desorbed from $200\,\mu\text{m}$ iron substrate.

Laser	Ekspla NT 200	InnoLas 400	InnoLas 400	InnoLas 400
Material	$300\,\text{nm}$	$300\,\text{nm}$	$150\,\text{nm}$	$100\,\text{nm}$
5 µm Ti	$\frac{85}{638}$			
50 µm Ti			$\frac{23}{71}$	$\frac{8}{106}$
50 µm Cu	$\frac{19}{184}$			
500 µm Cu	$\frac{13}{180}$	$\frac{88}{1415}$	$\frac{66}{464}$	$\frac{31}{189}$
700 µm Cu	$\frac{31}{391}$			
200 µm Fe	$\frac{16}{161}$			
100 µm Steel	$\frac{13}{169}$			
400 µm Si			$\frac{11}{178}$	$\frac{3}{89}$

Table 8: Success rates for different substrates and nanoparticle diameters for both desorption lasers. This table includes both Gaussian and non-Gaussian curves. The only difference in parameters between Ekspla NT 200 and InnoLas 400 is their pulse length. The Ekspla NT 200 has a pulse length of $3.6\,\text{ns}$ and the InnoLas 400 has a pulse length of $7\,\text{ns}$.

Laser	Ekspla NT 200	InnoLas 400	InnoLas 400	InnoLas 400
Material	$300\,\text{nm}$	$300\,\text{nm}$	$150\,\text{nm}$	$100\,\text{nm}$
5 µm Ti	$\frac{10}{638}$			
50 µm Ti			$\frac{13}{71}$	$\frac{8}{106}$
50 µm Cu	$\frac{4}{184}$			
500 µm Cu	$\frac{3}{180}$	$\frac{66}{1415}$	$\frac{20}{464}$	$\frac{19}{189}$
700 µm Cu	$\frac{6}{391}$			
200 µm Fe	$\frac{4}{161}$			
100 µm Steel	$\frac{1}{169}$			
400 µm Si			$\frac{5}{178}$	$\frac{1}{89}$

Table 9: Success rates for different substrates and nanoparticle diameters for both desorption lasers. This table only includes Gaussian curves.The only difference in parameters between Ekspla NT 200 and InnoLas 400 is their pulse length. The Ekspla NT 200 has a pulse length of $3.6\,\text{ns}$ and the InnoLas 400 has a pulse length of $7\,\text{ns}$

The general success rate of LIAD lies between $3\,\%$ and $32\,\%$, with $32\,\%$ % being an outlier. The average success rate lies at $\approx 10\,\%$. The success rates of different substrates desorbed using the Ekspla NT 200 laser show a spread from $7\,\%$ to $13\,\%$, while the spread of success rates observed for the InnoLas Spitlight 400 is higher with $3\,\%$ to $32\,\%$. The success rate seems to depend little on the substrate material, but rather on the substrate thickness, with $5\,\mu$m Titanium being having by far the highest success rate when desorbing $300\,$nm nanoparticles at $13.3\,\%$, followed by $50\,\mu$m Cu with $10.3\,\%$, while every other material has success rates of below 10 %.

A remarkable difference in success rates can be seen when comparing the nanoparticle diameters. The success rates measured for $150\,$nm SiO_2-nanoparticles desorbed off $50\,\mu$m Ti are remarkably above average at $32\,\%$, as compared to the highest success rate for $300\,$nm SiO_2-nanoparticles, which lies at only $13.3\,\%$, though we see a decrease in success rate for $100\,$nm SiO_2-nanoparticles, likely due to the properties of Rayleigh-scattering (see equation 52). They reduce the amount of scattered light and make them harder to detect.

The substrate best suited for a comparison of nanoparticle diameter and success rate is the $500\,\mu$m copper due to the amount of data available. The success rates are $6.2\,\%$,$14.2\,\%$ and $16.4\,\%$ for $300\,$nm, $150\,$nm and $100\,$nm respectively, showing a noticeable increase in success rate for smaller particles. This increase in success chance for smaller nanoparticles is likely caused by the analyte itself, since the concentration of the nanoparticle solution is defined by mass ratio. As such, a solution containing smaller nanoparticles would need to have a higher number concentration of nanoparticles to maintain said mass ratio.

The fraction of Gaussian curves lies between $0.6\,\%$ and $18.3\,\%$, with $18.3\,\%$ representing $150\,$nm SiO_2-nanoparticles desorbed off $50\,\mu$m Ti, the same outlier as discussed before. The average success rate when only taking into account Gaussian curves lies at around $3\,\%$. There is a significant difference in the fraction of Gaussian curves as compared to the general success chance when comparing the desorption lasers. With the Ekspla NT 200, the Gaussian curves make out $15.8\,\%$ of the total number of curves, while for the InnoLas spitlight 400, they account for $57.4\,\%$. Since the only difference between the lasers lies in their pulse length, the difference between the fraction of Gaussian curves is likely caused by a difference in either the alignment of the $1550\,$nm Tweezer, or an issue with the sample preparation.

5.1.3 Average time-of-flight (TOF) velocities

We employ two different ways to measure particle velocity. Either by measuring the $1/e$-width of the Gaussian curve generated by Rayleigh scattering of a single particle as described in section 2.3, or by measuring the time difference between desorption laser pulse and scattering signal and using the known distance between sample and detection beam (see section 4.2.3) together with said time difference to calculate the average particle velocity between substrate and detection beam. The velocities calculated using the first method will subsequently be called flythrough time velocities, while the second will be called time-of-flight (TOF) velocities. Note that to calculate flythrough time velocities, curves with a Gaussian envelope are required.

Here we investigate the dependency of TOF-velocities (of both non-Gaussian and Gaussian scattering signals) on different substrates and nanoparticle diameters under different environmental electric fields. Figure 30 contains thr average particle velocities together with a histogram containing a representative particle TOF-velocity distribution of $500\,\mu$m copper substrate.

While we used two different desorption lasers during our experiments, there is no difference between them except their pulse length. The only experimental overlap between desorption lasers, $300\,$nm SiO_2-nanoparticles desorbed off a $500\,\mu$m copper substrate without electric field shows

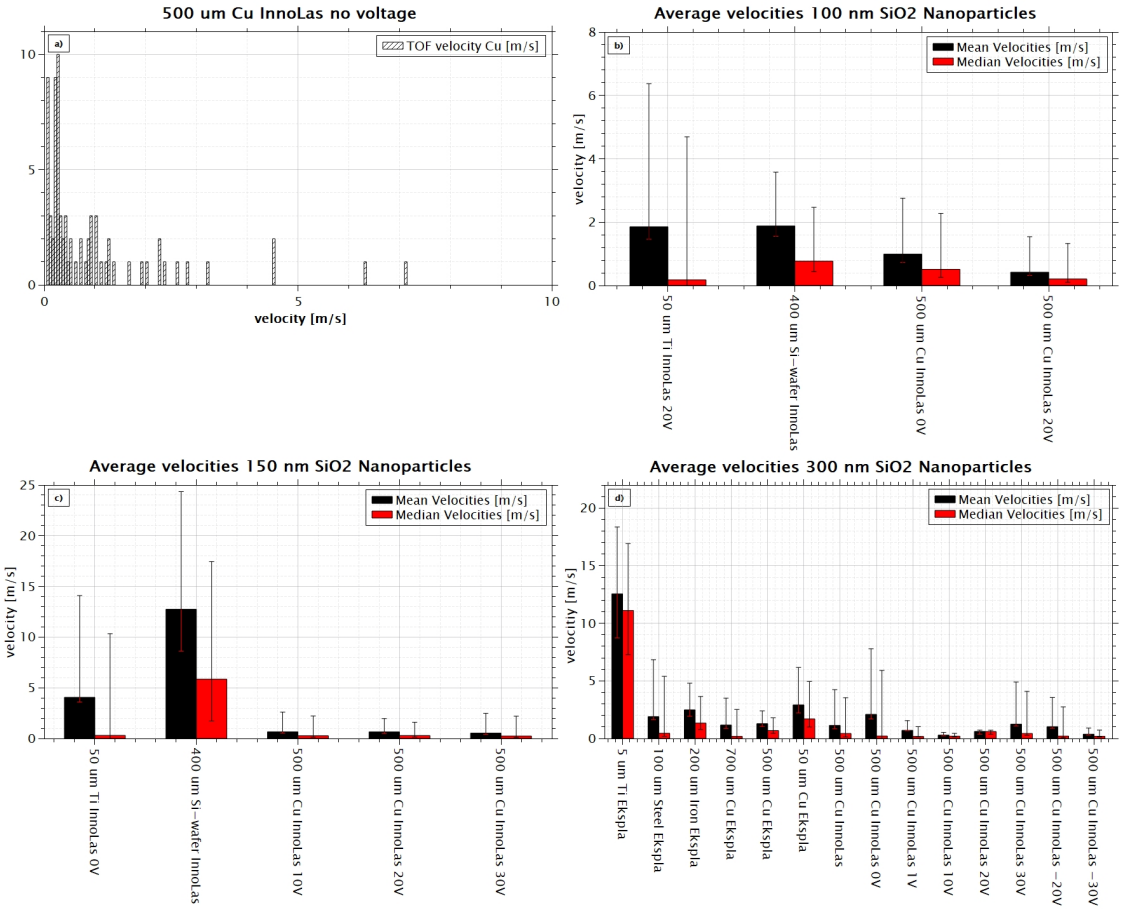

Figure 30: Time-of-flight (TOF) velocities of nanoparticles desorbed using LIAD. **a)** Histogram of the velocity distribution of $300\,\text{nm}$ SiO_2-nanoparticles desorbed of a $500\,\mu\text{m}$ copper foil with no electric field applied to the substrate. We observe a broad distribution of particles with the majority of them at velocities under $4\,\text{m/s}$. **b)** Mean-, as well as median TOF-velocities measured for $100\,\text{nm}$ SiO_2-nanoparticles desorbed of different substrates. The average velocities for different substrates show little spread between them, but have a high standard deviation. **c)** Mean-, as well as median TOF-velocities measured for $150\,\text{nm}$ SiO_2-nanoparticles desorbed of different substrates. We observe a remarkable difference in particle velocity for Si-wafers. **d)** Mean-, as well as median TOF-velocities measured for $300\,\text{nm}$ SiO_2-nanoparticles desorbed of different substrates. The average TOF-velocity for $5\,\mu\text{m}$ Ti-substrate is noticeably higher than the other average velocities. The high standard deviations indicate a broad velocity distribution typical for LIAD. The median velocities are all smaller than the mean velocities, indicating a positive skewness.

minimal difference in particles TOF-velocities, allowing us to make the assumption that thr choice of desorption laser has no influence on the particle TOF-velocities.

Comparing different substrates, we notice the average velocities are higher for thinner substrates. $5\,\mu m$ Titanium substrates show an average TOF-velocity almost four times larger than almost all other substrates. The only comparable substrate to $5\,\mu m$ Titanium are silicon-wafers in conjunction with $150\,nm$ SiO_2-nanoparticles. Thicker substrates show lower average velocities, but the difference in velocity between all substrates except $5\,\mu m$ Titanium is small compared to the standard deviation. This allows us to assume that the substrate choice, as well as nanoparticle diameter (and by extension particle mass) has little influence on the particle velocity. The average velocities for all types of substrates and nanoparticles except $5\,\mu m$ Titanium and one case of silicon-wafers and one series of measurement using silicon wafers are at most $5\,m/s$ or lower.

Figure 30 **b)**, **c)** and **d)** contain particle velocities for different electric fields set between the substrate and a metal plate below the detection beam (see section 4). The voltage given in the diagrams corresponds to the difference in potential between substrate and metal plate. Effectively, $10\,V$ as noted in the diagram involves connecting the substrate to the plus pole of the voltage source while grounding the metal plate beneath it, while $-10\,V$ would mean the opposite. Note that $0\,V$ means both sample as well as metal plate are grounded.

The results of setting a voltage on the substrate are varied. While we were able to observe an increase in average particle velocity between a grounded setup and one that is not grounded or has a current set to it, the difference is small enough that it is insignificant compared to the standard deviation. Additionally, the only noticeable change in particle velocity occurs when grounding the sample, while setting a current to either the substrate or the metal plate beneath it reduces the average velocity as compared to the one measured for a grounded sample.

When comparing the average TOF-velocities, we are able to observe two things which hold true for all substrates and particle diameters. The standard deviation is very high, for some substrates even exceeding the absolute value of the average velocity, indicating a broad velocity distribution and the mean velocity is larger than the median velocity, indicating a positive skew of the velocity distribution. This implies that the majority of nanoparticles will be of a lower velocity than actually given by the mean.

Both of these features are an indication of a Maxwell-Boltzmann velocity distribution, which is typical of particles desorbed by LIAD [74, 128], though in our measurements, we were not able to observe said distribution in any particle velocity histogram, no matter the substrate. The difference between these studies and ours is twofold. They worked with mass spectrometers instead of an optical tweezer for particle detection and investigated the behaviour of molecules instead of nanoparticles (Mass range of $100\,u$ - $5 \times 10^4\,u$ as compared to $3.7 \times 10^{10}\,u$). Assuming the detection method doesn't change the particle velocity distribution, this indicates that the desorption of nanoparticles works with different mechanisms than the one for molecules, likely due to the mass difference, and is non-thermal in nature.

In an effort narrow down our particle velocity distribution, we investigated the position dependence of the desorption velocity by moving it as depicted in figure 22 during the LIAD process. We make a difference between four sections of the sample. The outer edge of the sample near the region where it is glued to its holder, the first and second rings inward from the outer edge and the center of the substrate. The desorption laser impact points are kept at a distance of $500\,\mu m$ to avoid overlap reducing the particle yield, resulting in a total of ≈ 90 desorption events per sample.

The position-dependent mean velocities of four different substrates can be observed in figure

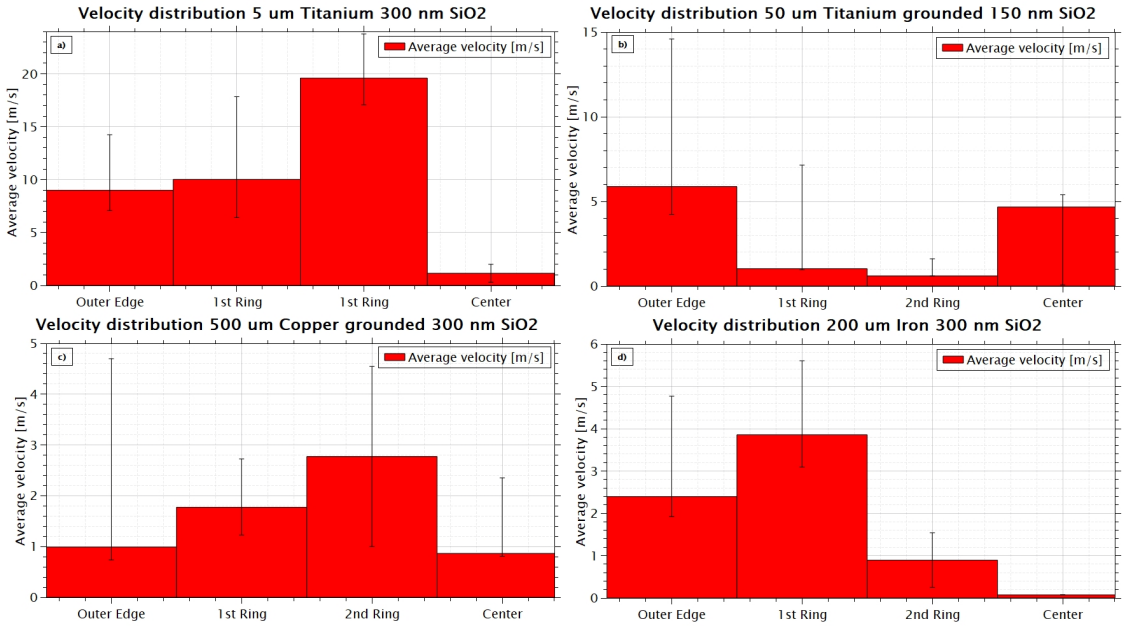

Figure 31: TOF-velocities as a function of the impact position of the desorption laser on the substrate. **a)** For $5\,\mu$m Titanium substrates, we observe a marked difference in particle velocity, between the center and the rest of the sample. **b)** For $50\,\mu$m Titanium substrates, we observe a velocity distribution close to the opposite of a). **c)** The velocity distribution for $500\,\mu$m copper substrates is similar to a), though with less spread between the velocities of different impact positions of the desorption laser. **d)** The velocity distribution for $200\,\mu$m Iron substrates is similar to a) and c), though peaking in the first ring instead of the second.

31. The lowest average velocities for most velocity distributions can be observed in the center of the sample with the only exception being the case of $50\,\mu$m Titanium substrate in conjunction with $150\,$nm-SiO_2 nanoparticles, which show a behaviour opposite to the other substrates .

While this three out of the four velocity distributions look similar, the velocity standard deviations for all four cases are too high to enable further analysis. Only velocity distributions **a)** and **d)** show any difference in position-dependent velocities when taking into account the standard deviation, which is not enough to confirm a trend.

5.1.4 Gaussian curves - Comparison of time-of-flight and flythrough time velocities

We have discussed the properties of the TOF-velocities calculated from both Gaussian and non-Gaussian scattering signals. Now, we will investigate the Gaussian curves, compare their TOF and flythrough time velocities and, by comparing them, calculate the average particle desorption delays of different substrates.

A distribution of both TOF, as well as flythrough time particle velocities for four different substrates can be observed in figure 32. While the TOF-velocity distributions looks different for titanium, the flythrough time velocity spread for the substrates (depicted in figure 32 **b)**, **c)** and **d)**) are all similar to each other, with velocities evenly spread from $0\,$m/s to $9\,$m/s. Comparing TOF and flythrough time velocities, we notice two differences. First, the flythrough time velocities have a broader spread than the TOF velocities and second, the TOF velocities are on average much slower than the flythrough time velocities.

The higher average velocities of the flythrough time velocity as compared to the TOF velocity hint at a significant delay between the impact of the desorption laser and the desorption of the particle. We can make an estimate of the delay time by comparing the time a particle would need to reach the detection beam while flying with the flythrough time velocity and the measured time

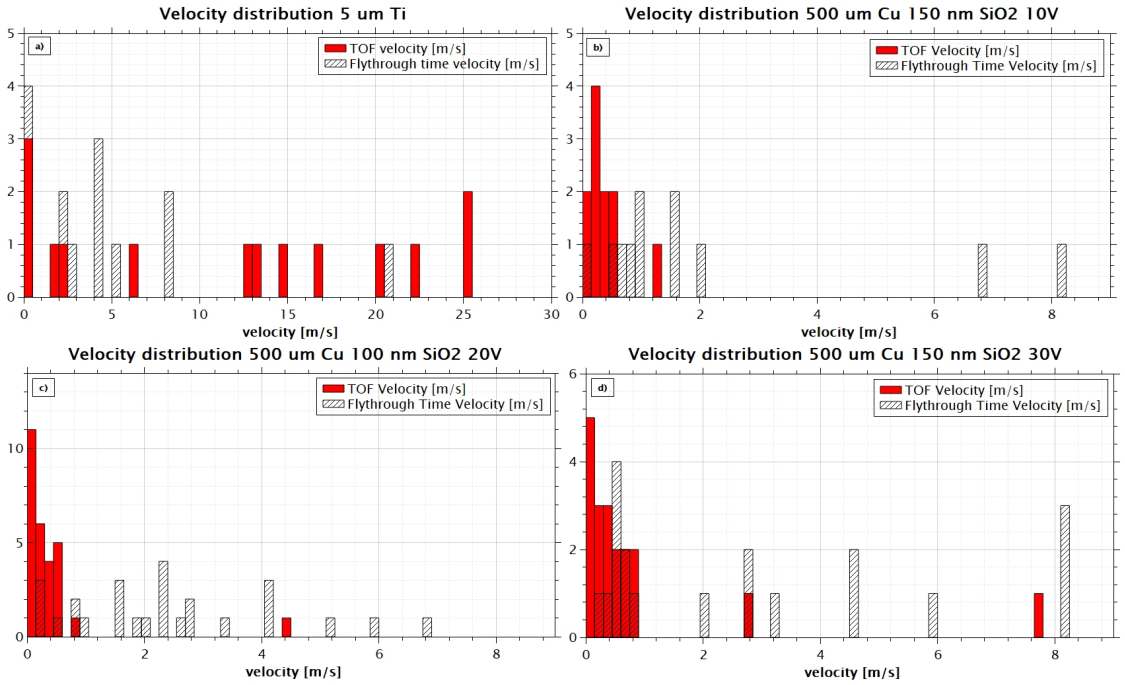

Figure 32: Histograms of nanoparticle TOF and flythrough time velocities for different desorption conditions. **a)** $300\,\text{nm}$ SiO_2-nanoparticles desorbed of $5\,\text{um}$ Titanium substrate. They show a broad velocity distribution, with TOF-velocities evenly spread across the entire velocity range. The flythrough time velocities are spread further than observed in **b)**, **c)** and **d)**, though they are concentrated in a 0 - $4\,\text{m/s}$ interval. In subplots **b), c), d)** SiO_2-nanoparticles desorbed of $500\,\mu\text{m}$ copper substrate with varying electric fields applied to the substrate are depicted. The velocity distribution is largely independent of the electric field applied to the substrate. The flythrough time velocity is narrow, concentrated in the $0-2$ m/s velocity regime, while the TOF-velocities show a broader spread.

of flight:

$$\tau_{\text{delay}} = t_{\text{TOF}} - \frac{D}{v_{\text{Flythrough}}} \tag{102}$$

The delay times calculated this way, as well as a comparison of the average flythrough time velocities to the average TOF-velocities for all substrates are depicted in figure 33.

The flythrough time velocities are comparable through all substrate choices, particle diameters and electric fields. The average flythrough time velocities across all of our measurements don't exceed $5\,\text{m/s}$, which is slower than what was found in previous, comparable measurements [60].

We expect the mean TOF-velocity to always be slower than the mean flythrough time velocity, since any delay in particle desorption should only reduce the apparent TOF-velocity, but this is not the case in our measurements. While the mean delay time is positive for most cases, we observe average TOF-velocities higher than flythrough time velocity averages on multiple occasions. These negative delay times occur, with three exceptions, only when using the Ekspla 200 desorption laser.

It is possible that the high rate of negative delay times is caused by a mistake in the alignment of the detection beam. If the alignment of the detection beam is improper (for example due to the incoming beam and the back-reflected beam not fully overlapping), the actual beam diameter differs from the beam diameter calculated from the known beam diameter before focusing. A broader beam waist naturally broadens the scattering curves. This can lead to the assumption of slower flythrough time velocities. When changing our desorption laser setup, we re-aligned the detection beam, after which the average delay times were mostly positive. Of the three cases of negative delay times, two have been calculated using only a single scattering signal as reference,

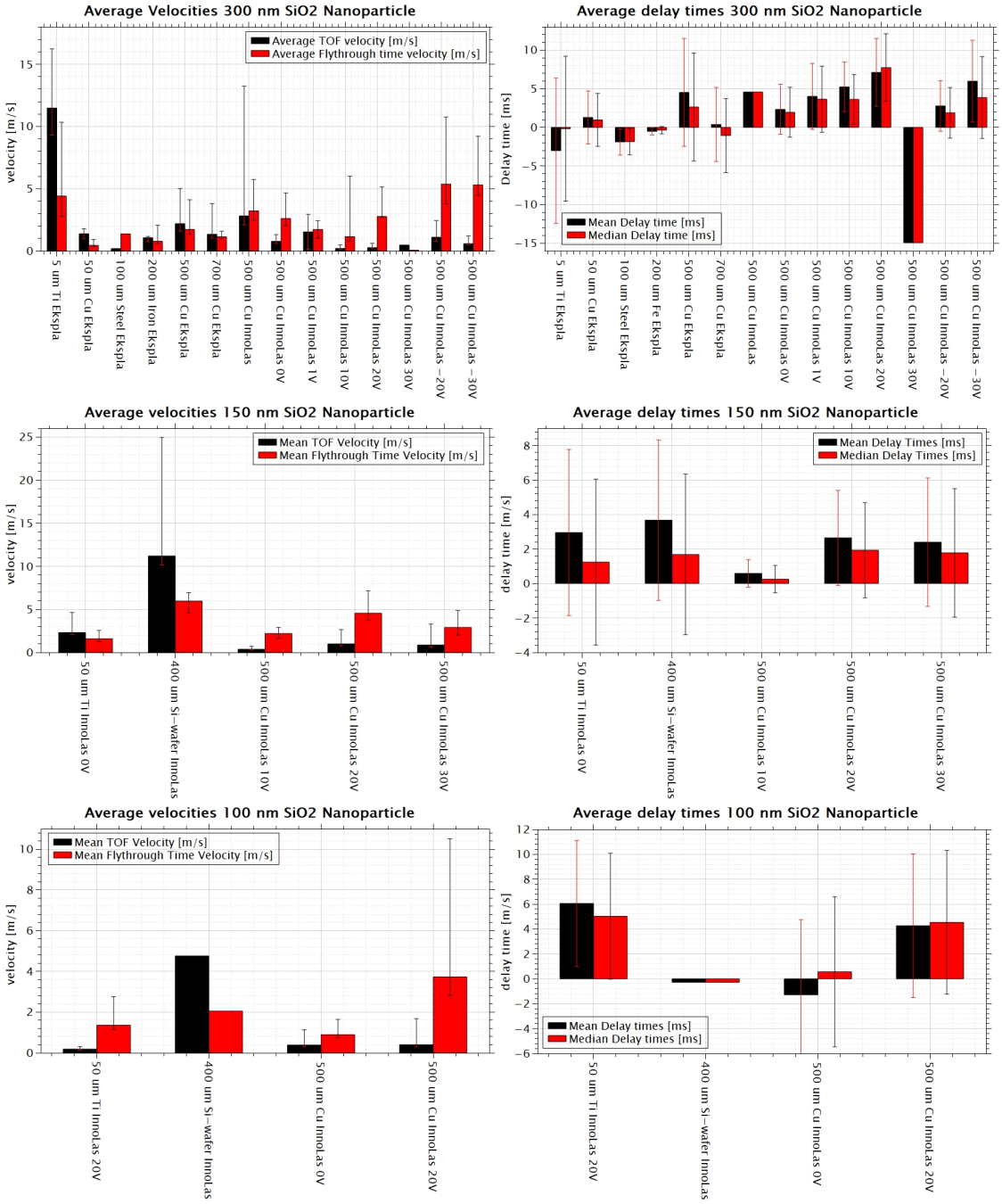

Figure 33: A comparison of the average TOF- and flythrough time velocities for different substrates and nanoparticle diameters and the particle emission delay times calculated by comparing them.

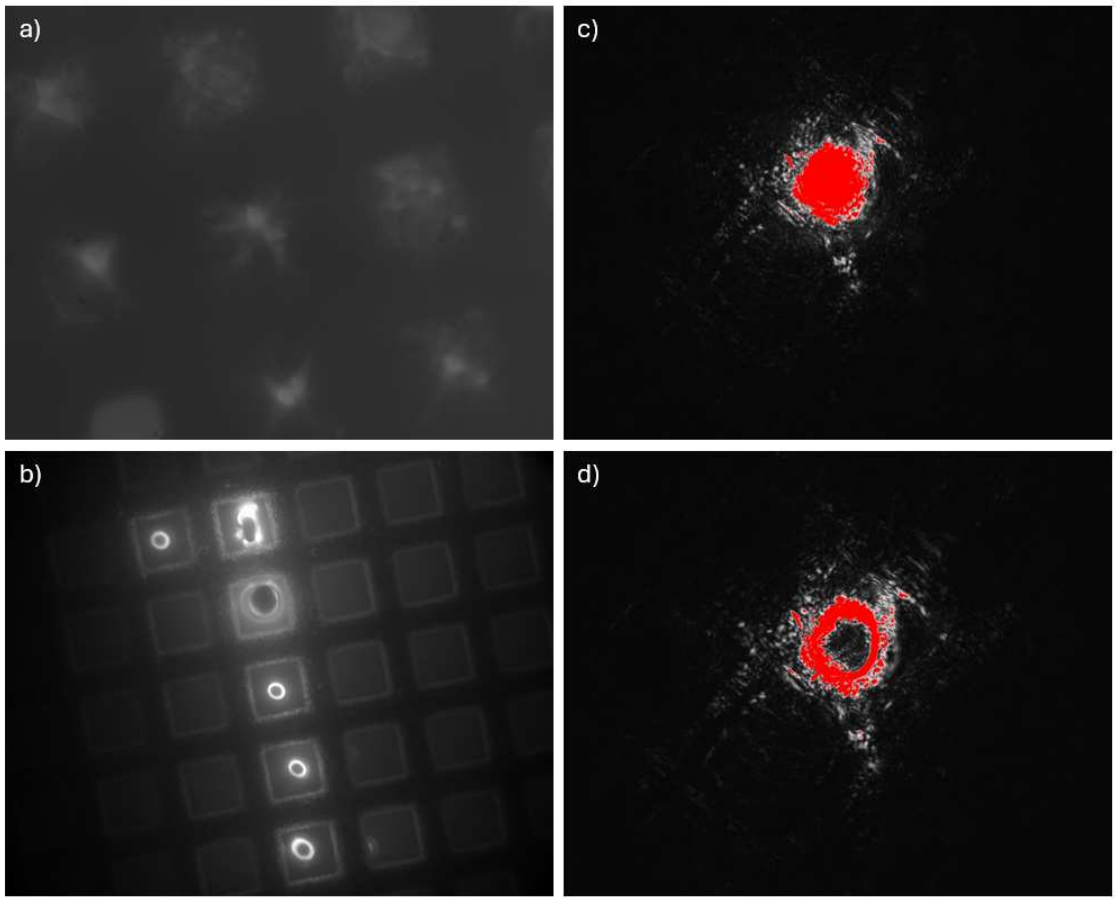

Figure 34: Microscopy images of a TEM grid sample depicting the sublimation of the PPA substrate. **a)** In-situ microscopy image of the TEM grid using a flashlight as light source. **b)** The same TEM grid after PPA sublimation under a fluorescence microscope with $40\times$ magnification. We observe circular holes in the PPA caused by the $405\,\text{nm}$ sublimation laser. **c)** In-situ image of a PPA substrate inside a TEM grid being irradiated by the sublimation laser. This picture was taken before the melting of the PPA. **d)** The same image as depicted in c), this time after the melting of the PPA-layer.

allowing us to classify them as outliers, while the third was similarly caused by a single outlier curve influencing the whole statistic.

5.2 Results (Poly-)Phtalaldehyde sublimation

When talking about our experimental results regarding PPA sublimation, we have to first mention, that until a few days before publishing this thesis, we were unable to observe the scattering curve of a nanoparticle passing through the detection beam. As such, we will be discussing the melting behaviour of the PPA inside a TEM grid and microscopy images of the particle distributions of gold-, as well as SiO_2 nanoparticles which were desorbed on a microscopy slide using PPA sublimation. We also will discuss possible reasons for our initial inability to observe particles.

5.2.1 (Poly-)phtalaldehyde sublimation behaviour

To observe the sublimation of PPA in-situ, we use the light microscope built in our experimental setup, which with our choice of lenses (see section 4.1.2) has a magnification of $M \approx 30$. An image of a 400 mesh TEM grid taken via the in-situ microscopy setup can be observed in figure 34 **a)**. The image in question was taken using a flashlight placed above the TEM grid as the light source of the light microscope. During the sublimation of PPA, the $405\,\text{nm}$ desorption laser replaces said flashlight as light source.

The behaviour of a PPA layer in a TEM grid during the sublimation process is depicted in figure 34 **c** and **d**. We observe a red spot representing the reflection of the desorption laser on the PPA in the center of a cell of the TEM grid. With a desorption laser power of $100\,\text{mW}$ (corresponding to $50\,\text{mW}$ power on the substrate, see 3.2.3), the spot in question transforms into a ring-shape over the course of $\approx 1\,\text{s}$ as the beam sublimates the PPA. A microscopy image of the TEM grid after this sublimation takes place can be found in figure 34 **b)**. We observe holes of mostly homogeneous sizes with diameters of $\approx 10\,\mu\text{m}$ in the center of the PPA. The holes in the PPA layer are by a factor of 3 larger than the desorption laser waist ($3\,\mu\text{m}$), implying the dissolution of the PPA either due to heat propagation in the polymer or due to dissolution of PPA chains spreading beyond the spot of the material heated by the laser in a chain reaction.

While the laser-diameter and the diameter of the hole in the PPA-layer don't conform to each other, we are still able to sublimate small sections of the PPA in a controlled manner with the desorption laser, implying a desorption of particles.

5.2.2 Particle distribution of a (Poly-)phtalaldehyde sublimation plume

Using PPA sublimation, we are unable to observe nanoparticles in our detection setup despite being able to observe the desorption process itself. If SiO_2-nanoparticles either melt after desorption (e.g. because of laser heating of their fluorophores), or aren't guided into the tweezer by the desorption beam, we can explain our lack of observable nanoparticles in the detection beam after desorption.

To observe the behaviour of the nanoparticle plume generated by PPA sublimation, we place two microscopy slides at $300\,\mu\text{m}$ distance above, as well as below the substrate and desorb nanoparticles via PPA sublimation. The resulting particle distribution is observed in a Transmission electron microscope. The resulting images are depicted in figure 35.

After desorption, both microscopy slides were laced with nanoparticles. Both slides showed a similar particle distribution and flat crystal structures of $5\,\mu\text{m}$ to $10\,\mu\text{m}$ diameter with snowflake-like appearance, which are likely composed of re-condensed PPA. The crystal structures on the slide are placed at an average distance between $10\,\mu\text{m}$ to $20\,\mu\text{m}$. Considering the repetition rate of our TEM grid (400 mesh) is $37\,\mu\text{m}$, it is unlikely that the PPA travels directly to the microscopy slide before condensing and instead condenses randomly on the substrate. The only difference in nanoparticle distribution between slides lies in the quantity of nanoparticles with the lower slide having a higher particle concentration. The desorbed nanoparticles in figure 35 **b)** are highly concentrated. In addition, their diameters are at least a factor 2 smaller than those of the complete nanoparticles seen in figure 35 **c)** and **d)** and resemble the droplets in the background of figure 35 **d)** more closely. This leads us to assume that some nanoparticles melt during desorption and are deposited on the microscopy slide as droplets.

A closeup of the nanoparticles which were desorbed whole reveals that their diameter as given by the manufacturer ($300\,\text{nm}$) mismatches with their observed diameter ($100\,\text{nm}$ to $200\,\text{nm}$). The desorbed nanoparticles are spherical in shape and their size distribution is uniform, implying an issue with the prefabricated nanoparticles rather than a loss of particle mass during desorption. The nanoparticles are desorbed either alone or in groups of two or three with no observations of bigger clusters.

Through figure 35 **a)** to **c)**, we were able to confirm that the desorbed nanoparticles travel in the direction of the detection beam. This lets us conclude that the radiation pressure pushes a fraction of the nanoparticles upwards as suggested by the simulations in section 3.2.4.

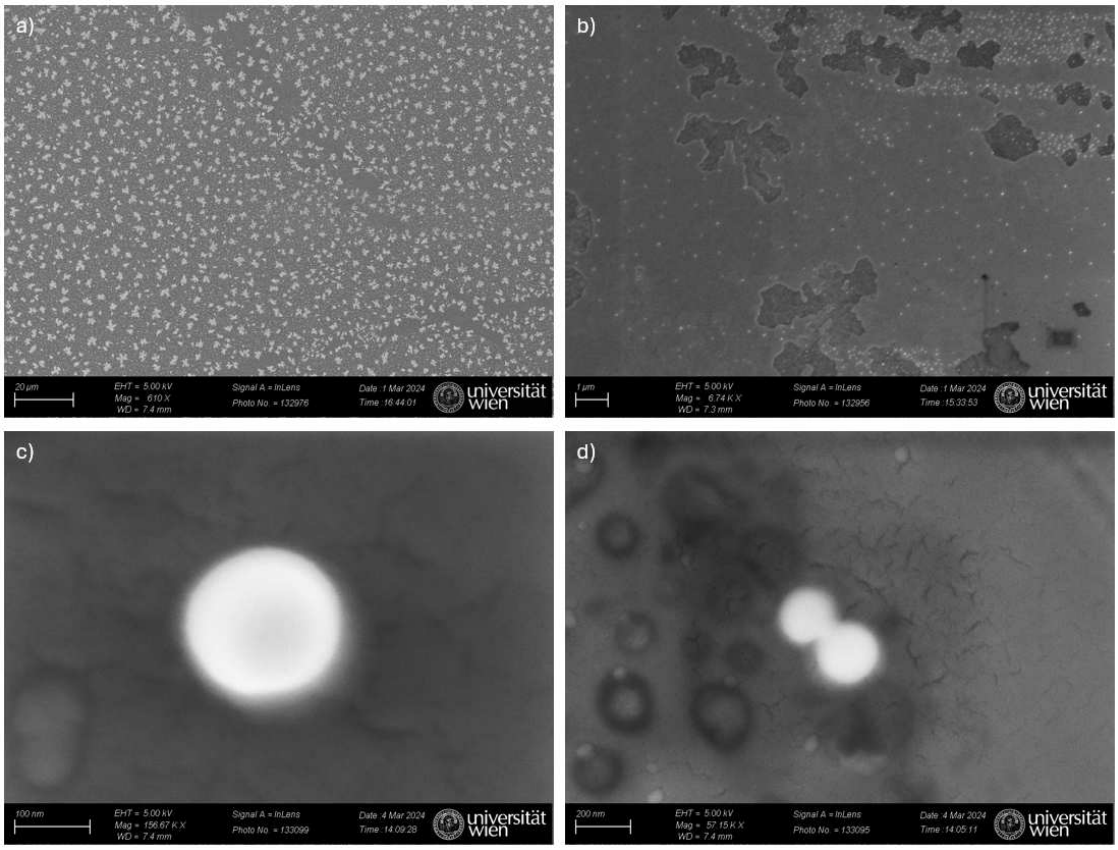

Figure 35: Microscopy images of nanoparticles desorbed using PPA sublimation. **a)** TEM-image of a Microscopy slide placed above a PPA-filled 400 mesh Ni grid nebulised with $300\,\mathrm{nm}$ SiO_2-nanoparticles after multiple desorption events. Besides the nanoparticles, we spot patches of crystal, which we assume to be recondensed PPA. **b)** Closeup of the same slide. The concentration of nanoparticles is high and their diameter is lower than the one we observe in c) and d). **c)**, **d)** Imaging single nanoparticles on the microscopy slide from a) and b) reveals the nanoparticles to be desorbed either alone or in groups of two to three. Additionally to the nanoparticles, we observe small droplets of what we assume to be SiO_2 which stem from nanoparticles melted under the laser.

6 Discussion and outlook

Here we will discuss the properties of the investigated desorption techniques as a particle sources for optomechanics. We compare the average velocities and velocity distributions observed for LIAD with those necessary to trap a particle and discuss improvements to PPA-sublimation to allow for the observation and hopefully trapping of desorbed particles.

6.1 Laser-induced acoustic desorption

When discussing LIAD, there are a few questions that are of interest for us. What kind of further manipulation of the volatilised particles is necessary to trap them? How would we need to modify our setup to make trapping possible? And what improvements could be made to the source? In this section we will make an effort to answer these questions based on the experimental data discussed in section 5 above.

First we want to determine if it is theoretically possible to use our setup for trapping. To determine if it is possible to trap a given nanoparticle from any source, we can compare the kinetic energy of the particle to the potential depth of the trap. In the dipole approximation, the potential depth of an optical tweezer for a given spherical nanoparticle with polarisability α is given by (compare section 2.2.2):

$$U(\vec{\rho}, z) = \frac{\alpha}{2\epsilon_0 nc} \cdot I(\vec{\rho}, z) \tag{103}$$

Usually, one would also need to consider the radiation pressure force of the tweezer and its magnitude compared to the gradient force (see section 2.2.2), but since we work with a double-sided tweezer, we only need to consider the trapping potential of the tweezer and the kinetic energy of the nanoparticle.

If we insert the polarisability of a $300\,\text{nm}$ SiO_2-nanoparticle, as well as the Intensity of our detection beam at focus ($I_0 \approx 4.8 \times 10^9\,\text{W/m}^2$) into this equation, we arrive at a potential depth of:

$$U_{\text{det}} \approx 9.013 \times 10^{-20}\,\text{J} = 0.56\,\text{eV} \tag{104}$$

We insert this potential into the equation for kinetic energy $E_{\text{kin}} = mv^2/2$, together with the mass of a $300\,\text{nm}$ SiO_2-nanoparticle $m = 3,75 * 10^{-17}$ kg and arrive at a velocity $v_p \approx 0.14\,\text{m/s}$. This is the maximal particle velocity, which still allows for a trapping event to happen. The given velocity is far below the average velocities we found for LIAD. In fact, this velocity is below even the gravitational acceleration a $300\,\text{nm}$ SiO_2-nanoparticle would experience if one were to let it fall from substrate to tweezer ($1\,\text{mm}$ distance in our experiments) in perfect vacuum, which would be $0.16\,\text{m/s}$.

The average particle velocity for LIAD is low and a significant proportion of the flythrough time velocities of the detected particles are below $1\,\text{m/s}$. Nonetheless, the $1550\,\text{nm}$-tweezer, which is used for particle detection in our setup is not able to trap particles due to its shallow potential. If we wanted to trap particles in our setup, we would have to deepen the potential of our tweezer by either increasing the polarisability of our nanoparticles or by increasing the tweezer-intensity.

Increasing the nanoparticle polarisability by increasing its diameter wouldn't improve upon our issue, since both kinetic energy and trap potential scale at the same rate with the particle diameter. This leaves only using a nanoparticle of a material with higher specific permittivity or reducing the tweezer diameter/wavelength to allow for particle trapping. Exchanging the nanoparticle material or the tweezer wavelength would cause the nanoparticles to no longer be

$300\,\text{nm}$ SiO_2-Nanoparticle	$150\,\text{nm}$ SiO_2-Nanoparticle	$100\,\text{nm}$ SiO_2-Nanoparticle
$44/66 \approx 66\,\%$	$26/48 \approx 54\,\%$	$15/41 \approx 37\,\%$

Table 10: Trapping probabilities of the nanoparticles we observed when assuming a narrower tweezer with $1\,\mu\text{m}$ waist.

transparent to the tweezer, resulting in their eventual evaporation (see section 3.2.4). As such, the reduction of tweezer-diameter seems to be the only change we could make to our setup in order to allow it to the trapping of particles.

If we assume a reduction of the tweezer waist to $1\,\mu\text{m}$, its new potential is:

$$U_{\text{det}} \approx 3.8 \times 10^{-17}\,\text{J} \approx 237.9\,\text{eV} \tag{105}$$

The corresponding maximal velocity to trap a particle lies at $v_p \approx 1.42\,\text{m/s}$. Comparing this value with the flythrough time velocities we obtained, we can estimate the fraction of single nanoparticles (as indicated by their Gaussian scattering curves) we would have been able to trap with a narrower tweezer. The result can be observed in table 10.

We conclude that using our current setup in conjunction with a desorption laser of $1\,\mu\text{m}$ waist, about half of the single particles we observed were trappable. While this is a significant fraction, the low rate of observed scattering Signals in conjunction with the smaller detection/trapping region a narrower tweezer offers would make a trapping event still very unlikely. If we assume the trapping region of a $1\,\mu\text{m}$ waist tweezer to be equal to the detection region of a $20\,\mu\text{m}$ waist tweezer, we would trap 1 particle in 100 desorption events on average. In practice we would trap less particles than that due to the smaller trapping region of a narrower tweezer.

While the rate of Gaussian curves to trapping events is high, the rate of desorption events to Gaussian curves is low, which can be increased by two ways. Either we can increase the tweezer waist, which is not possible if we want to trap particles, or we can change the source parameters. If we were to decrease the distance between sample and tweezer, the nanoparticle plume would be more focused, resulting in more particles crossing the tweezer while keeping the total amount of desorbed particles constant. This would increase trapping chances without changing the probability of polluting the trap optics with desorbed particles.

Another possible area of improvement would be the sample preparation. In the microscopy images of the particle distribution of our LIAD substrates from section 4.2.2, we observe patches of high particle density, while other region are almost devoid of particles. It is a reasonable assumption that our low success rate can be partially derived from this imbalance in the particle distribution, since a desorption event in an area almost entirely devoid of particles would likely see a very low success rate. As such, ensuring a more homogeneous particle distribution could be an easy way to improve our success rate without increasing the maximal number of particles desorbed per desorption event and thereby not significantly increasing the chances of contamination of our optics.

6.2 (Poly-)Phtalaldehyde sublimation

Our observations for PPA sublimation were somewhat contradictory. On the one hand, we were able to not only observe the sublimation of PPA in-situ, but we could also observe a particle distribution on a glass slide placed between tweezer and substrate, letting us conclude that part of the particle plume indeed propagates in the desired direction. On the other hand, for the longest time we were unable to observe any nanoparticles in our tweezer. In this section, we will first discuss the reliability of the desorption laser as particle guide considering the discrepancy in

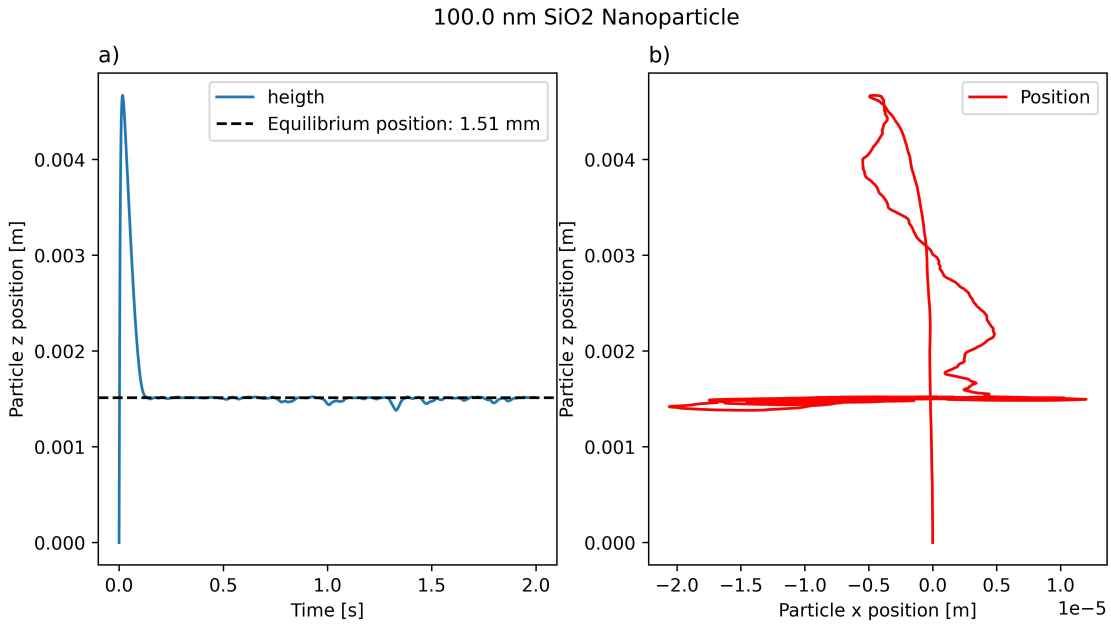

Figure 36: Simulation of the trajectory of a $100\,\text{nm}$ SiO_2-nanoparticle after sublimation. We assume the desorption to occur at a pressure of $5\,\text{pa}$ with a desorption laser at $3\,\mu\text{m}$ waist and with a power of $50\,\text{mW}$. **a)** z-position of the nanoparticle after melt-out as a function of time. The initial acceleration of the particle is followed by a gravity counteracting the radiation pressure until the particle reaches an equilibrium z-position. Some slight oscillations in the equilibrium z-position due to brownian motion are observable. **b)** Particle position after sublimation. The initial acceleration is so strong that the Brownian motion almost plays no role. The gradient force is strong enough to counteract Brownian motion, though we observe significant lateral particle movement.

particle diameters between manufacturer specifications and reality (see section 5.2.2). After this, we will consider any other issues that may have prevented us from observing particles desorbed with PPA sublimation.

6.2.1 (Poly-)Phtalaldehyde sublimation particle guide for the observed beam diameters

Until now, we have assumed the simulation in section 3.2.4 to be correct and the desorption laser to work as a particle guide. What we neglected in this assumption were the nanoparticle diameters observed under TEM (see section 5.2.2) with average diameters of $100\,\text{nm}$ to $200\,\text{nm}$, as opposed to the initially assumed $300\,\text{nm}$ particle diameter. A reduced particle diameter results in a reduction in gradient force and an increased influence of Brownian motion on the nanoparticle trajectory. Combining these two factors, it is easy to assume that the power of the desorption beam would become insufficient to guide particles of such diameters.

To verify this assumption, we simulated the particle behaviour of a $100\,\text{nm}$ nanoparticle, as observed under TEM, after PPA-sublimation. The result can be observed in figure 36. While there is a significant reduction in the amplitude of the initial acceleration of the particle, which now only reaches less than $5\,\text{mm}$, the gradient force of the desorption beam is still significant enough to act as particle guide. In fact, lower particle diameters seem better suited to observe particles in the tweezer, since their decreased initial velocities imply that they are in the tweezer-region for longer periods of time. Apart from the amplitude of the particle z-position, the only significant difference between figure 36 and figure 16 is the presence of significant Brownian motion in the direction of the optical axis of the desorption laser while the particle is in equilibrium position, which should have no negative influence on our ability to detect the nanoparticles during their

initial acceleration.

In conclusion, while the particle trajectories differ for smaller nanoparticles, the observed difference in particle diameter shouldn't make any influence in our ability to observe particles with our detection beam setup.

6.2.2 (Poly-)Phtalaldehyde sublimation with a working particle guide

The desorption laser acts as a particle guide and particles are desorbed during the sublimation of the PPA. This leaves only one possibilities regarding our failure to observe particles during PPA sublimation. There was a problem with the alignment of desorption and detection beam.

Shortly before handing in this Thesis, we were able to observe scattering curves we believe to belong to nanoparticles after a realignment of the tweezer. The nanoparticles were observed at two different environmental pressures. At 0.06 mBar, the nanoparticles cross the tweezer with a flythrough time velocity of 2 m/s to 20 m/s, which is comparable to LIAD, though for a detailed study more data is still necessary. At ambient pressure on the other hand, the air drag forces slow the desorbed nanoparticles down considerably and cause it to stay in the tweezer for 0.25 s on average. In light of these new results, we can conclude that PPA sublimation is a valid desorption source, though its suitability for trapping remains to be seen.

6.3 Conclusion

We investigated two sources of nanoparticles and their suitability for optomechanics. An analysis of the velocity distributions of particles desorbed with LIAD was made and the reason why no particles were observed when using PPA-sublimation as desorption method was investigated. In conclusion, while LIAD shows remarkably low velocities, theoretically allowing for frequent trapping assuming a narrow enough tweezer waist, its inherent randomness and the low number of desorbed particles result in a low trapping success rate. The trapping rate could be increased by either decreasing the distance between tweezer and substrate or by improving the coating method of the substrate to ensure a more homogeneous particle distribution.

PPA sublimation was be proven to desorb particles which are be guided by the desorption beam into the tweezer. In fact, at the time of writing this Thesis, we have successfully observed nanoparticles in the tweezer. Our former inability to observe nanoparticles was caused by a mistake in laser alignment. With the correct alignment of desorption laser and tweezer, we are able to observe nanoparticles that stay in the tweezer for $\approx 0.25\,\mathrm{s}$ at ambient pressure and cross the tweezer with at velocities between $2\,\mathrm{m/s}$ and $21\,\mathrm{m/s}$ at $0.06\,\mathrm{mBar}$ pressure.

7 Appendix A: Scattering properties of a nanoparticle in a tweezer

This section contains the python code used to estimate the particle trajectory in a double-sided tweezer and the corresponding scattering signal.

```
import numpy as np
import matplotlib.pyplot as plt
import scipy.constants as cst
from scipy.signal import find_peaks
from matplotlib.patches import ConnectionPatch

fig, ax = plt.subplots(2, sharex=True, figsize=(7, 5), dpi =400.0)
# Define the function and the axes of our Plot


# Definition of Tweezer Variables and Physical constants
w_0 = 2.055e-5
# Waist of the tweezer
lambda_tweez = 1.55e-6
# Tweezer Wavelength
z_R = cst.pi*w_0**2/lambda_tweez
# Raileigh length
P_0 = 3.2
# Tweezer Power
k = 2*np.pi/lambda_tweez
# Wavenumber
I_0 = 2*P_0/np.pi/w_0**2
# Peak Intensity

# Define the initial parameters of the Paricle (in SI units)
s_xinit = 5e-5 # Initial particle x position
s_zinit = 0     # Initial particle z position
v_xinit = -5   # Initial particle x velocity
v_zinit = 0.5     # Initial particle z velocity
a_xinit = 0     # Initial particle x acceleration
a_zinit = 0     # Initial particle z acceleration

r_p = 1.5e-7
# Particle radius
rho = 2650
# Density Silicone (Particle material)
m_p = 4*cst.pi/3*r_p**3*rho
# Mass Silicone Particle
eps = 2.07
# Dielectric Constant Silicone
# Particle Polarizability
alpha = 4*cst.pi*cst.epsilon_0*r_p**3*(eps-1)/(eps+2)
# Scattering Cross section
sigma_sc = k**4*alpha**2/6/np.pi/cst.epsilon_0**2

# Define the Parameters of the background Gas
```

```
T_e = 300
# Enviromental Temperature in Kelvin
r_N2 = 0.155e-9
# van der Waals radius of the nitrogen molecule (m)
m_g = 28*cst.atomic_mass
# Average Mass of the Background Gas
p_g = 5
# Background Pressure in Pascal

v_mp = np.sqrt(8*cst.k*T_e/np.pi/m_g)
# mean velocity of the background gas
sigma_coll= np.pi*(2*r_N2)**2
#collisional cross section of nitrogen (m^2)
n = p_g/(cst.k*T_e)
# nitrogen volume density (m^-3)
L_mfp = 1/(n*sigma_coll)
# mean free path for N2 at 5 Pa
eta_N2 = 1/3 * n * m_g * v_mp * L_mfp
# kinematic viscosity of the ideal gas
T_mfp = L_mfp/v_mp
# Mean time of free flight of N2 at 5 Pa
Kn = L_mfp/r_p
# Knudsen number
c_K = (0.31*Kn)/(0.785 + 1.152*Kn + Kn**2)


# Forces axting on a particle passing through the light field
t_ges = 2e-5
# Simulation time
steps = 1e-8
# Timestep of the simulation
stepnumber = int(np.round(t_ges/steps))
# Number of Steps in the Simulation
time = np.zeros(stepnumber)
time[0] = steps

# Initialization of the Particle movement vectors
s_x = np.zeros(stepnumber)
s_z = np.zeros(stepnumber)
v_x = np.zeros(stepnumber)
v_z = np.zeros(stepnumber)
a_x = np.zeros(stepnumber)
a_z = np.zeros(stepnumber)
s_x[0] = s_xinit
s_z[0] = s_zinit
v_x[0] = v_xinit
v_z[0] = v_zinit
a_x[0] = a_xinit
a_z[0] = a_zinit
# Initialize the Intensity of the light field
I_pos = np.zeros(stepnumber)
I_env = np.zeros(stepnumber)
```

```
x_part = s_x[0]
z_part = s_z[0]
vx_part = v_x[0]
vz_part = v_z[0]
w_zpart = np.zeros(stepnumber)
w_zpart[0] = w_0*np.sqrt(1+ (z_part/z_R)**2)
R_part = z_part*(1+(z_R/z_part)**2)

I_pos[0] = 4*P_0/w_zpart[0]**2/np.pi*
            np.exp(-2*x_part**2/w_zpart[0]**2)
           *np.cos(k*z_part+ k*x_part**2/2/R_part+
                   np.arctan(z_part/z_R))**2

I_env[0] = 4*P_0/w_zpart[0]**2/np.pi*
            np.exp(-2*x_part**2/w_zpart[0]**2)

for n in range(0,stepnumber-1):
    # Define the forces acting on the particle
    f_g = m_p*cst.g

    f_xdip = -2*I_0*alpha/cst.epsilon_0/cst.c*w_0**4
             *x_part/w_zpart[n]**4*
             np.exp(-2*x_part**2/w_zpart[n]**2)*np.cos(k*z_part)**2

    f_zdip = -4*I_0*alpha*z_part/cst.epsilon_0/cst.c/k**2/
             w_zpart[n]**4*np.exp(-2*x_part**2/w_zpart[n]**2)*
             (2*x_part**2/w_zpart[n]**2 - 1)

    fx_stokes = - 6*np.pi*eta_N2*r_p*0.619/(0.619 + Kn)*c_K*vx_part

    fz_stokes = - 6*np.pi*eta_N2*r_p*0.619/(0.619 + Kn)*c_K*vz_part

    # Update acceleration of the particle using the forces
    a_x[n+1] = (f_xdip + fx_stokes)/m_p
    a_z[n+1] = (f_g + f_zdip + fz_stokes)/m_p
    # Updating of the Velcoities
    v_x[n+1] = v_x[n] + a_x[n+1]*steps
    v_z[n+1] = v_z[n] +a_z[n+1]*steps
    # and positions
    s_x[n+1] = s_x[n] + v_x[n+1]*steps + 0.5*a_x[n+1]*steps**2
    s_z[n+1] = s_z[n] + v_z[n+1]*steps + 0.5*a_z[n+1]*steps**2
    # Define new particle position/velocities/accelerations
    x_part = s_x[n+1]
    z_part = s_z[n+1]
    vx_part = v_x[n+1]
    vz_part = v_z[n+1]
    # and the corresponding Tweezer waist
    w_zpart[n+1] = w_0*np.sqrt(1+ (z_part/z_R)**2)
    R_part = z_part*(1+(z_R/z_part)**2)
    # Calculate the Tweezer Intensity and update the time vector
    I_pos[n+1] = 4*P_0/w_zpart[n]**2/np.pi*
                 np.exp(-2*x_part**2/w_zpart[n]**2)
```

```
                    *np.cos(k*z_part+ k*x_part**2/2/R_part+
                            np.arctan(z_part/z_R))**2

    time[n+1] = time[n] + steps
    I_env[n+1] = 4*P_0/w_zpart[n]**2/np.pi*
                 np.exp(-2*x_part**2/w_zpart[n]**2)

# Fraction of Scattered Intensity caught by the scattering fiber
I_scat = I_pos*sigma_sc*0.5/4/np.pi
I_scatenv = I_env*sigma_sc*0.5/4/np.pi



# Plot the scattered Intensity
ax[0].plot(s_z, I_scat, "b", s_z, I_scatenv, "r")
# Label the Inetensity of the scattered light
ax[0].set_ylabel("Scattered Intensity [W/m^2]")

# Definition of the space the Tweezer should be depicted over
ind_point = np.argmin(np.abs(s_x))
# Index where the particle crosses the Center of the tweezer
z_point = s_z[ind_point]
# Convert the index into coordinates on the tweezer axis
res = 800
# Resolution we want the Lightfield to have

x = np.linspace(-3.5e-5, 3.5e-5, res)
z = np.linspace(-1e-8, 1.e-5, res)

y = [np.min(s_z), np.max(s_z)]
# Definition of the Intensity Field of the Tweezer
w_z = w_0*np.sqrt(1+ (z/z_R)**2)    # Tweezer radius
R = z*(1+(z_R/z)**2)                # Wavefront curvture
I = np.zeros((x.size, z.size))
for i in range(x.size):
    for j in range(z.size):
        I[i, j] = 4*P_0/w_z[j]**2/np.pi*
                  np.exp(-2*x[i]**2/w_z[j]**2)
                  *np.cos(k*z[j]+ k*x[i]**2/2/R[j]+
                          np.arctan(z[j]/z_R))**2
        # Intensity

# Removal of the boundary conditions
I = I[:-1, :-1]


# Determine the maxima and minima of the Intensity
I_min = np.min(I)
I_max = np.max(I)

# Create the Colormap of the intensity Field
c = ax[1].pcolormesh(z, x, I, cmap='Reds', vmin=I_min, vmax=I_max)
```

```
ax[1].axis("off")

# Plot the Trajectory of the Particle
ax[1].plot(s_z,s_x, "k")
ax[0].set_xlabel("Time [us]")
ax[0].xaxis.set_label_coords(0.95,-0.13)
ax[0].xaxis.set_tick_params(labelbottom=True)
xticks = np.arange(0, 1e-5, 2e-6)
xlabels = [str(np.round(q*2, 1)) for q in xticks*1e6]
ax[0].set_xticks(xticks)
ax[0].set_xticklabels(xlabels)

# Add the numbering of the subplots
ax[0].text(2e-7, 6.4e-7, "a)", size=15, ha="center", va="center")
ax[1].text(2e-7, -4.3e-5, "b)", size=15, ha="center", va="center")
```

8 Appendix B: Substrate displacements and thermal waves

This section contains a different form of the thermal wave equation for the case of a moving substrate, which can be simplified into equations 55 and 56, as well as estimations of thermal waves and central foil displacements calculated using equations 81 67 63. Additionally, this section contains the python code used to estimate said thermal waves and central foil displacements. The thermal waves attenuation due to the plasma plume is estimated as in section 3.1.6.

$$\frac{\partial 1/\rho}{\partial t} - \frac{\partial u}{\partial m} = 0 \tag{106}$$

$$\frac{\partial u}{\partial t} - \frac{\partial P_i + P_e}{\partial m} = 0 \tag{107}$$

$$\frac{\partial e_i}{\partial t} + P_i \frac{\partial u}{\partial m} = -\gamma \frac{(T_e - T_i)}{\rho} \tag{108}$$

$$\frac{\partial e_e}{\partial t} + P_e \frac{\partial u}{\partial m} = -\gamma \frac{(T_e - T_i)}{\rho} + \frac{\partial}{\partial m}\left(\rho \kappa_e \frac{\partial T_e}{\partial m}\right) + \frac{S(z,t)}{\rho} \tag{109}$$

Here ρ represents the substrate density, u its velocity and m its mass coordinate, while $P_{i/e}$ and $e_{i/e}$ are the pressure and specific energy of the ion lattice and the electrons respectively. These equations, stemming from [129–131] describe the thermal waves spreading in a substrate moving with velocity u. In our case, since we have very low displacement velocities (see table 3), we can assume u to be 0 and directly use equations 55 and 56, which can be derived from the equations above.

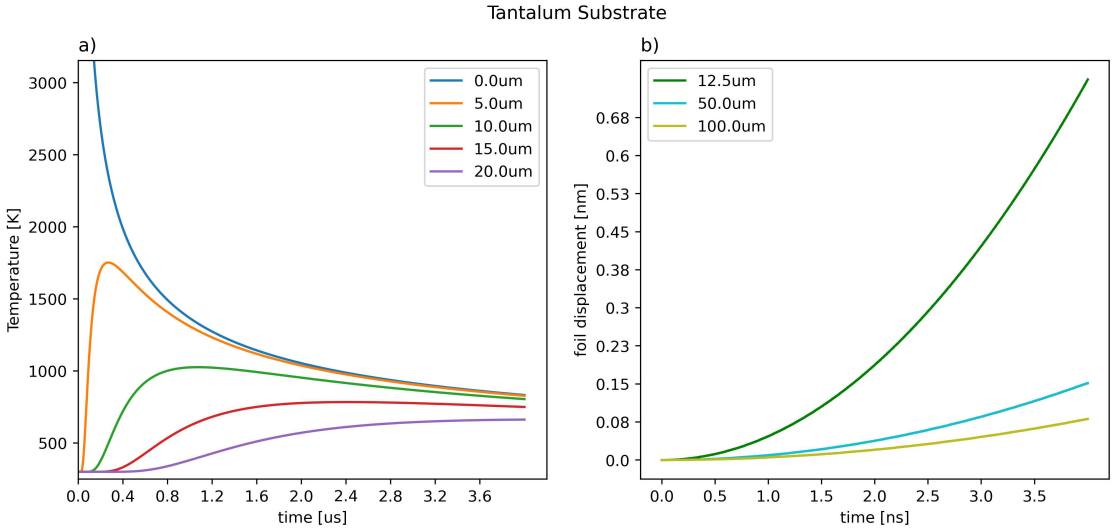

Figure 37: Laser ablation of Tantalum using a pulsed laser with $\lambda = 532\,\text{nm}$, with $\tau = 4\,\text{ns}$ and a pulse power of $3\,\text{mJ}$. **a)** Spread of the thermal wave at different positions in the sample. **b)** Substrate displacement during the irradiation with the pulsed laser as calculated from equation 81.

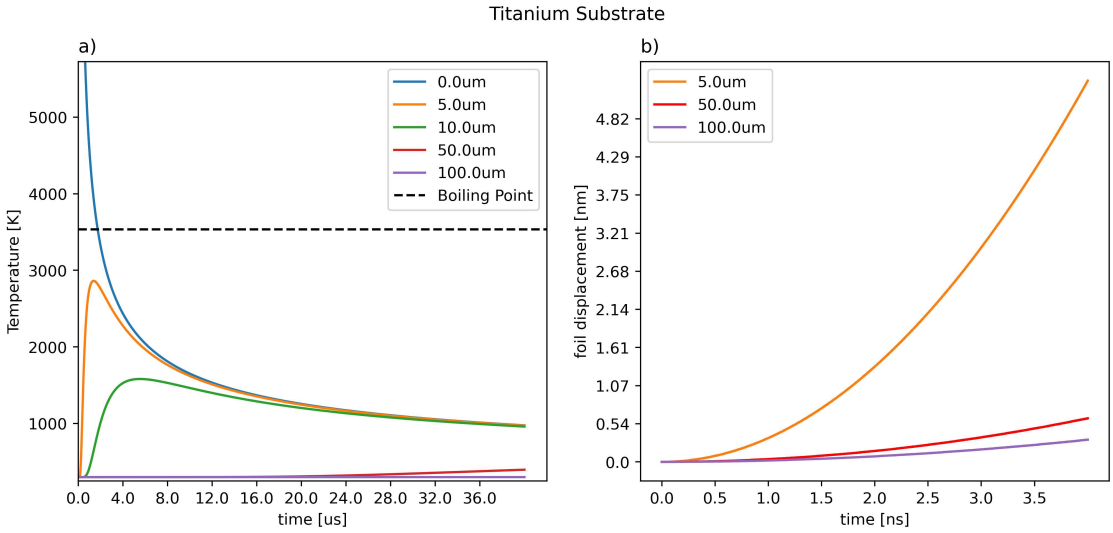

Figure 38: Laser ablation of Titanium using a pulsed laser with $\lambda = 532\,\text{nm}$, with $\tau = 4\,\text{ns}$ and a pulse power of $3\,\text{mJ}$. **a)** Spread of the thermal wave at different positions in the sample. **b)** Substrate displacement during the irradiation with the pulsed laser as calculated from equation 81.

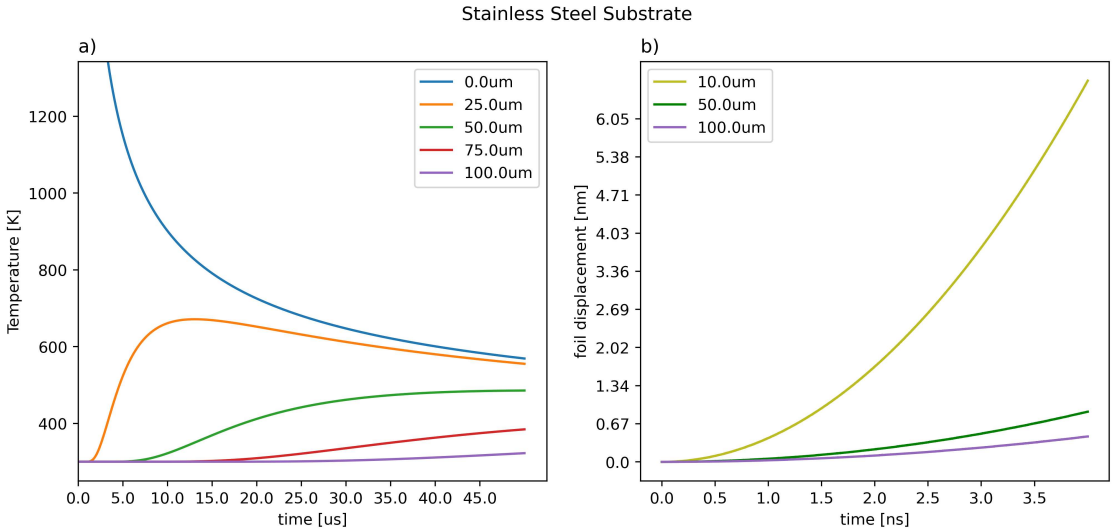

Figure 39: Laser ablation of Stainless Steel using a pulsed laser with $\lambda = 532\,\text{nm}$, with $\tau = 4\,\text{ns}$ and a pulse power of $3\,\text{mJ}$. **a)** Spread of the thermal wave at different positions in the sample. **b)** Substrate displacement during the irradiation with the pulsed laser as calculated from equation 81.

Python code used to estimate thermal waves and foil displacements.

```
import numpy as np
import matplotlib.pyplot as plt
import scipy.constants as cst
import scipy.special as sp

def ierfct(x):
    return 1/np.sqrt(np.pi) * (np.exp(-x**2) - x*(1-sp.erf(x)))
# Define the integrated error function for the thermal waves

# Definition of Meltout Laser Variables
tau = 4e-9
# Pulse length
```

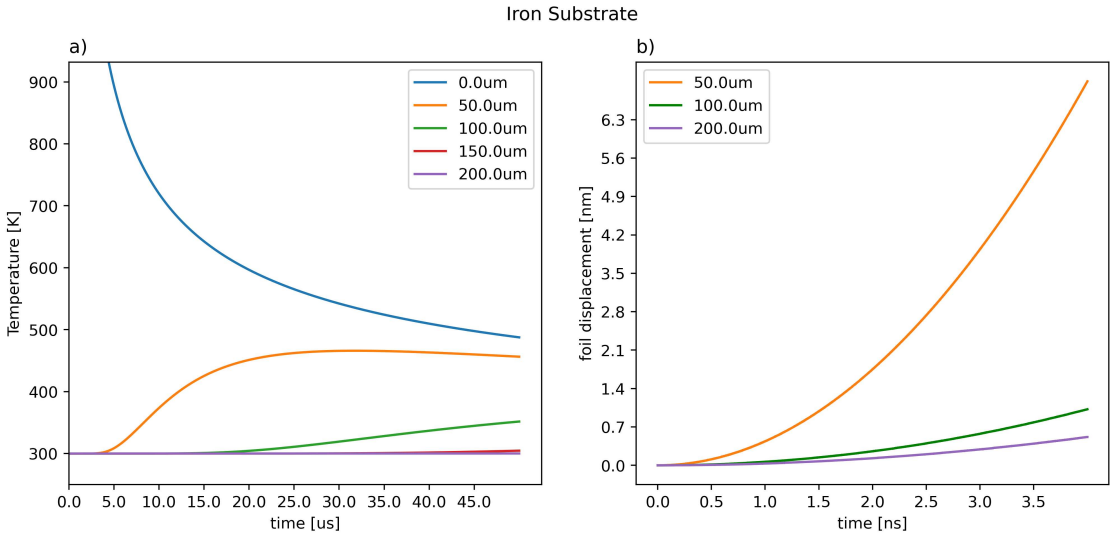

Figure 40: Laser ablation of Iron using a pulsed laser with $\lambda = 532\,\text{nm}$, with $\tau = 4\,\text{ns}$ and a pulse power of $3\,\text{mJ}$. **a)** Spread of the thermal wave at different positions in the sample. **b)** Substrate displacement during the irradiation with the pulsed laser as calculated from equation 81.

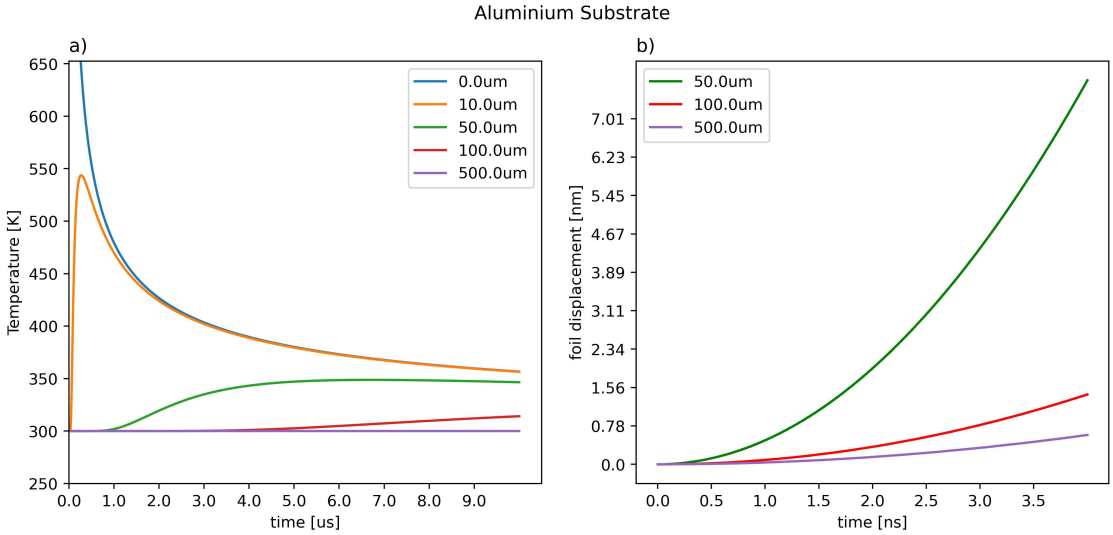

Figure 41: Laser ablation of Aluminium using a pulsed laser with $\lambda = 532\,\text{nm}$, with $\tau = 4\,\text{ns}$ and a pulse power of $3\,\text{mJ}$. **a)** Spread of the thermal wave at different positions in the sample. **b)** Substrate displacement during the irradiation with the pulsed laser as calculated from equation 81.

```
w_0 = 6e-5
# Waist
lambda_melt = 5.32e-7
# meltour laser Wavelength
z_R = cst.pi*w_0**2/lambda_melt
# Raileigh length
pp = 3e-3
# Polse power
P_0 = pp/tau
# Power of the laser pulse
k = 2*np.pi/lambda_melt
# Wavenumber
I_0 = 2*P_0/np.pi/w_0**2 * 0.37
```

```
# Peak Intensity W/m

T_0 = 300 # Enviromental temperature in Kelvin

P_abl = 7.26*1e8*(I_0*1e-13)**(3/4)*
(lambda_melt*1e6*tau*1e9)**(-1/4)
# Estimate of the ablation pressure
F_abl = P_abl*w_0**2*np.pi
# Estimate of the ablation recoil force

I_att = I_0*(I_0/I_opt)**-0.3
 # Attenuation of the Laser due to plume ionisation

# Plate dimensions lateral
Len = 5e-3

# Material constants
Metals = ["Copper", "Tantalum", "Titanium", "Stainless Steel",
          "Iron", "Aluminium"]
rho = np.array([8940, 16650, 4630, 7800, 7870, 2700])
# Material density
n_r = np.array([1.04, 1.09, 0.27, 2.75, 2.65, 0.77])
# Real index of refraction
n_i = np.array([2.59, 5.24, 4.61, 3.8, 3.34, 6.08])
# Imaginary index of refraction
A = np.array([0.244, 0.22, 0.401, 0.433, 0.382, 0.077])
# Absorptivity
E = np.array([129.8, 185,7, 105, 200, 211.4, 71])
# Young's Modulus
v = np.array([0.343, 0.342, 0.34, 0.27, 0.293, 0.33])
# Poisson ratio
kappa = np.array([391, 57, 11.4, 45, 73, 237])
 # thermal conductivity
eta = np.array([16.5, 6.6, 8.6, 10.4, 11.8, 22.6])
# thermal expansion coefficient
Tb = np.array([2835, 5632, 3533, 2900, 3134, 2743])
# Boiling temperature
cv = np.array([385, 140, 520, 460, 450, 900])
# Specific heat
alpha = np.zeros(len(Metals))
D = kappa / rho / cv


n = 0
# define the loop variable for the material choice

# Sample z positions, where we calculate the temperature
h0 = np.array([7e-4, 2e-5, 5e-5, 1e-4, 2e-4, 5e-4])
z = np.zeros((len(Metals), 5))
for d in range(5):
    z[:,d] = h0/4*d
```

```
z[0, :] = [0, 2.5e-5, 5e-5, 5e-4, 7e-4]
# Special choices for z chosen in case of Copper
z[2, :] = [0, 5e-6, 1e-5, 5e-5, 1e-4]
# Special choices for z chosen in case of Titanium
z[len(Metals)-1, :] = [0, 1e-5, 5e-5, 1e-4, 5e-4]
# Special choices for z chosen in case of Aluminium

# Thickness of the sample for the ablation pressure estimate
h = np.array([[5e-5, 5e-4, 7e-4], [1.25e-5, 5e-5, 1e-4],
              [5e-6, 5e-5, 1e-4], [1e-5, 5e-5, 1e-4],
              [5e-5, 1e-4, 2e-4], [5e-5, 1e-4, 5e-4]])

timestep = 5e4
 # define the number of timesteps
tges = np.array([1.5e-5, 4e-6, 4e-5, 5e-5, 5e-5, 1e-5])
# define the material dependent simulation time
t0 = 1.2e-9
# define the starting time of the simulation



smallt = np.linspace(0, tau, np.intc(timestep))
 # Define the time period for pressure simulation
theta = np.zeros([h[1,:].size, np.intc(timestep)])
# define the during pulse displacement vector for the simulations
T = np.zeros([len(Metals), z[n,:].size, np.intc(timestep)])
# define the temperature matrix for the simulations


while n < 6:
    # We calculate the spread of the thermal wave
    alpha[n] = 4* np.pi * n_i[n] / lambda_melt
    # Define the material absorption coefficient
    t = np.linspace(t0, tges[n], np.intc(timestep))
    # define the time vector for the simulations
    fig, ax = plt.subplots(1, 2, figsize=(12, 5), dpi =400.0)
    # Define the function and the axes of our Plot
    fig.suptitle(Metals[n] + " Substrate")
    for i in range(z[n,:].size):
        for j in range(np.intc(timestep)):
            T[n, i, j] = T_0 + 2 * A[n] * I_att *
            np.sqrt(D[n])/kappa[n] * (np.sqrt(t[j]) *
             ierfct(z[n, i] / 2 / np.sqrt(D[n] * t[j]))
             - np.sqrt((t[j] - tau))
             * ierfct(z[n, i] / 2 /
                      np.sqrt(D[n] * (t[j] - tau))) )
        ax[0].plot(t, T[n, i, :], label =
                   str(np.round(z[n, i], 6)*1e6) + "um")
    ax[0].set_title("a)", loc = "left")
    ax[0].set_xlim(0)
    ax[0].set_ylim(250, 1.2*np.nanmax(T[n, 1, :]))
    ax[0].set_xlabel("time [us]")
```

```
ax[0].set_ylabel("Temperature [K]")
xticks = np.arange(0, tges[n], tges[n]/10)
xlabels = [str(np.round(q, 2)) for q in xticks*1e6]
ax[0].set_xticks(xticks)
ax[0].set_xticklabels(xlabels)
ax[0].axhline(Tb[n], color = "k",
              linestyle = "--", label = "Boiling Point")
ax[0].legend()
print("Maximal temperature" + str(Metals[n]) +
      ":" + str(np.nanmax(T[n, 0, :])))

# We calculate the center foil displacement
for f in range(h[n,:].size):
    for l in range(1, 10, 2):
        for m in range(1, 10, 2):
            w_nm = np.sqrt(D[n]/2/rho[n]/h[n, f])*np.pi**2 *
            (m**2/Len + l**2/Len)
            theta[f,:] +=  F_abl/w_nm**2 *
            (1 - np.cos(w_nm*smallt)) *
            m*l/2/rho[n]/h[n, f]*(-1)**(m+l)*
            np.sin(m*np.pi/2)*np.sin(l*np.pi/2)
            theta[np.isnan(theta)] = 0
    print("Maximal foil displacement " +
          str(Metals[n]) + " h = "
          + str(h[n, f]) +":" +
          str(np.nanmax(theta[f,:])))
for i in range(h[n,:].size):
    ax[1].plot(smallt, theta[i,:], label =
               str(h[n, i]*1e6) + "um")
ax[1].legend()
ax[1].set_title("b)", loc = "left")
ax[1].set_xlabel("time [ns]")
xticks = np.arange(0, tau, 5e-10)
xlabels = [str(np.round(q, 2))
           for q in xticks*1e9]
ax[1].set_xticks(xticks)
ax[1].set_xticklabels(xlabels)
ax[1].set_ylabel("foil displacement [nm]")
yticks = np.arange(0, np.nanmax(theta),
                   np.nanmax(theta)/10)
ylabels = [str(np.round(q, 2))
           for q in yticks*1e9]
ax[1].set_yticks(yticks)
ax[1].set_yticklabels(ylabels)
n = n + 1
```

9 Appendix C: PPA melt out properties

This section contains the python code used to estimate the melting of PPA when irradiated with a laser, as well as the particle trajectory in the melt out beam. The PPA-melting has been simulated both in the way given in section 3.2.3, as well as how we treated laser ablation of metals in section 3.1.4, though the latter didn't given any realistic results.

```
import numpy as np
import matplotlib.pyplot as plt
import scipy.constants as cst
import scipy.special as sp

# Define the integrated error function for the thermal waves
def ierfct(x):
    return 1/np.sqrt(np.pi) * (np.exp(-x**2) - x*(1-sp.erf(x)))

# Properties of Meltout Laser
w_0 = 1e-6
# Waist in m
lambda_melt = 4.05e-7
# meltout laser Wavelength in m
z_R = cst.pi*w_0**2/lambda_melt
# Raileigh length in m
P_0 = 0.1
# total Power of the laser in W
k = 2*np.pi/lambda_melt
# Wavenumber in 1/m
I_0 = 2*P_0/np.pi/w_0**2
# Peak Intensity in W/m



# Properties of the substrate
rho = 1190
# Material density in kg/m^3
n_r = 1.63
# Real index of refraction
n_i = 4.8e-4
# Imaginary index of refraction
A = 0.2
# Absorptivity
kappa = 0.25
# thermal conductivity W/m/K
Tc = 150
# critical temperature in C
cm = 1554.62
# Specific heat in J/kg/K
alpha = 4* np.pi * n_i / lambda_melt
# material absorption coefficient
D = kappa / rho / cm
# heat diffusion coefficient in m^2/s
M = 0.134134
# molar mass of PPA in kg/mol
```

```
d = 1e-5
# Sample thickness in m
rhomol = rho/M*cst.Avogadro
# molar density of PPA in 1/m^3

# Properties of the nanoparticle
d_p = 2.5e-7
r_p = d_p/2
# Nanoparticle radius
Material = ["SiO2", "Au"]
# Nanoparticle material
rho_p = np.array([2650, 19300])
# density in kg/m^3
eps_p = np.array([2.1, -1.67 + 1j*5.73])
# dielectric constant at 405 nm
cm_p = np.array([650, 126])
# heat capacity in J/kg/K
m_at = np.array([60, 197])
# atomic mass in Da
T_m = np.array([1980,1340])
 # melting point
k_th = np.array([1.4, 318])
# thermal conductivity in W/m/K

m_p = 4*np.pi/3*r_p**3*rho_p
# particle mass
m_p_Da = m_p/(m_at*cst.u)
# number of atoms in the particle
alpha_r = 4*np.pi*cst.epsilon_0*r_p**3 *
          np.real( (eps_p-1)/(eps_p+2) )
# real part of complex polarizability
alpha_i = 4*np.pi*cst.epsilon_0*r_p**3 *
          np.imag( (eps_p-1)/(eps_p+2) )
# imaginary part of complex polarizability



# Properties of the background gas
T_0 = 300
# Enviromental temperature in K
p_g = 5
# Background pressure in pa
m_g = 28*cst.u
# Mass of the background gas in kg (N2)
r_N2 = 0.155e-9
# van der Waals radius of the nitrogen molecule in m
n = p_g/cst.Boltzmann/T_0
# nitrogen number density m^-3
rho_N2 = n* m_g
# nitrogen mass density kg/m^-3
v_mp = np.sqrt(8*cst.Boltzmann*T_0/np.pi/m_g)
# mean velocity of the background gas m/s
```

```
p_N2 = m_g*v_mp
# mean momentum of the background gas kg m/s
sigma_coll= np.pi*(2*r_N2)**2
# collisional cross section of Nitrogen m^2
L_mfp = 1/n/sigma_coll
# mean free path for N2 at p_g in m
eta_N2 = 1/3*n*m_g*v_mp*L_mfp
# kinematic viscosity of the ideal gas
Kn = L_mfp/r_p
# Knudsen number
c_K = 0.31*Kn/(0.785 + 1.152*Kn + Kn**2)
Gamma_0 = 6*np.pi*eta_N2*r_p/m_p*0.619/(0.619+Kn)*(1+c_K)
# Damping constant of the bakcground gas
T_mfp = L_mfp/v_mp
# Mean free path of the nanoparticle m


r = w_0
# radius for the esimation of PPA melting velocity
P_w_0 = P_0 * (1 - np.exp(-2*r**2/w_0**2))
# total laser power over area with radius r

# Simulation of the PPA temperature using the equations from metal
timestep = 5e4
# define the number of timesteps
tges = 1
# define the material dependent simulation time
t0 = 1.2e-9
# define the starting time of the simulation
t_m = np.linspace(t0, tges, np.intc(timestep))
# define the time vector for the simulations
z =  np.array([0, d])
T = np.zeros([z.size, np.intc(timestep)])

for i in range(z.size):
    for j in range(np.intc(timestep)):
        T[i, j] = T_0 + 2 * A * I_0 * np.sqrt(D*np.sqrt(t_m[j]))
                  / kappa * (ierfct(z[i] / 2 / np.sqrt(D * t_m[j])))
    plt.plot(t_m, T[i, :], label = str(np.round(z[i], 6)*1e6) + "um")



# Estimate the heating rate of PPA
vol = np.pi*w_0**2*1e-5
# Volume of the irradiated PPA substrate
N_sub = rhomol*vol
# Molecule number of the irradiated PPA substrate

P_abs = P_w_0/alpha *(1 - np.exp(-alpha*d))
# Power absorbed by the irradiated PPA substrate
P_ind = P_abs/N_sub
# Power absorbed per molecule
```

```
gamma_test = P_ind/(M/cst.Avogadro)/cm
# PPA heating rate
tau = Tc/gamma_test
# Time until PPA reaches critical temperature


# Simulation of the particle behaviour after meltout

# Cross sections of the nanoparticle
sigma_sc = k**4*alpha_r**2/6/np.pi/cst.epsilon_0**2;
# Scattering cross section in m^2
sig_abs = k/cst.epsilon_0*alpha_i;
# Absorption cross section in m^2

# Define the simulation time
T_p = 2
# Duration of the Simulation in seconds
t0_p = 0
# Initial time before simulation
stepnumber = 1e6
# Number of time steps
t_step = T_p/stepnumber
# Duration of one step
t = np.linspace(t0_p, T_p, np.intc(stepnumber))
if t_step > T_mfp:
    raise TypeError("Step size is bigger than mean free path of
                    the particle")

# Initialize the particle positions, velocities and accelerations
pos = np.zeros([2,np.intc(stepnumber)])
vel = np.zeros([2,np.intc(stepnumber)])
acc = np.zeros([2,np.intc(stepnumber)])

pos[0,0] = 0
# Initial particle x position at time t= 0
pos[1,0] = 0
# Initial particle z position at time t= 0
vel[0,0] = 0
 # Initial particle x velocity at time t= 0
vel[1,0] = 0
# Initial particle z velocity at time t= 0
acc[0,0] = 0
# Initial particle x acceleration at time t= 0
acc[1,0] = 0
# Initial particle z acceleration at time t= 0

# Variable to define the material
# if m=1, we have Au-NP, for m=0, they are made from SiO2
m = 1
# Loop variable for brownian motion
b = 0
```

```
# Define the intensity
I = np.zeros(np.intc(stepnumber))

for p in range(np.intc(stepnumber)-1):
    # Redefine the current positions, velocities and accelerations
    x = pos[0,p]
    z = pos[1,p]
    vx = vel[0,p]
    vz = vel[1,p]
    ax = acc[0,p]
    az = acc[1,p]

    # Calculate the current laser intensity at z
    wz = w_0*np.sqrt(1+(z/z_R)**2)
    I[p] = I_0*w_0**2/wz**2*np.exp(-2*x**2/wz**2)

    # Calculate the forces acting on the particle in this time step
    F_sc = I[p]*sigma_sc[m]/cst.c
    F_abs = I[p]*sig_abs[m]/cst.c
    F_rdip = -2*I_0*alpha_r[m]/cst.epsilon_0/cst.c*w_0**2*x/wz**4
             *np.exp(-2*x**2/wz**2)
    F_ldip = 4*I_0*alpha_r[m]*z/cst.epsilon_0/cst.c/wz**4/k**2*
             np.exp(-2*x**2/wz**2)*(2*x**2/wz**2-1)
    F_g = -m_p[m]*cst.g

    # Update accelerations of the particle
    acc[0,p+1] = (F_rdip)/m_p[m] - vel[0, p]*Gamma_0[m]
    acc[1,p+1] = (F_sc + F_abs + F_ldip + F_g)/m_p[m] -
                 vel[1,p]*Gamma_0[m]

    # Update the velocities and positions of the particle
    if (t[p]-t[b]) > T_mfp:
        ex = 1-2*np.random.rand()
        ez = 1-2*np.random.rand()
        # Define random variables for brwonian motion
        vel[0,p+1] = vel[0,p] + acc[0,p+1]*t_step + 2*ex*p_N2/m_p[m]
        vel[1,p+1] = vel[1,p] + acc[1,p+1]*t_step + 2*ez*p_N2/m_p[m]
        # Implement brownian motion
        b = p
    else:
        vel[0,p+1] = vel[0,p] + acc[0,p+1]*t_step
        vel[1,p+1] = vel[1,p] + acc[1,p+1]*t_step
        # No brownian motion
    pos[0,p+1] = pos[0,p] + vel[0,p]*t_step + acc[0,p+1]*t_step**2/2
    pos[1,p+1] = pos[1,p] + vel[1,p]*t_step + acc[1,p+1]*t_step**2/2

fig, ax = plt.subplots(1, 2, figsize=(10, 5), dpi =600.0)
ax[0].plot(t, pos[1,:], label = "heigth")
ax[0].set_xlabel("Time [s]")
ax[0].set_ylabel("Particle z position [m]")
```

```
ax[0].set_title("a)", loc = "left")
ax[0].axhline(pos[1,-1], color = "k", linestyle = "--", label =
              "Equilibrium position: " +
              str(np.round(pos[1,-1]*1e3, 2))+ " mm")
ax[0].legend()

ax[1].plot(pos[0,:], pos[1,:], "r", label = "Position")
ax[1].set_xlabel("Particle x position [m]")
ax[1].set_ylabel("Particle z position [m]")
ax[1].set_title("b)", loc = "left")
ax[1].legend()
fig.suptitle(str(d_p*1e9) + " nm " + str(Material[m]) +
             " Nanoparticle")

# Calculate the heating rate of the nanoparticles
P_abs = I_0*sig_abs[m]
# Absorbed power in W
gamma_heat = P_abs/m_p[m]/cm_p[m]
# Heating rate in K/s
t_melt = T_m[m]/gamma_heat
# melting time in s
```

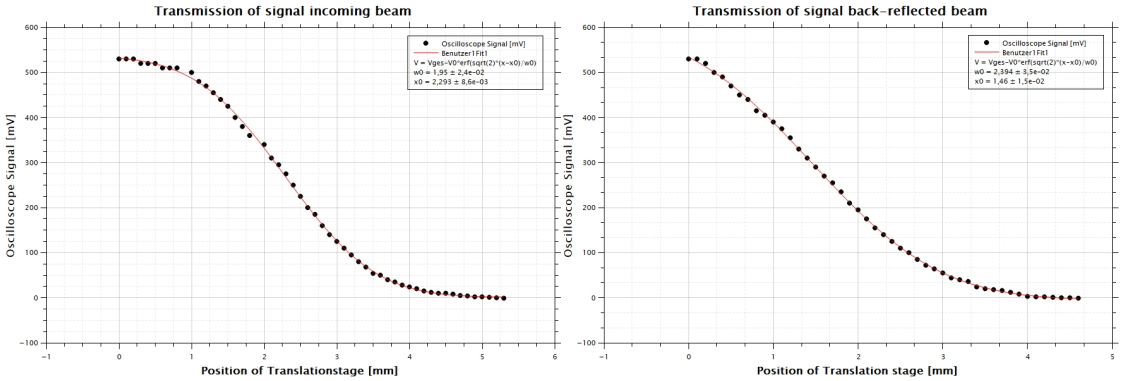

Figure 42: Intensity profiles for the $1550\,\mathrm{nm}$ detection beam both for the incoming beam, as well as for the back-reflection coming from the vacuum chamber. The measurement of the incoming beam has been taken between the $\lambda/2$-plate and mirror M_{T1}, while the measurement of the back-reflex has been taken between the polarising beam splitter and the photodiode measuring the back-reflex.

10 Appendix D: Detection beam diameter

We measure the detection beam diameter before focussing using a razor blade and a translation stage. The results can be observed in figure 42. The razor blade was pushed into the beam using the translation stage, while continuously measuring the power of the laser behind the razor blade using a Coherent Field mate PM10 power meter. The intensity of a Gaussian beam is given in equation 27. If we operate at the waist and integrate over one of the lateral components, we get:

$$\int \sqrt{\frac{\pi}{2}} w_0 I(x,z)\mathrm{dx} = \sqrt{\frac{\pi}{2}} w_0 \int I_0 \exp -\frac{2x^2}{w_0^2}\mathrm{dx} = I_0 \frac{w_0^2 \pi}{4} \mathrm{erf}\left(\frac{\sqrt{2}x}{w_0}\right) + C \tag{110}$$

Here the factor $w_0\sqrt{\pi/2}$ comes from the integration over the y-component:

$$\int_{-\infty}^{\infty} \exp\left(-\frac{2x^2}{w_0^2}\right)\mathrm{dy} = \sqrt{\frac{\pi}{2}} w_0 \tag{111}$$

Equation 110 gives us the transmitted intensity when blocking off a section of the beam spanning from $-\infty$ to x in the x-direction and $-\infty$ to ∞ in the y-direction. If we fit our measurements to equation 110, we can use it to determine the beam diameter, as seen in figure 42. We arrive at a beam diameter of $(3.900 \pm 0.048)\,\mathrm{mm}$ for the incoming beam and $(4.788 \pm 0.070)\,\mathrm{mm}$ for the back-reflected beam. The beam diameter in both cases is larger than the given beam diameter of $3.6\,\mathrm{mm}$ of our collimator, which we attribute to beam divergence.

References

[1]V. B. Braginsky, "Classical and quantum restrictions on the detection of weak disturbances of a macroscopic oscillator", Zh. Eksp. Teor. Fiz **53**, 1434–1441 (1967).

[2]D. H. Douglass, R. Q. Gram, J. A. Tyson, and R. W. Lee, "Two-detector-coincidence search for bursts of gravitational radiation", Physical Review Letters **35**, Publisher: American Physical Society, 480–483 (1975).

[3]A. Ashkin, "Acceleration and trapping of particles by radiation pressure", Physical Review Letters **24**, 156–159 (1970).

[4]A. Ashkin and J. M. Dziedzic, "Optical trapping and manipulation of viruses and bacteria", Science **235**, ISBN: 0036-8075 Publisher: American Association for the Advancement of Science, 1517–1520 (1987).

[5]A. Ashkin, J. M. Dziedzic, and T. Yamane, "Optical trapping and manipulation of single cells using infrared laser beams", Nature **330**, 769–771 (1987).

[6]D. J. Wineland, R. E. Drullinger, and F. L. Walls, "Radiation-pressure cooling of bound resonant absorbers", Physical Review Letters **40**, Publisher: American Physical Society, 1639–1642 (1978).

[7]T. Li, S. Kheifets, and M. G. Raizen, "Millikelvin cooling of an optically trapped microsphere in vacuum", Nature Physics **7**, 527–530 (2011).

[8]J. Gieseler, B. Deutsch, R. Quidant, and L. Novotny, "Sub-kelvin parametric feedback cooling of a laser-trapped nanoparticle", Physical Review Letters **109**, 103603 (2012).

[9]T. W. Penny, A. Pontin, and P. F. Barker, "Sympathetic cooling and squeezing of two co-levitated nanoparticles", Physical Review Research **5**, 013070 (2023).

[10]N. Kiesel, F. Blaser, U. Delić, D. Grass, R. Kaltenbaek, and M. Aspelmeyer, "Cavity cooling of an optically levitated submicron particle", Proceedings of the National Academy of Sciences **110**, 14180–14185 (2013).

[11]P. Asenbaum, S. Kuhn, S. Nimmrichter, U. Sezer, and M. Arndt, "Cavity cooling of free silicon nanoparticles in high-vacuum", Nature Communications **4**, 2743 (2013).

[12]U. Delić, M. Reisenbauer, D. Grass, N. Kiesel, V. Vuletić, and M. Aspelmeyer, "Cavity cooling of a levitated nanosphere by coherent scattering", Physical Review Letters **122**, 123602 (2019).

[13]U. Delić, M. Reisenbauer, K. Dare, D. Grass, V. Vuletić, N. Kiesel, and M. Aspelmeyer, "Cooling of a levitated nanoparticle to the motional quantum ground state", Science **367**, 892–895 (2020).

[14]J. Piotrowski, D. Windey, J. Vijayan, C. Gonzalez-Ballestero, A. d. I. R. Sommer, N. Meyer, R. Quidant, O. Romero-Isart, R. Reimann, and L. Novotny, "Simultaneous ground-state cooling of two mechanical modes of a levitated nanoparticle", Nature Physics **19**, 1009–1013 (2023).

[15]J. Ahn, Z. Xu, J. Bang, P. Ju, X. Gao, and T. Li, "Ultrasensitive torque detection with an optically levitated nanorotor", Nature Nanotechnology **15**, 89–93 (2020).

[16]S. Nimmrichter, K. Hornberger, and K. Hammerer, "Optomechanical sensing of spontaneous wave-function collapse", Physical Review Letters **113**, 020405 (2014).

[17]B. A. Stickler, B. Papendell, S. Kuhn, B. Schrinski, J. Millen, M. Arndt, and K. Hornberger, "Probing macroscopic quantum superpositions with nanorotors", New Journal of Physics **20**, 122001 (2018).

[18]G. Pesce, P. H. Jones, O. M. Maragò, and G. Volpe, "Optical tweezers: theory and practice", The European Physical Journal Plus **135**, 949 (2020).

[19]S. Kuhn, "Cooling and manipulating the ro-translational motion of dielectric particles in high vacuum", Dr. rer. nat. (University Vienna, Vienna, 2017), 123 pp.

[20]F. Kiałka, Y. Y. Fein, S. Pedalino, S. Gerlich, and M. Arndt, "A roadmap for universal high-mass matter-wave interferometry", AVS Quantum Science **4**, 020502 (2022).

[21]K. Benham, R. Hodyss, F. M. Fernández, and T. M. Orlando, "Laser-induced acoustic desorption atmospheric pressure photoionization via VUV-generating microplasmas", Journal of the American Society for Mass Spectrometry **27**, 1805–1812 (2016).

[22]E. Weisman, C. K. Galla, C. Montoya, E. Alejandro, J. Lim, M. Beck, G. P. Winstone, A. Grinin, W. Eom, and A. A. Geraci, "An apparatus for in-vacuum loading of nanoparticles into an optical trap", Review of Scientific Instruments **93**, 115115 (2022).

[23]L. Hanley, O. Kornienko, E. T. Ada, E. Fuoco, and J. L. Trevor, "Surface mass spectrometry of molecular species", Journal of Mass Spectrometry **34**, 705–723 (1999).

[24]H. Franz, J. Thorsten W., and K. Michael, *MALDI MS: a practical guide to instrumentation, methods, and applications*, 2nd ed. (Wiley-VCH Verlag GmbH & Co. KGaA, 2014), 1-40.

[25]L. Konermann, E. Ahadi, A. D. Rodriguez, and S. Vahidi, "Unraveling the mechanism of electrospray ionization", Analytical Chemistry **85**, 2–9 (2013).

[26]J. Therrien, A. Dindar, and D. Smith, "AFM studies of nanoparticle deposition via electrospray ionization", Microscopy Research and Technique **70**, 530–533 (2007).

[27]S.-C. Tseng, C.-C. Yu, D.-C. Lin, Y.-C. Tseng, H.-L. Chen, Y.-C. Chen, S.-Y. Chou, and L. A. Wang, "Laser-induced jets of nanoparticles: exploiting air drag forces to select the particle size of nanoparticle arrays", Nanoscale **5**, 2421 (2013).

[28]U. Zywietz, A. B. Evlyukhin, C. Reinhardt, and B. N. Chichkov, "Laser printing of silicon nanoparticles with resonant optical electric and magnetic responses", Nature Communications **5**, 3402 (2014).

[29]V. Golovlev, S. Allman, W. Garrett, N. Taranenko, and C. Chen, "Laser-induced acoustic desorption", International Journal of Mass Spectrometry and Ion Processes **169/171**, 69–78 (1997).

[30]D. S. David, *A guided tour of light beams*, 2nd ed. (IOP Publishing Ltd, Easton, 2020), 137 pp.

[31]W. Nagourney, *Quantum electronics for atomic physics and telecommunication*, 2nd ed. (OUP Oxford, Oxford, 2014), 1-11.

[32]E. Kriezis, D. Chrissoulidis, and A. Papagiannakis, *Electromagnetics and optics*, 1st (World Scientific, Signapore, 1992), 241-245.

[33]*Encyclopedia of optical engineering* (Taylor & Francis, Apr. 2011).

[34]A. Ashkin, S. Chu, J. E. Bjorkholm, and J. M. Dziedzic, "Observation of a single-beam gradient force optical trap for dielectric particles", Optical Society of America **11** (1986).

[35]P. H. Jones, O. M. Maragò, and G. Volpe, *Optical tweezers: principles and applications*, 1st ed. (Cambridge University Press, Dec. 3, 2015).

[36]P. A. M. Neto and H. M. Nussenzveig, "Theory of optical tweezers", Europhysics Letters (EPL) **50**, 702–708 (2000).

[37]T. A. Nieminen, V. L. Y. Loke, A. B. Stilgoe, G. Knöner, A. M. Brańczyk, N. R. Heckenberg, and H. Rubinsztein-Dunlop, "Optical tweezers computational toolbox", Journal of Optics A: Pure and Applied Optics **9**, S196–S203 (2007).

[38]D. McGloin, "Optical tweezers: 20 years on", Philosophical Transactions of the Royal Society A: Mathematical, Physical and Engineering Sciences **364**, 3521–3537 (2006).

[39]A. Callegari, M. Mijalkov, A. B. Gököz, and G. Volpe, "Computational toolbox for optical tweezers in geometrical optics", Journal of the Optical Society of America B **32**, B11 (2015).

[40]J. E. Molloy and M. J. Padgett, "Lights, action: optical tweezers", Contemporary Physics **43**, 241–258 (2002).

[41]I. C. D. Lenton, A. B. Stilgoe, H. Rubinsztein-Dunlop, and T. A. Nieminen, "Visual guide to optical tweezers", European Journal of Physics **38**, 034009 (2017).

[42]T. A. Nieminen, N. Du Preez-Wilkinson, A. B. Stilgoe, V. L. Loke, A. A. Bui, and H. Rubinsztein-Dunlop, "Optical tweezers: theory and modelling", Journal of Quantitative Spectroscopy and Radiative Transfer **146**, 59–80 (2014).

[43]F. Gittes and C. F. Schmidt, "Interference model for back-focal-plane displacement detection in optical tweezers", Optics Letters **23**, 7 (1998).

[44]F. Tebbenjohanns, M. Frimmer, and L. Novotny, "Optimal position detection of a dipolar scatterer in a focused field", Physical Review A **100**, 043821 (2019).

[45]L. Dania, K. Heidegger, D. S. Bykov, G. Cerchiari, G. Araneda, and T. E. Northup, "Position measurement of a levitated nanoparticle via interference with its mirror image", Physical Review Letters **129**, 013601 (2022).

[46]G. Cerchiari, L. Dania, D. S. Bykov, R. Blatt, and T. E. Northup, "Position measurement of a dipolar scatterer via self-homodyne detection", Physical Review A **104**, 053523 (2021).

[47]S. Zhu, L. Ma, S. Wang, C. Chen, W. Zhang, L. Yang, W. Hang, J. P. Nolan, L. Wu, and X. Yan, "Light-scattering detection below the level of single fluorescent molecules for high-resolution characterization of functional nanoparticles", ACS Nano **8**, 10998–11006 (2014).

[48]S. Kuhn, P. Asenbaum, A. Kosloff, M. Sclafani, B. A. Stickler, S. Nimmrichter, K. Hornberger, O. Cheshnovsky, F. Patolsky, and M. Arndt, "Cavity-assisted manipulation of freely rotating silicon nanorods in high vacuum", Nano Letters **15**, 5604–5608 (2015).

[49]A. C. Pflanzer, O. Romero-Isart, and J. I. Cirac, "Master equation approach to optomechanics with arbitrary dielectrics", Physical Review A **86**, 013802 (2012).

[50]C. F. Bohren and D. R. Huffman, *Absorption and scattering of light by small particles*, 1st ed. (Wiley, Apr. 23, 1998).

[51]P. Asenbaum, "Cavity cooling of silicon nanoparticles in high-vacuum", Doktor der Naturwissenschaften (Universität Wien, Wien, 2014), 97 pp.

[52]R. Schiffer and K. O. Thielheim, "Light scattering by dielectric needles and disks", Journal of Applied Physics **50**, 2476–2483 (1979).

[53]M. Renz, "Fluorescence microscopy—a historical and technical perspective", Cytometry Part A **83**, 767–779 (2013).

[54]J. W. Lichtman and J.-A. Conchello, "Fluorescence microscopy", Nature Methods **2**, 910–919 (2005).

[55]H. Mader, X. Li, S. Saleh, M. Link, P. Kele, and O. S. Wolfbeis, "*Fluorescent Silica Nanoparticles*", Annals of the New York Academy of Sciences **1130**, 218–223 (2008).

[56]S. F. Wuister, I. Swart, F. Van Driel, S. G. Hickey, and C. De Mello Donegá, "Highly luminescent water-soluble CdTe quantum dots", Nano Letters **3**, 503–507 (2003).

[57]L. Jacak, H. Pawel, and W. Arkadiusz, *Quantum dots* (Springer Science & Business Media, 2013).

[58]A. J. Nozik, "SPECTROSCOPY AND HOT ELECTRON RELAXATION DYNAMICS IN SEMICONDUCTOR QUANTUM WELLS AND QUANTUM DOTS", Annual Review of Physical Chemistry **52**, 193–231 (2001).

[59]A. P. Demchenko, "Photobleaching of organic fluorophores: quantitative characterization, mechanisms, protection", Methods and Applications in Fluorescence **8**, 022001 (2020).

[60]M. Nikkhou, Y. Hu, J. A. Sabin, and J. Millen, "Direct and clean loading of nanoparticles into optical traps at millibar pressures", Photonics **8**, 458 (2021).

[61]H.-C. Lin, J.-L. Lin, and C.-H. Chen, "Novel mass spectrometry technology development for large organic particle analysis", RSC Adv. **4**, 4523–4534 (2014).

[62]L. Nyadong, J. P. Quinn, C. S. Hsu, C. L. Hendrickson, R. P. Rodgers, and A. G. Marshall, "Atmospheric pressure laser-induced acoustic desorption chemical ionization mass spectrometry for analysis of saturated hydrocarbons", Analytical Chemistry **84**, 7131–7137 (2012).

[63]T. Sugai, "Mass and charge measurements on heavy ions", Mass Spectrometry **6**, S0074–S0074 (2017).

[64]O. Kostko, L. K. Takahashi, and M. Ahmed, "Desorption dynamics, internal energies, and imaging of organic molecules from surfaces with laser desorption and vacuum ultraviolet (VUV) photoionization", Chemistry – An Asian Journal **6**, 3066–3076 (2011).

[65]W. C. Natzle, D. Padowitz, and S. J. Sibener, "Ultraviolet laser photodesorption of NO from condensed films: translational and internal energy distributions", The Journal of Chemical Physics **88**, 7975–7994 (1988).

[66]L. Hanley, R. Wickramasinghe, and Y. P. Yung, "Laser desorption combined with laser postionization for mass spectrometry", Annual Review of Analytical Chemistry **12**, 225–245 (2019).

[67]D. S. Peterson, "Mass spectrometry reviews - 2006 - peterson - matrix-free methods for laser desorption ionization mass spectrometry.pdf", Mass Spectrometry Reviews **26**, 16 (2006).

[68]M. Karas and F. Hillenkamp, "Laser desorption ionization of proteins with molecular masses exceeding 10,000 daltons", Analytical Chemistry **60**, 2299–2301 (1988).

[69]E. De Hoffmann, V. Stroobant, and E. De Hoffmann, *Mass spectrometry: principles and applications*, 3. ed., reprinted (Wiley, Chichester Weinheim, 2011), 489 pp.

[70]K. Dreisewerd, "The desorption process in MALDI", Chemical Reviews **103**, 395–426 (2003).

[71]M. W. Duncan, H. Roder, and S. W. Hunsucker, "Quantitative matrix-assisted laser desorption/ionization mass spectrometry", Briefings in Functional Genomics and Proteomics **7**, 355–370 (2008).

[72]I.-C. Lu, C. Lee, Y.-T. Lee, and C.-K. Ni, "Ionization mechanism of matrix-assisted laser desorption/ionization", Annual Review of Analytical Chemistry **8**, 21–39 (2015).

[73]X. Ma, Y. Zhang, H.-R. Lei, and H. I. Kenttämaa, "Laser-induced acoustic desorption", MRS Bulletin **44**, 372–381 (2019).

[74]Z. Huang, T. Ossenbrüggen, I. Rubinsky, M. Schust, D. A. Horke, and J. Küpper, "Development and characterization of a laser-induced acoustic desorption source", Analytical Chemistry **90**, 3920–3927 (2018).

[75]A. V. Zinovev, I. V. Veryovkin, J. F. Moore, and M. J. Pellin, "Laser-driven acoustic desorption of organic molecules from back-irradiated solid foils", Analytical Chemistry **79**, 8232–8241 (2007).

[76]U. Sezer, L. Wörner, J. Horak, L. Felix, J. Tüxen, C. Götz, A. Vaziri, M. Mayor, and M. Arndt, "Laser-induced acoustic desorption of natural and functionalized biochromophores", Analytical Chemistry **87**, 5614–5619 (2015).

[77]R. C. Shea, C. J. Petzold, J. L. Campbell, S. Li, D. J. Aaserud, and H. I. Kenttämaa, "Characterization of laser-induced acoustic desorption coupled with a fourier transform ion cyclotron resonance mass spectrometer", Analytical Chemistry **78**, 6133–6139 (2006).

[78]P. Wen-Ping, L. Huan-Chang, L. Hsin-Hung, C. Minglee, L. Y. Alice, C. HuanCheng, and C. Chung-Hsuan, "Charge-monitoring laser-induced acoustic desorption mass spectrometry for cell and microparticle mass distribution measurement", Angewandte Chemie **119**, 3939–3943 (2007).

[79]J. Pérez, L. E. Ramırez-Arizmendi, C. J. Petzold, L. P. Guler, E. D. Nelson, and H. I. Kenttämaa, "Laser-induced acoustic desorption/chemical ionization in fourier-transform ion cyclotron resonance mass spectrometry", International Journal of Mass Spectrometry **198**, 173–188 (2000).

[80]L. Jia, J. Weng, Z. Zhou, F. Qi, W. Guo, L. Zhao, and J. Chen, "Note: laser-induced acoustic desorption/synchrotron vacuum ultraviolet photoionization mass spectrometry for analysis of fragile compounds and heavy oils", Review of Scientific Instruments **83**, 026105 (2012).

[81]S.-C. Cheng, M.-Z. Huang, and J. Shiea, "Thin-layer chromatography/laser-induced acoustic desorption/electrospray ionization mass spectrometry", Analytical Chemistry **81**, 9274–9281 (2009).

[82]L. B. Freund and S. Suresh, *Thin film materials: stress, defect formation and surface evolution* (Cambridge university press, 2004).

[83]A. Zinovev, I. Veryovkin, and M. Pelli, "Molecular desorption by laser–driven acoustic waves: analytical applications and physical mechanisms", in *Acoustic waves - from microdevices to helioseismology* (InTech, Nov. 14, 2011).

[84]D. Tasche, T. Weihs, and W. Viöl, "FUNDAMENTALS OF LASER ABLATION", Laser ablation : fundamentals, methods and applications (2015).

[85]C. Wu and L. V. Zhigilei, "Microscopic mechanisms of laser spallation and ablation of metal targets from large-scale molecular dynamics simulations", Applied Physics A **114**, 11–32 (2014).

[86]B. N. Chicbkov, C. Momma, and S. Nolte, "Femtosecond, picosecond and nanosecond laser ablation of solids", **63**, 109–115 (1996).

[87]A. M. Prokhorov, ed., *Laser heating of metals*, The Adam Hilger series on optics and optoelectronics (A. Hilger, Bristol ; Philadelphia, 1990), 239 pp.

[88]J. H. Bechtel, "Heating of solid targets with laser pulses", Journal of Applied Physics **46**, 1585–1593 (1975).

[89]D. J. Förster, B. Jäggi, A. Michalowski, and B. Neuenschwander, "Review on experimental and theoretical investigations of ultra-short pulsed laser ablation of metals with burst pulses", Materials **14**, 3331 (2021).

[90]C. R. Phipps, T. P. Turner, R. F. Harrison, G. W. York, W. Z. Osborne, G. K. Anderson, X. F. Corlis, L. C. Haynes, H. S. Steele, and K. C. Spicochi, "IMPULSE COUPLING TO TARGETS IN VACUUM BY KrF, HF AND CO2 SINGLE-PULSE LASERS", Journal of Applied Physics **64**, 1083–1096 (1988).

[91]R. K. Singh and J. Narayan, "Pulsed-laser evaporation technique for deposition of thin films: physics and theoretical model", Physical review B **41**, 8843 (1990).

[92]D. Lee and S. Jeong, "Analysis of recoil force during nd:YAG laser ablation of silicon", Applied Physics A **79**, 1341–1344 (2004).

[93]D. W. Gregg and S. J. Thomas, "Momentum transfer produced by focused laser giant pulses", Journal of Applied Physics **37**, 2787–2789 (1966).

[94]P. Mora, "Theoretical model of absorption of laser light by a plasma", The Physics of Fluids **25**, 1051–1056 (1982).

[95]T. W. Murray and J. W. Wagner, "Laser generation of acoustic waves in the ablative regime", Journal of Applied Physics **85**, 2031–2040 (1999).

[96]J. P. Gospodyn, A. Sardarli, A. M. Brodnikovski, and R. Fedosejevs, "Ablative generation of surface acoustic waves in aluminum using ultraviolet laser pulses", Journal of Applied Physics **92**, 564–571 (2002).

[97]A. W. Leissa, *Vibration of plates.* 160 (Scientific, Technical Information Division,National Aeronautics, and Space Administration, 1969).

[98]N. McLachlan, *Theory of vibrations* (Dover Publications Inc, New York, 1951).

[99]S. Smith, *Flexures - elements of elastic mechanics* (Gordon and Breach Science Publishers, Amsterdam, 2000).

[100]B. A. Boley and J. H. Weiner, *Theory of thermal stresses* (Courier Corporation, 2012).

[101]K. Cholevas, N. Liosatos, A. Romanov, M. Zaiser, M. Zaiser, E. Aifantis, and E. Aifantis, "Misfit dislocation patterning in thin films", physica status solidi (b) **209**, 295–304 (1998).

[102]S. V. Bobylev and I. A. Ovid'ko, "Faceted grain boundaries in polycrystalline films", Physics of the Solid State **45**, 1926–1931 (2003).

[103]G. Janssen, "Stress and strain in polycrystalline thin films", Thin Solid Films **515**, 6654–6664 (2007).

[104]M. Bass and O. S. of America, eds., *Handbook of optics*, 2nd ed (McGraw-Hill, New York, 1995), 4 pp.

[105]S. Wang, G. L. Abma, P. Krüger, A. Van Roij, M. Balster, N. Janssen, and D. A. Horke, "Comparing pulsed and continuous laser-induced acoustic desorption (LIAD) as sources for intact biomolecules", The European Physical Journal D **76**, 128 (2022).

[106]J. Millens, "Cooling and manipulation of nanoparticles in high vacuum", Proceedings Volume 9922, Optical Trapping and Optical Micromanipulation XIII, `https://doi.org/10.1117/12.2238753` (2016).

[107]D. S. Bykov, P. Mestres, L. Dania, L. Schmöger, and T. E. Northup, "Direct loading of nanoparticles under high vacuum into a paul trap for levitodynamical experiments", Applied Physics Letters **115**, 034101 (2019).

[108]N. J. Demarais, Z. Yang, T. P. Snow, and V. M. Bierbaum, "GAS-PHASE REACTIONS OF POLYCYCLIC AROMATIC HYDROCARBON CATIONS AND THEIR NITROGEN-CONTAINING ANALOGS WITH h ATOMS", The Astrophysical Journal **784**, 25 (2014).

[109]W.-P. Peng, H.-C. Lin, M.-L. Chu, H.-C. Chang, H.-H. Lin, A. L. Yu, and C.-H. Chen, "Charge monitoring cell mass spectrometry", Analytical Chemistry **80**, 2524–2530 (2008).

[110]W.-P. Peng, Y.-C. Yang, M.-W. Kang, Y.-K. Tzeng, Z. Nie, H.-C. Chang, W. Chang, and C.-H. Chen, "Laser-induced acoustic desorption mass spectrometry of single bioparticles", Angewandte Chemie **45**, 1423–1426 (2006).

[111]J. A. Kaitz, C. E. Diesendruck, and J. S. Moore, "End group characterization of poly(phthalaldehyde): surprising discovery of a reversible, cationic macrocyclization mechanism", Journal of the American Chemical Society **135**, 12755–12761 (2013).

[112]F. Wang and C. E. Diesendruck, "Polyphthalaldehyde: synthesis, derivatives, and applications", Macromolecular Rapid Communications **39**, 1700519 (2018).

[113]J. M. Schwartz, O. Phillips, A. Engler, A. Sutlief, J. Lee, and P. A. Kohl, "Stable, high-molecular-weight poly(phthalaldehyde)", JOURNAL OF POLYMER SCIENCE **55**, 1166–1172 (2016).

[114]A. M. DiLauro, J. S. Robbins, and S. T. Phillips, "Reproducible and scalable synthesis of end-cap-functionalized depolymerizable poly(phthalaldehydes)", Macromolecules **46**, 2963–2968 (2013).

[115]E. C. Feinberg, H. L. Hernandez, C. L. Plantz, E. B. Mejia, N. R. Sottos, S. R. White, and J. S. Moore, "Cyclic poly(phthalaldehyde): thermoforming a bulk transient material", ACS Macro Letters **7**, 47–52 (2018).

[116]K. M. Lee, O. Phillips, A. Engler, P. A. Kohl, and B. P. Rand, "Phototriggered depolymerization of flexible poly(phthalaldehyde) substrates by integrated organic light-emitting diodes", ACS Applied Materials & Interfaces **10**, 28062–28068 (2018).

[117]C. Huang, X. Qian, and R. Yang, "Thermal conductivity of polymers and polymer nanocomposites", Materials Science and Engineering: R: Reports **132**, 1–22 (2018).

[118]X. Xie, D. Li, T.-H. Tsai, J. Liu, P. V. Braun, and D. G. Cahill, "Thermal conductivity, heat capacity, and elastic constants of water-soluble polymers and polymer blends", Macromolecules **49**, 972–978 (2016).

[119]C. Wu, J. Jiang, H. Guo, X. Pu, L. Liu, W. Ding, P. A. Kohl, and Z. L. Wang, "Sunlight-triggerable transient energy harvester and sensors based on triboelectric nanogenerator using acid-sensitive poly(phthalaldehyde)", Advanced Electronic Materials **5**, 1900725 (2019).

[120]X. Liu, S. T. Howell, A. Conde-Rubio, G. Boero, and J. Brugger, "Thermomechanical nanocutting of 2d materials", Advanced Materials **32**, 2001232 (2020).

[121]O. Coulembier, A. Knoll, D. Pires, B. Gotsmann, U. Duerig, J. Frommer, R. D. Miller, P. Dubois, and J. L. Hedrick, "Probe-based nanolithography: self-amplified depolymerization media for dry lithography", Macromolecules **43**, 572–574 (2010).

[122]J. N. Israelachvili, *Intermolecular and surface forces*, 3rd ed. (Elsevier Inc., Santa Barbara, 2011).

[123]N. Bityurin, B. S. Luk'yanchuk, M. H. Hong, and T. C. Chong, "Models for laser ablation of polymers", Chemical Reviews **103**, 519–552 (2003).

[124]T. Lippert, "Laser application of polymers", in *Polymers and light*, Vol. 168, edited by T. K. Lippert, Series Title: Advances in Polymer Science (Springer Berlin Heidelberg, Berlin, Heidelberg, 2004), pp. 51–246.

[125]O. Phillips, A. Engler, J. M. Schwartz, J. Jiang, C. Tobin, Y. A. Guta, and P. A. Kohl, "Sunlight photodepolymerization of transient polymers", Journal of Applied Polymer Science **136**, 47141 (2019).

[126]J. Gieseler, R. Quidant, and L. Novotny, "Dynamics of optically levitated nanoparticles in high vacuum", PhD thesis (ICFO, Feb. 3, 2014).

[127]X. Fang, K. F. MacDonald, E. Plum, and N. I. Zheludev, "Coherent control of light-matter interactions in polarization standing waves", Scientific Reports **6**, 31141 (2016).

[128]J. R. Horak, "Design and characterisation of a LIAD source in view of matter wave interferometry", (2013).

[129]M. E. Povarnitsyn, N. E. Andreev, E. M. Apfelbaum, T. E. Itina, K. V. Khishchenko, O. F. Kostenko, P. R. Levashov, and M. E. Veysman, "A wide-range model for simulation of pump-probe experiments with metals", Applied Surface Science **258**, 9480–9483 (2012).

[130]M. E. Povarnitsyn, V. B. Fokin, and P. R. Levashov, "Microscopic and macroscopic modeling of femtosecond laser ablation of metals", Applied Surface Science **357**, 1150–1156 (2015).

[131]S. I. Anisimov, N. A. Inogamov, Y. V. Petrov, V. A. Khokhlov, V. V. Zhakhovskii, K. Nishihara, M. B. Agranat, S. I. Ashitkov, and P. S. Komarov, "Interaction of short laser pulses with metals at moderate intensities", Applied Physics A **92**, 939–943 (2008).